QC
1
.U56
Vol. 64C
No. 2

Volume 64C
Number 2
Apr.–June 1960

UNIVERSITY OF MICHIGAN
JUN 8 1960
LIBRARY

Journal of Research

of the

NATIONAL BUREAU OF STANDARDS

C. ENGINEERING AND INSTRUMENTATION

Journal of Research
of the
National Bureau of Standards

C. Engineering and Instrumentation

APR.-JUNE • 1960

VOLUME • 64C

NUMBER • 2

Editor: W. A. Wildhack

Associate Editors: G. F. Montgomery, R. B. Jacobs

Publication dates:
Feb. 15, Apr. 15, Aug. 15, Nov. 15, 1960

JOURNAL OF RESEARCH

The National Bureau of Standards Journal of Research reports research and development in the fields of activity shown at right. Also included from time to time are survey articles of information on topics closely related to the Bureau's scientific and technical program.

The Journal is published in four separate sections as follows:

A. Physics and Chemistry

Contains papers of interest primarily to scientists working in these fields. Issued six times a year. Annual subscription: domestic, $4.00; foreign, $4.75.

B. Mathematics and Mathematical Physics

Presents studies and compilations designed mainly for the mathematician and the theoretical physicist. Issued quarterly. Annual subscription: domestic, $2.25; foreign, $2.75.

C. Engineering and Instrumentation

Reports research and development results of interest chiefly to the engineer and the applied scientist. Issued quarterly. Annual subscription: domestic, $2.25; foreign, $2.75.

D. Radio Propagation

Reports work in radio propagation physics and upper atmospheric research. Issued six times a year. Annual subscription: domestic, $4.00; foreign, $4.75.

U.S. DEPARTMENT OF COMMERCE
Frederick H. Mueller, Secretary

NATIONAL BUREAU OF STANDARDS
A. V. Astin, Director

Functions and Activities

The functions of the National Bureau of Standards are set forth in the Act of Congress, March 3, 1901, as amended. These include the development and maintenance of the national standards of measurement and the provision of means and methods for making measurements consistent with these standards; the determination of physical constants and properties of materials; the development of methods and instruments for testing materials, devices, and structures; advisory services to government agencies on scientific and technical problems; invention and development of devices to serve special needs of the Government; and the development of standard practices, codes, and specifications. The work includes basic and applied research, development, engineering, instrumentation, testing, evaluation, calibration services, and various consultation and information services. The Bureau also serves as the Federal technical research center in a number of specialized fields. The scope of activities of the National Bureau of Standards is suggested in the following listing of the divisions and sections engaged in technical work.

Washington, D.C

Electricity and Electronics. Resistance and Reactance. Electron Devices. Electrical Instruments. Magnetic Measurements. Dielectrics. Engineering Electronics. Electronic Instrumentation. Electrochemistry.

Optics and Metrology. Photometry and Colorimetry. Optical Instruments. Photographic Technology. Length. Engineering Metrology.

Heat. Temperature Physics. Thermodynamics. Cryogenic Physics. Rheology. Engine Fuels. Free Radicals Research.

Atomic Physics. Spectroscopy. Radiometry. Mass Spectrometry. Solid State Physics. Electron Physics. Atomic Physics.

Radiation Physics. Neutron Physics. Radiation Theory. Radioactivity. X-ray. High Energy Radiation. Nucleonic Instrumentation. Radiological Equipment.

Chemistry. Organic Coatings. Surface Chemistry. Organic Chemistry. Analytical Chemistry. Inorganic Chemistry. Electrodeposition. Molecular Structure and Properties of Gases. Physical Chemistry. Thermochemistry. Spectrochemistry. Pure Substances.

Mechanics. Sound. Mechanical Instruments. Fluid Mechanics. Engineering Mechanics. Mass and Scale. Capacity, Density, and Fluid Meters. Combustion Controls.

Organic and Fibrous Materials. Rubber. Textiles. Paper. Leather. Testing and Specifications. Polymer Structure. Plastics. Dental Research.

Metallurgy. Thermal Metallurgy. Chemical Metallurgy. Mechanical Metallurgy. Corrosion. Metal Physics.

Mineral Products. Engineering Ceramics. Glass. Refractories. Enameled Metals. Concreting Materials. Constitution and Microstructure.

Building Technology. Structural Engineering. Fire Protection. Air Conditioning, Heating, and Refrigeration. Floor, Roof, and Wall Coverings. Codes and Safety Standards. Heat Transfer.

Applied Mathematics. Numerical Analysis. Computation. Statistical Engineering. Mathematical Physics.

Data Processing Systems. SEAC Engineering Group. Components and Techniques. Digital Circuitry. Digital Systems. Analog Systems. Applications Engineering.

• Office of Basic Instrumentation. • Office of Weights and Measures

Boulder, Colorado

Cryogenic Engineering. Cryogenic Equipment. Cryogenic Processes. Properties of Materials. Gas Liquefaction.

Radio Propagation Physics. Upper Atmosphere Research. Ionosphere Research. Regular Prediction Services. Sun-Earth Relationships. VHF Research. Radio Warning Services. Airglow and Aurora. Radio Astronomy and Arctic Propagation.

Radio Propagation Engineering. Data Reduction Instrumentation. Radio Noise. Tropospheric Measurements. Tropospheric Analysis. Propagation-Terrain Effects. Radio-Meteorology. Lower Atmosphere Physics.

Radio Standards. High-Frequency Electrical Standards. Radio Broadcast Service. Radio and Microwave Materials. Atomic Frequency and Time Standards. Electronic Calibration Center. Microwave Circuit Standards.

Radio Communication and Systems. Low Frequency and Very Low Frequency Research. High Frequency and Very High Frequency Research. Modulation Systems. Antenna Research. Navigation Systems. Systems Analysis. Field Operations.

Order all publications from the Superintendent of Documents
U.S. Government Printing Office, Washington 25, D.C.

Use of funds for printing this publication approved by the Director of the Bureau of the Budget (June 24, 1958).

DEPOSITED BY THE
UNITED STATES OF AMERICA

JOURNAL OF RESEARCH of the National Bureau of Standards—C. Engineering and Instrumentation
Vol. 64C, No. 2, April–June 1960

Measurement of Cobalt-60 and Cesium-137 Gamma Rays with a Free-Air Chamber

H. O. Wyckoff

(October 27, 1959)

Design data for free-air chambers measuring cobalt-60 and cesium-137 gamma rays in roentgens are presented. It has been shown that the Jaffé-Zanstra method of obtaining the saturation current is adequate for air pressures of about 4 to 12 atmospheres. Also, radiation measurements of the gamma rays from cobalt-60 and cesium-137 made by a cavity chamber and a free-air chamber agree to within the experimental errors.

1. Introduction

The standard instrument for measurement of 5 to 500 kv X-rays in roentgens is the free-air chamber [1].[1] Both free-air chambers [2, 3, 4] and cavity chambers are used for measurement in roentgens of the gamma rays from radium, cobalt-60, and cesium-137. Kaye and Binks [2] used both methods to measure the same source of radium and obtained agreement to the order of 1 percent between the two results. However, Taylor and Singer [3] have since pointed out that the free-air chamber measurements by Kaye and Binks were too low by the order of 2 percent because of inadequate plate separation. Ionization from scattered photons, for which no correction was made, may have compensated for part of this error. This contribution was not measured either by Kaye and Binks or by Taylor and Singer. On the other hand Attix and Ritz [5] have indicated that the cavity-chamber measurements of Kaye and Binks require a 1½ percent correction for chamber wall attenuation. An additional possible source of error, inadequate guarding of the collector region, has been pointed out [6] for free-air chamber measurement of low-energy X-rays. Preliminary estimates of this effect on the radium [3], cobalt-60 [4], and cesium-137 [4] measurements indicate that the dose rates given there may be up to 5 percent low. Thus, there is not yet an unambiguous comparison of the two methods.

At the present time, neither type of instrument is designated [1] as the standard instrument in the million-volt region. The ultimate selection of one, largely hinges on their individual capability of absolute accuracy. Therefore, measurement of the exposure dose rate of the same radiation sources by the two methods and an analysis of the factors affecting the accuracy seems desirable. Cobalt-60 and cesium-137 gamma-ray sources have already been measured in this laboratory by cavity-chamber methods and an analysis of the accuracy has been performed [5]. Similar treatment is needed for the free-air chamber method and this paper describes such an analysis.

One of the factors which may limit the accuracy of the free-air chamber measurements is the determination of the saturation current. In order to limit the dimensions of the free-air chamber, the ionized air is often at high pressure. Under this condition it is impossible to collect all of the ionization; one must rely on a theoretical extrapolation to an infinite value of the collecting field.

One method of performing this extrapolation, the Jaffé-Zanstra theory [7], has been checked and verified experimentally by Taylor et al. [8] for air pressures of up to 10 atm.[2] According to this theory [7], a plot of the inverse of the collected ionization current versus a particular function of x, $f(x)$, should give a straight line and the intercept at $f(x)=0$, where the field strength is infinite, should give the inverse of the saturation current. Here $x=c(V/DP)^2$; where V=collecting potential in volts; D=plate seperation in cm; P=pressure in atmospheres; and c is empirically determined from the requirement that the inverse of the collected ionization versus $f(x)$ should be a straight line. Curves of $f(x)$ versus x are available in the literature [7]. However, at least two very different values of c have been published [8, 9]. The latter reference also recommends a field strength per atmosphere of at least 80 v cm^{-1} atm^{-1}, contrary to the earlier work [8] where fields of less than 10 v cm^{-1} atm^{-1} give data that fall on the straight line plot.

A second method of extrapolation to an infinite field has been suggested by Kara-Michaelova and Lea [10]. They plot the inverse of the measured ionization current versus the inverse of the collecting potential. For sufficiently high potential, a linear relation exists which may be extrapolated to an

[1] Figures in brackets indicate the literature references at the end of this paper.

[2] The authors neglected the correction for the scattered photon contribution. When such a correction is made for cesium-137 gamma rays, the extrapolated current per atmosphere at 10 atm is at least 2 percent less than that at 1 atm. The correction should be larger for the 300-kv X-rays used for this test by Taylor et al.

infinite collection field. The authors also pointed out the equivalence of the two methods for obtaining saturation current when the collecting potentials are sufficiently high. Therefore, an exploration of the feasibility of the suggested extrapolation methods seems desirable for the present application. At the same time, it is worthwhile to obtain the radial distribution of the ionization from the primary electrons and from the scattered photons and the distance required for electron equilibrium. These are necessary [11] design data for the construction of a free-air chamber for measuring the gamma rays from cesium-137 and cobalt-60 in roentgens.

The main objective of this report is, therefore, to carefully measure a cobalt-60 and a cesium-137 gamma-ray source with a free-air chamber, and compare these measurements with those obtained with the cavity chamber. With a careful analysis of the accuracy of each type of measurement it may be possible to indicate which is capable of greatest accuracy at the present time and therefore, can be designated as the standard instrument in the million-volt region. However, the free-air chamber measurements require an exploration of the feasibility of the extrapolation methods for saturation and the determination of the design data necessary for the construction of free-air chambers for measuring cesium-137 and cobalt-60 gamma rays in roentgens.

2. Experimental Arrangement

A small beam of gamma rays from a radiation source is defined by an accurately known aperture (approximately 2 cm in diameter) in the shutter-diaphragm (fig. 1). This aperture is at the end of a cylindrical hole parallel to, but displaced from the axis of the cylindrical shutter-diaphragm. Rotation of the shutter cuts off the beam and permits measurement of the leakage radiation without introducing a modification of the scattering conditions. The beam passes first through a thin aluminum window (0.8 mm thick), then midway between and parallel to the two vertical plates of a parallel-plate ionization chamber, and then through a glass exit window. The ionization chamber is sealed inside a large tank filled with air under high pressure so that the mass of air between the plates is adequate for totally absorbing all the energy of the highest energy electrons produced by the beam of gamma rays.

One of the plates of the ionization chamber is maintained at a high potential with respect to ground (see sec. A–A of fig. 1); the other is divided into 3 collecting regions (plates marked 2, 4, 5a, 5b, 6a, 6b, 7a, 7b, and 9) and 4 large and 6 small grounded guard plates (see elevation view of fig. 1). The center collecting region is divided into 7 separate insulated plates (marked 4, 5a, 5b, 6a, 6b, 7a, and 7b). Each collector plate is separated from the adjacent plate by an air gap of 0.5 mm. A flat grounded plate is installed between the collector plates and the tank at about 3 cm from the collector plate to reduce the possibility of ionization collection from behind the collector plate.

The ionization to any of the collecting plates can be measured. During an exposure the plates which are not used for ionization measurement are grounded. After careful alinement of the plate

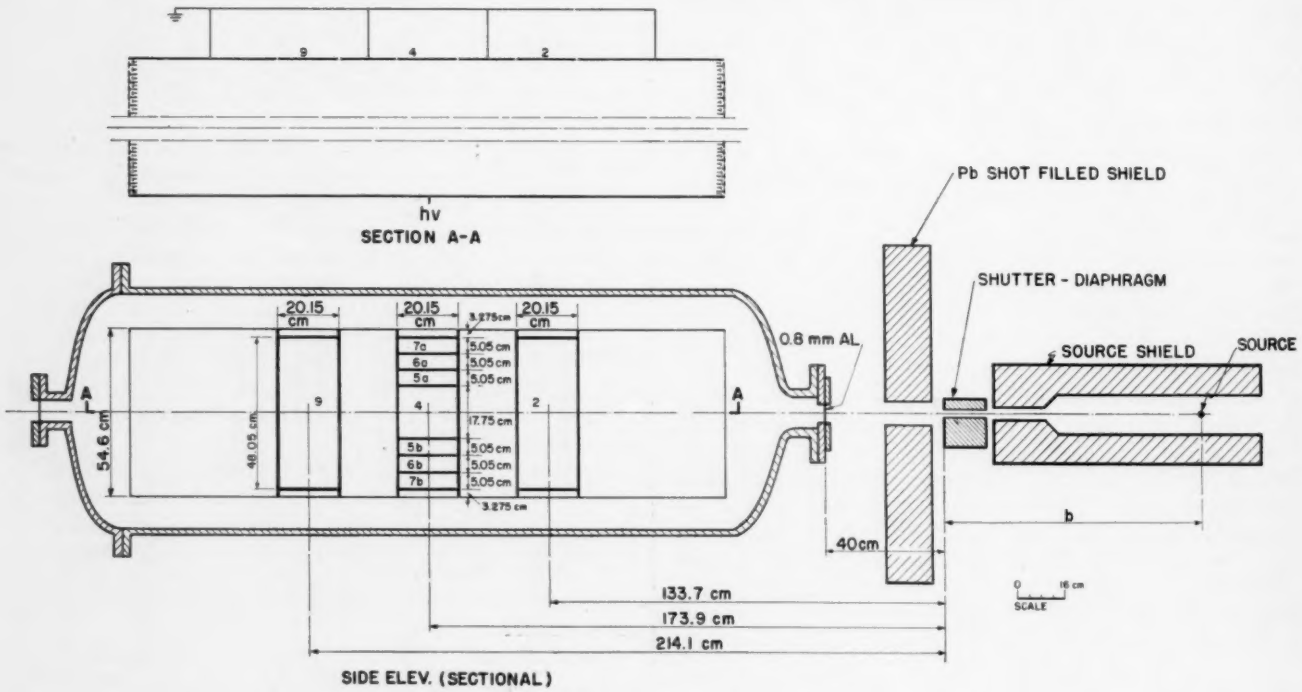

FIGURE 1. *The experimental arrangement.*

system, the displacement of the plane of each collector from the adjacent guard plate is measured. Generally, this is less than 0.03 mm but increases to as much as 0.1 mm very near the top of plate 2 and the bottom of plate 9 because of warpage of these plates. This causes a distortion of the field. However, previous measurements [11] indicate that as the ionization collected in this latter region is small, this distortion should cause no more than 0.1 percent error in the collected ionization.

This collector plate arrangement provides a means for determining the adequacy of the plate separation at a given pressure and also provides a means for determining the air absorption of the gamma-ray beam. With proper guarding of the electric field, each plate collects ionization from a volume defined by the plate height, the length of 20.15 cm (fig. 1), and the distance between the collector and high-voltage plates. Thus, by observing the relative amount of ionization collected by each of the plates 4 to 7, it is possible to determine if the effective plate separation (the product of plate separation and pressure) is adequate to collect all the ionization from electrons produced in the beam.

The ionization current collected by plate 9 is smaller than that collected by plate 2, due to air absorption. Therefore, the ratio of these two measurements may be used to compute the air absorption coefficient. Comparison of these computed values at the different pressures for each source provides an independent estimate of the precision of the current measurements. A comparison with the theoretical absorption coefficient indicates whether there is a difference in any systematic error between the current measurements to the two plates.

Guard bars are used to assure that the grounded tank does not distort the field in the collecting region. These are T cross section aluminum bars equally spaced between the chamber plates and parallel to these. In order to avoid extra photon attenuation and scattering, vertical bars are not used in either the front or back of the guard system where they might be struck by the beam (fig. 2). In these regions, fine aluminum wires are used instead of bars. A resistance network with a tap for each bar divides the potential uniformly between the high voltage and ground. A determination of the ability of these guard bars to eliminate the effect of the pressure tank on the electric field between a collector and the high-voltage plate requires an auxiliary experiment. As pointed out previously [5, 11], this is accomplished by noting the variation in collected ionization current as the potential of the tank is varied. Ionization measurements to each of the collectors indicate no variation greater than ± 0.1 percent as the tank potential varies from ground potential up to the potential of the high-voltage plate. Thus, the tank produces no distortion of the collecting field which changes the collecting volume by more than the precision of measurement (about ± 0.1 percent). All subsequent measurements are performed with the tank at ground potential.

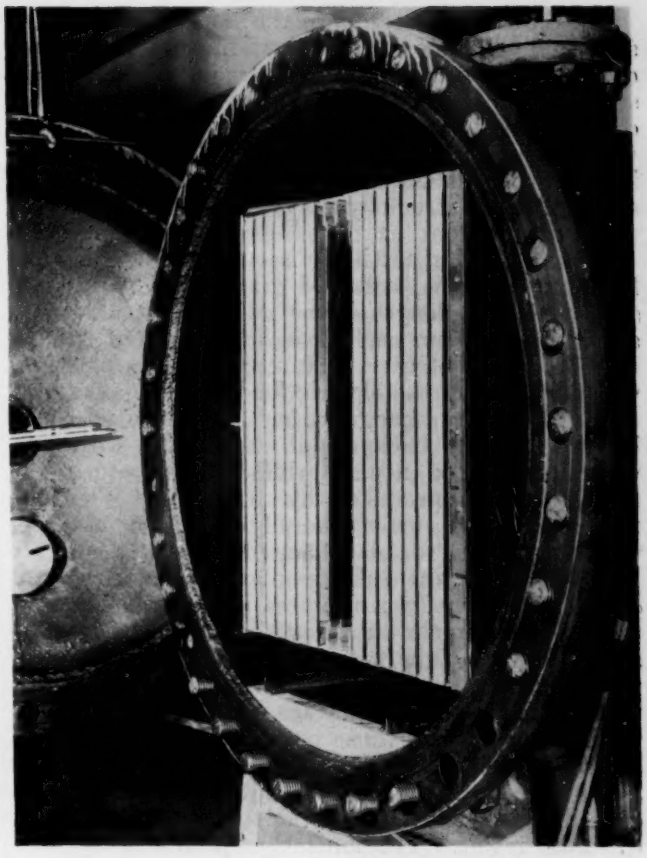

FIGURE 2. *A view of the back of the tank with the end bell removed showing the guard bars for the chamber.*

The air pressure in the tank is determined from the reading of a bourdon-type gage and the barometric pressure. The gage is calibrated by a piston gage and shows a short-time (over about 2 yr) maximum drift of calibration of about ± 0.2 psi and a long-time stability (over 8 yr) of about ± 0.3 psi except for a progressive zero shift (0.4 psi over 8 yr). For pressures of less than 5 atm, a mercury manometer also is used. In this range, the two methods agree with each other to within 0.2 percent. Filters and an ice-cooled condenser in the pumping system, as well as silica gel on the inside of the tank, maintain a low water vapor pressure. Mass spectrometric tests of the air under pressure indicate that the composition is the same as room air.

Separate thermocouples are used to test for possible temperature differences of the high-pressure air in the various ion collecting regions of the tank, and to calibrate as a function of pressure a mercury thermometer placed inside the tank near the exit window. For this test, thermocouples are placed at the center of each of the collecting regions as well as near the thermometer. After a short stabilizing period, all of the thermocouples give temperatures agreeing to better than 0.2° C. Moreover, the calibration of the thermometer at a given pressure appears to be constant to 0.2° C, although its calibration varies by nearly 1° C over the pressure range used.

In order to determine the ionization due to scattered photons, the ionization current also is obtained with a 10-cm diam 2-m long, Bakelite tube surrounding the collimated beam of photons inside of the tank. This tube is of sufficient thickness (about 3 mm) so that it stops all electrons originating in the air within the tube, and of sufficient diameter so that it is not struck by the primary beam of gamma rays.

To reduce the possible distortion of the electric field by the tube, colloidal graphite is painted in strips along the length of the tube. Adjacent strips are insulated from each other by uncoated tubing. Each of these strips is maintained at a potential which minimizes the electric field distortion by connecting it to the proper guard bars. Observation of the ionization from background radiation [3] with and without the tube in place gives an estimate of the field distortion produced by the tube. With the tube in place the current should be the same as those without the tube for plates 5a, 5b, 6a, 6b, 7a, and 7b. However, with the tube in place plate 4 will not collect ionization from the area in the tube shadow, that is, between the tube and the high voltage plate and within the tube but the difference can be computed from the geometry. The measured current to the different collectors are in the same ratio to within 5 percent as those predicted from the geometry. As the scattered photon contribution is only 2 or 3 percent of the total ionization, field distortion caused by the presence of the tube does not affect the final result. The ionization produced by electrons generated by the primary photons is, within the precision of measurement, proportional to the difference between the ionization measured with [4] and without this tube.

The ionization-current measuring system consists of a null indicating electrometer with feedback, a carefully calibrated condenser, and a variable bucking potential provided by a potentiometer. Timing of each exposure is accomplished by means of a scaler and a 1-kc oscillator [12]. This chronograph gives timing accuracies of about 0.01 percent for the times used here.

Measurements are made with the shutter closed in order to correct for the background. As the shutter-closed measurement is not changed when a solid lead plug is inserted into the hole in the lead-shot-filled shield, the leakage radiation through the shutter is negligible and the shutter-closed measurement indicates the background.

In addition to corrections for leakage radiation and air-scattered photons, it is also necessary to correct for any ionization from photons scattered by the source shield or diaphragm. Consider any rays which are scattered by the source shield and then pass through the diaphragm aperture. It may be shown for the geometry of figure 1 that the path of such rays will pass through the collector regions at distances greater than 5 cm from the axis of the primary beam. Thus, the ionization that they produce in the collecting region will be measured both with and without the Bakelite tubing in place, and the difference in readings will not include ionization either from photons scattered by the source shield or from the air in the chamber.

The effect of scattering from the diaphragm is explored by comparing the ionization current with diaphragms 15 cm and 22.5 cm long.

The source holders are made as light as is consistent with dimensional stability so as to reduce the amount of scattered radiation from them. These source holders fit into the large hole in the rear end of the source shield. The position of the source is determined by observing the position of the end of the long rod attached to each source holder. The radiation is measured perpendicular to the axis of the 3.2 mm diam by 3.2 mm long cobalt-60 source and along the axis of the 4.6 mm diam by 5 mm long cesium-137 source. The cobalt-60 source is encapsulated in aluminum with a 1.6 mm thick wall and the cesium-137 in 1 mm thick stainless steel.

A separate piece of equipment similar to that previously used [13] provides a means of determining the distance required for electronic equilibrium [11]. A grid chamber (fig. 3), made of colloidal-graphite-

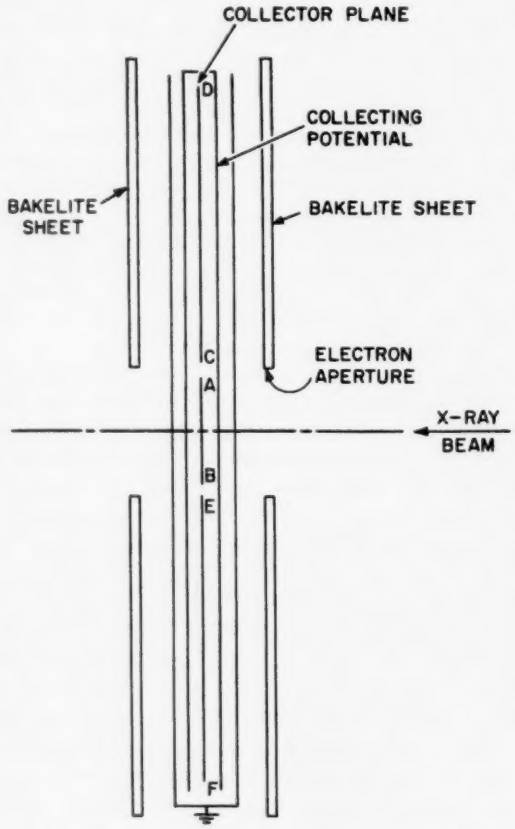

FIGURE 3. *Schematic plan view of the thread chamber and electron diaphragms.*

For simplicity the threads in each plane are drawn as a single line.

[3] The background radiation is assumed to produce a uniform density of ionization over the whole collecting region.

[4] A slight correction is required for the shadow cast by the tube and a larger correction for lack of saturation. The reduction of the scattered photon ionization by photon absorption in the tubewall is much smaller than 0.1 percent of the tube-out ionization. Therefore this reduction can be neglected.

coated nylon threads ($\sim$ 0.2 mm diam) in 5 parallel planes spaced about 1 cm apart, is placed in the pressure tank with the planes perpendicular to the gamma-ray beam. The threads in any one plane also are spaced about 1 cm apart. The threads in the central plane form a collector at near ground potential, and the two adjacent planes are connected to the collecting potential. The collector plane has two collecting regions separated by uncoated thread for insulation. A central collecting region, which is coaxial with the gamma-ray beam, is about 6.5 cm diam (AB in fig. 3). The outer collecting region has an inner diameter of 8.5 cm (CE) and an outer diameter of 51 cm (DF). The gamma-ray beam diameter at the position of the collector plane is about 6.5 cm. Thus, the central collector measures the ionization in a cylindrical region of about 2 cm depth and a diameter of 7.5 cm, and the outer collector measures the ionization in a ring of about 2 cm depth, 7.5 cm inner diameter and about 51 cm outer diameter.

A circular electrically-conducting Bakelite sheet (electron diaphragm), which is thicker than the range of the electrons produced by the gamma rays in air, is positioned perpendicular to the gamma-ray beam and in front of the grid chamber. A similar sheet is positioned behind the chamber. Each sheet has a center hole, which is slightly larger than the gamma-ray beam and coaxial with it, and each can be moved along the beam by remote control from outside the pressure tank.

3. Results and Discussion

The ionization current to each of the collector plates is measured both with and without the Bakelite tube and for a variety of pressures and collecting potentials. Data are obtained for five different pressures from 3.96 to 10.75 atm with the gamma rays from cesium-137 and for pressures of 10.75 and 12.27 atm for cobalt-60 gamma rays in order to choose a value for the Jaffé-Zanstra constant, c. With the Bakelite tube in place part of the ionization from the scattered photons is produced in the shadow of the tube and is thus not collected on plates 2, 4, and 9. However, the ionization produced in a ring about the axis of the beam decreases only slowly with increase of the ring radius [5]. Therefore, it is relatively simple [14] to make a correction for this shadowing, and also to change from the rectangular coordinate system of measurement for plates 4 to 7 to a cylindrical set of coordinates. For a given pressure and collecting potential, the difference between the ionization measured without the tube in place and the shadow-corrected determination with the tube in place is proportional to the ionization produced in the collecting length (20.15 cm) by the electrons generated by the primary gamma rays.

If the pressure is too low, so that some of the energy of the electrons is dissipated in the plates, a linear extrapolation to larger radii may be performed [14] on a log-current-loss versus radius plot. For the data reported here, this extrapolation does not exceed ⅔ percent.

Data from the large range of pressures used with cesium-137 gamma rays permits a study of the techniques for extrapolating to infinite collecting fields. Figure 4 shows plots of the inverse of the ionization currents,[6] I, against the Jaffé-Zanstra parameter, $f(x)$. Four values of c are used to obtain $f(x)$ in order to determine the value of c which gives a straight line. The value of 1.24×10^{-4} is that used by Taylor et al., [3] and by Grove [4]. It is seen that the point for the largest value of $f(x)$ falls well *below* the straight line through the remaining points. However, for both $c=3.2\times10^{-5}$ and $c=2.5\times10^{-5}$, all data fall on straight lines with slightly different intercepts at $f(x)=0$ (infinite collecting field). For $c=10^{-5}$, the points for large values of $f(x)$ fall *above* the straight line for the remaining points. The proper intercept on the $1/I$ axis therefore probably lies between that obtained for $c=10^{-5}$ and for $c=1.24\times10^{-4}$.

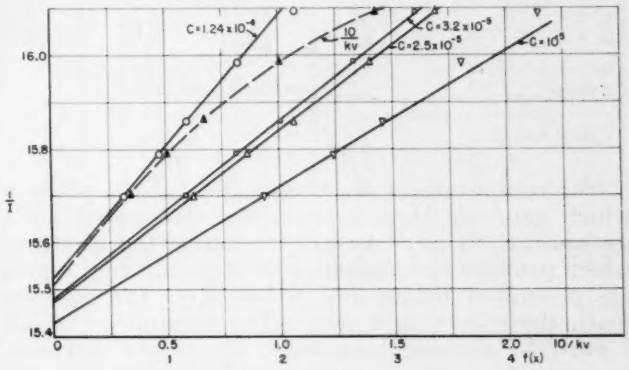

FIGURE 4. *Sample plots of the extrapolation procedure with cesium-137 gamma rays at a tank pressure of 3.96 atm.*

Four Jaffé-Zanstra type plots are indicated using different values of c. A Kara-Michaelova and Lea type plot (marked I0/kv) does not give a straight line relation.

Also included in figure 4 is a plot (marked 10/kv) of the inverse of the ionization current, I, against the inverse of the collecting potential (Kara-Michaelova and Lea). The intercept on the $1/I$ axis for the inverse collecting potential plot is indeterminate as the points do not fall on a straight line even for the three smallest values of $1/I$, where the effective electric field strengths are about 171, 114, and 85.5 v cm^{-1} atm^{-1}.

While the uncertainty in the intercept by these two methods is small at this pressure because the extrapolation is only about 1½ percent, the uncertainty becomes larger at the higher pressures where the extrapolation is as large as 10 percent. Fortunately, there is another criterion for choosing the proper extrapolation procedure.

[5] Scattering in the source shield or collimator might distort this monotonic decrease but such effects prove to be small in the present arrangement. Correction is still required for lack of saturation.

[6] Tube-in minus tube-out determination after correction for tube shadowing.

The exposure dose rate at the aluminum window is independent of the pressure in the tank. The exposure dose rate is proportional to the ionization current per atmosphere extrapolated to an infinite field and corrected for air attenuation, i.e., to $I_\infty e^{Pd\mu}/P$. Here I_∞ is the current at infinite field, P is the pressure in atmospheres, d is the distance between the center of the collector plate and the entrance window, and μ is the linear absorption coefficient of the gamma rays in air. Values of $I_\infty e^{Pd\mu}/P$ at different pressures are listed in table 1 for cesium-137 gamma rays. These results verify the earlier conclusion that a proper extrapolation is obtained for a value of c between 1.24×10^{-4} and 10^{-5}. As the extrapolated values for $c=2.5\times10^{-5}$ show a slightly smaller deviation from the average than $c=3.2\times10^{-5}$, this value is used for all subsequent determinations for both the cesium-137 and the cobalt-60 source.

TABLE 1. $10^{11}\frac{I_\infty}{P}e^{Pd\mu}$ *for cesium-137*

Pressure	c 1.24×10^{-4}	3.2×10^{-5}	2.5×10^{-5}	10^{-5}
atm				
10.75	1.956	1.992	2.005	2.054
8.457	1.977	1.997	2.009	2.045
6.70	1.990	2.013	2.018	2.041
4.797	2.001	2.015	2.018	2.030
3.965	1.998	2.002	2.004	2.013
Average		2.004 ± 0.008 [a]	2.011 ± 0.006 [a]	

[a] Mean deviation.

The computations of $e^{Pd\mu}$ assume that the photons which generate the electrons are attenuated for a distance, d, in air. Actually, most of the electrons which produce the ionization in the collecting region are generated before and a few after the photons reach the collecting region. The amount by which d must be reduced because of this is the distance, a, from the center of the collecting region to the mean position of origin of the electrons producing ionizations in the collecting region. As the value of a is nearly a constant fraction of the distance for electronic equilibrium for the photon energies considered here, it is convenient to first determine the distance[7] for electronic equilibrium. These distances for the two sources may be obtained from the thread chamber data.

Results obtained with the thread chamber for cesium-137 gamma rays at 6.7 atm are shown in figure 5 and for cobalt-60 gamma rays at 12 atm in figure 6. The solid curves give the ionization current to the outer collector ring for different positions of each Bakelite sheet with the other sheet positioned as close as possible to the collecting region; the dotted curves are for the ionization current to the central collector. Initially the solid curves rise rapidly with the distance between the sheet and the collecting region, but eventually reach a plateau. The rise indicates that electrons generated at larger distances from the collecting plane are

[7] This distance is also necessary for free air chamber design.

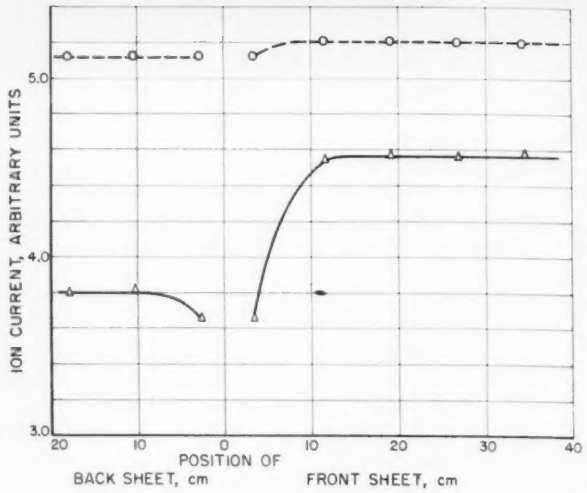

FIGURE 5. *Data obtained from the thread chamber and cesium-137 gamma rays at 6.7 atm.*

[a] The solid curves give the ionization current to the outer collecting ring and the dotted curve to the center electrode.

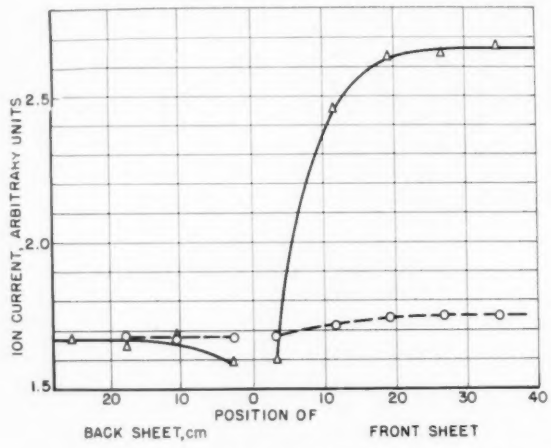

FIGURE 6. *Data obtained from the thread chamber and cobalt-60 gamma rays at 12 atm.*

The solid curves give the ionization current to the outer collecting ring and the dotted curve to the center electrode.

contributing to the ionization. The distance at which the ionization becomes constant is the distance for electronic equilibrium. From the solid curves it appears that the distance required for electronic equilibrium with cobalt-60 gamma rays is about 350 cm-atm in front of the collector and about 180 cm-atm behind the collector. The corresponding distances for cesium-137 are 90 and 50 cm-atm. Aglintsev and Ostromukhova [15] also obtained a distance of about 350 cm-atm for cobalt-60 gamma rays.

The mean distance from the collecting region to the mean position of origin of electrons producing ionization in the collecting region is, of course, less than the equilibrium distances. Calculations by Roesch [16] indicate the distance from the collecting region to the mean position of origin of the electrons is about 0.3 times the distance for electronic equilibrium. Aglintsev and Ostromukhova [15] computed

values of 0.36 for cobalt-60 and 0.34 for cesium-137 gamma rays. For these distances in a free-air chamber they compute the transmission, $K=e^{-Pa_\mu}$, of cesium-137 and cobalt-60 gamma rays to be 0.996 and 0.992, respectively. In a carbon-walled cavity chamber, because of the lower effective absorption coefficient there, these transmissions are 0.998 and 0.995. These factors must be multiplied by e^{Pd_μ} in order to obtain the attenuation of the photons whose electrons produce the measured ionization.

The attenuation cofficients for the gamma-ray beams are computed from data obtained for plates 2 and 9. The difference in the currents obtained with the tube out and with the tube in, after correction for the shadowing and saturation, gives the current produced by the primary beam. The ratio of the plate-2-to-plate-9 currents are given in table 2 for different pressures with the two sources. The linear absorption coefficient computed from the ratio and that given by Grodstein [17] are also shown. The maximum deviation of the computed absorption coefficient from the mean is approximately 6 percent and the maximum difference between the experimental and theoretical values is also 6 percent. The first number indicates that the precision of the current ratio is at least 0.5 percent and the second that the systematic errors if they exist for two current determinations are equal within the precision of measurement. As there is no reason to assign different precisions to the two current determinations, the precision of each is about 0.35 percent.

TABLE 2. *Air absorption coefficient*

Source	Pressure	$\frac{I_2}{I_9}$	μ cm^{-1}	
			Experiment	Grodstein [17]
	atm			
Cs^{137}	10.75	1.094	1.04×10^{-4}	1.0×10^{-4}
	8.45	1.068	0.96×10^{-4}	
	6.70	1.057	1.04×10^{-4}	
	4.79	1.042	1.06×10^{-4}	
Co^{60}	12.27	1.076	7.5×10^{-5}	7.3×10^{-5}
	10.75	1.069	7.7×10^{-5}	

Possible scattering from the diaphragm is investigated by obtaining data with both a 15 cm and a 22½ cm long diaphragm. The radiation scattered through the diaphragm and into the chamber from the source holder is decreased slightly by lengthening the diaphragm. However, this decrease is estimated to be less than 0.1 percent of the electron contribution to the ionization. Such a small decrease is not observable from the tube-out measurement as this is less than the precision. Large angle scattering from the shutter-diaphragm is considerably attenuated by the steel surrounding the entrance window of the pressure tank. Probably for this reason no difference is obtained in the current to plate 7a and 7b when the diaphragm length is increased. Currents to plates 5a, 5b, 6a, and 6b are decreased slightly (0.1% of the electron contribution) as the diaphragm length is increased for the tube-out measurement. There is a similar decrease for the tube-in measurement. Therefore, the differences in the tube-out and tube-in measurements are independent of diaphragm scattering.

From the measured currents to plates 4, 5, 6, and 7, it is possible [14] to compute the loss in ionization (electron loss) obtained beyond different radii and also the contribution to the ionization provided by the scattered photons. In order to compare the results obtained at different pressures for each source, the radii at each pressure are corrected for the diameter of the gamma-ray beam [13] and for the density of the air. The abscissa of figures 7 and 8 is in equivalent centimeters at 1 atm for a zero diameter beam. It is seen that the data of figure 7 agree to within about ±0.2 percent for different pressures and that the data of figure 8 agree to within about ±0.1 percent for different pressures.

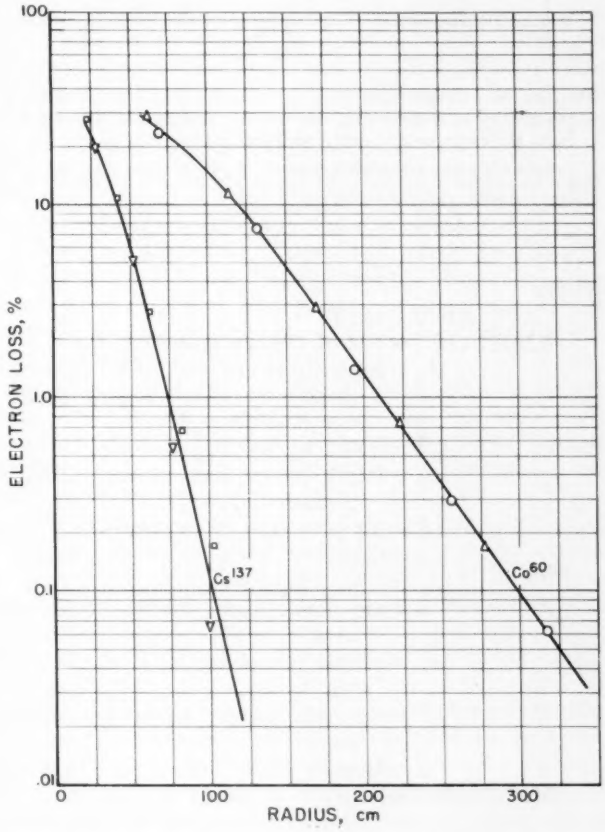

FIGURE 7. *The loss of ionization from primary photons beyond different radii for cobalt-60 and cesium-137 gamma rays.*

Results have been corrected to 1 atm and for the beam diameter. Results with cesium-137 at 3.96 atm = ⊡, at 4.797 atm = ▽; with cobalt-60 at 12.27 atm = ⊙, at 10.75 atm = △.

The gamma ray output, G, in roentgens per hour at 1 m (rhm) for each source is obtained by substituting numerical values in eq (1).

$$G=\frac{(3{,}600)\,(2.998)\,(10^9)\,I_\infty b^2 K\, e^{Pd_\mu} e^{0.08\mu}\mathrm{Al}\; e^{100(b+0.40)\rho_\mu/0.001293}}{PADL}\ \mathrm{rhm} \qquad (1)$$

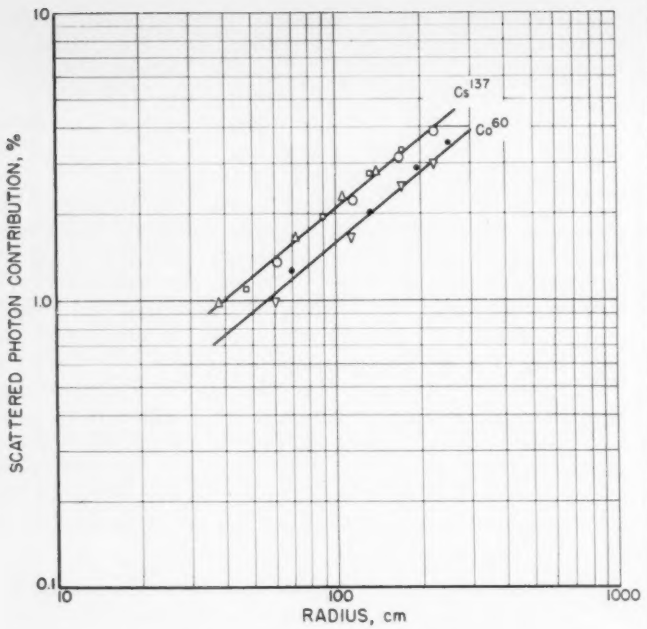

FIGURE 8. *Contribution of secondary photon ionization in percent of total primary electron ionization for different radii from the cesium-137 and cobalt-60 beam.*

Results have been corrected to 1 atm and for the beam diameter. Results with cesium-137 at 10.75 atm = ⊙, at 8.45; atm = ⊡, at 6.70 atm = △; with cobalt-60 at 12.27 atm = ⊙, at 10.75 atm = ▽.

where

$3{,}600$ = sec hr^{-1},

$(2.998)\ (10^9)$ = esu of charge coulomb^{-1},

I_∞ = ionization current in amperes produced by the primary beam in the collecting region,

b = 0.871 m (see fig. 1),

K = 0.992 for cobalt-60 and 0.996 for cesium-137,

P = air pressure in atmospheres,

d = distance from collecting region to entrance window, 133.9 cm,

μ = air absorption coefficient in cm^{-1} atm^{-1},

μ_{Al} = aluminum absorption coefficient in cm^{-1},

$e^{100(b+0.40)\rho\mu/0.001293}$ = air absorption correction between source and window,

ρ = density of laboratory air in g cm^{-3},

0.001293 = density of air at a pressure of 760 mm mercury and a temperature of 0° C in g cm^{-3},

A = measured area of aperture of diaphragm, 3.147_8 cm,

$D = \dfrac{\text{effective area of aperture}}{A}$, and

L = collector length (20.15 cm).

The effective area of the aperture is greater than the area A because of photon leakage through the edges of the aperture [3]. The computed factor, D, allows for this leakage.

Table 3 gives the rhm for each of the sources computed from the equation with the data obtained with the pressure chamber.

TABLE 3. *Output determinations*

Source	Free-air chamber	Cavity chamber	Difference
			%
Co^{60}	0.756 rhm	(1.003)[a] 0.758 rhm	0.3
		(1.016)[a] 0.768	1.6
		(1.003)[a] 0.758	0.3
Cs^{137}	2.61_1	(1.007)[a] 2.56_9	1.6
		(1.026)[a] 2.61_5	0.3
		(1.013)[a] 2.58_6	1.0

[a] The numbers in parentheses are the ratio of the stopping power of carbon to that of air for "Bakker-Segre," "Caldwell," and "NCRP" mean excitation potentials, respectively, for each of the sources.

The carbon cavity chamber previously used by Attix and Ritz [4] is also used to measure the sources. The largest single uncertainty in such a determination is in the stopping power. Attix and Ritz have indicated two sets of values for the mean excitation potential to be used in the stopping power equation. For one set, labeled "Bakker and Segre," they give 76.4 and 80.5 ev for carbon and air respectively; for the other set, labeled "Caldwell," they give 78 and 94.9. An analysis by a task group of the National Committee on Radiation Protection and Measurements [18] of the information presently available provides values of 78.4 and 85 ev for carbon and air respectively. The resulting stopping power ratios (in parentheses) obtained after taking into account the density correction and the outputs determined from the cavity chamber data for each are listed in table 3.

The emission constant of the cobalt-60 source may also be computed. The activity in curies is obtained from the measured value of Minton [19] with a radioactive decay correction. Corrections are also applied to the values in table 2 for photon absorption in the aluminum capsule (1.011) and in the cobalt-60 cylinder (1.030). The resultant emission constant is 12.7_3 r cm^2 mc^{-1} h^{-1}. The theoretical value for this constant is 12.9 if the average energy to produce an ion pair is 34.0 ev. In view of the uncertainty in the activity determination (1%) and the uncertainty in the decay correction for the four years between the activity and ionization-chamber determinations, the agreement seems reasonable.

4. Accuracy

In order to assign an accuracy to the free-air and cavity-chamber values in table 3, it is necessary to review the accuracy of each of the factors used in determining the values. These factors are listed in table 4.

The error for item 1 is estimated from the reproducibility of individual measurements. Part of this fluctuation is caused by slight drifts in the collecting and bucking potentials and possibly from charging of some of the insulators.

TABLE 4. *Possible errors in rhm determinations*

Item	Errors due to	Percent error	
		Pressure chamber	Cavity chamber
1	Ionization measurements [a]	[a] 0.2	[a] 0.1
2	Time, capacitance, and potential	.1	.1
3	Voltage saturation	[b] .3	<.1
4	Air absorption	.1	<.1
5	Window absorption	.1	
6	Plate separation correction	.1	
7	Air pressure	.1	<.1
8	Temperature	.1	.1
9	Effective collector length [c]	.2	
10	Diaphragm area	.1	
11	Diaphragm leakage	.2	
12	Chamber volume		.1
13	Diaphragm-to-source distance	<.1	.2
14	Scattered radiation and chamber wall alternate		.3
15	Scattered photon contribution	.1	
16	Electron contribution	.2	
17	K	.2	.2
18	Stopping power ratio		.5

[a] Of individual points.
[b] Including relative measurement of currents for different pressures but not correction for error for item 2.
[c] Including field distortion.

The timing accuracy depends principally on the difference in action time of two relays [12]. An investigation indicates that the accuracy is about 0.01 percent for the times used here. The condenser and potentiometer are each calibrated to an accuracy of 0.05 percent but the capacitance drifted during the experiment by almost 0.1 percent. However, it does not seem probable that the determination of the charge collected on the condenser is in error by more than 0.1 percent (item 2).

The accuracy of the saturation extrapolation depends on the adequacy of the Jaffé-Zanstra theory. Each extrapolation is obtained by a least squares fit so there is no subjective error. The amount of extrapolation at 3.96 atm for cesium-137 is only about 1½ percent. However, the constancy of $(I_\infty e^{Pd\mu}/P$ in table 1 for cesium-137 and similar values for cobalt-60 (which agree to within $\pm 0.15\%$) indicates that the error in extrapolation is not likely to be over 0.3 percent (item 3). For the cavity chamber the extrapolation is only 0.1 percent so the uncertainty must be small compared to 0.1 percent.

The air attenuation between plates 4 to 7 and the source varies from about 7 percent to 17 percent for cesium-137 and is about 12 percent for cobalt-60. The distance used in the computation is known to at least 0.1 percent. There appears to be no accurate experimental determination of the absorption coefficient for air although the values for aluminum agree with theory to within a few tenths of a percent for the sources considered here. Therefore, it seems reasonable not to expect an error of more than 0.1 percent for item 4 because the maximum correction for air absorption is only about 17 percent for the pressure-chamber measurement. For the cavity-chamber measurements, the maximum correction is only about 0.7 percent so the uncertainty in this item should be negligible.

The absorption in the aluminum window of the pressure chamber is of the order of 1 percent. It is difficult to imagine that variations in thickness, absorption coefficient, or composition could cause uncertainties of more than 0.1 percent (item 5).

Several extrapolations for inadequate plate separation were tried. For any reasonable assumption on this extrapolation, the uncertainty is probably not more than 0.1 percent (item 6). The small variation with pressure indicated in figures 7 and 8 corroborates this.

The density of air in the pressure chamber is determined from the gage pressure and temperature in the tank and the barometric pressure and room temperature. Errors in the room pressure and temperature could cause less than 0.1 percent error in the air density within the tank at the pressure used. However, as the gage could be calibrated to only ± 0.1 psi and it was not calibrated at the exact pressures used, there is a possible uncertainty of the pressure of about 0.1 percent at the higher pressures (item 7). The same uncertainty is estimated for measurements below 5 atm where the mercury manometer is used. Temperature fluctuation in the tank as indicated by the thermocouples could not have caused an uncertainty in the density determination of more than 0.1 percent (item 8).

For the cavity-chamber measurements, the air pressure is given by a barometer calibrated to 0.1 mm and the pressure was very constant during a set of measurements. Thus, the error in item 7 should be less than 0.1 percent. However, the temperature did vary by about ± 0.1 percent during a set of measurements so a possible error of 0.1 percent is assumed for item 8.

The effective length of the collector plate is determined by the measured length and by any field distortion caused by the presence of the grounded tank and by warpage of the plates. The measured length could not be in error by as much as 0.1 percent but, as indicated earlier, the distortion produced by the grounded tank is determined by ionization means. Therefore, the reproducibility of the ionization measurements (0.1 % for this investigation) determines this possible error. From previous work [11] it appears that the warpage of the plate could produce an uncertainty of no more than 0.1 percent. Therefore, for these two possible errors it is estimated that the effective plate length could not be in error by more than 0.2 percent (item 9).

The diaphragm area is determined by measuring four radii at different depths. These measurements show the hole to be slightly coned (about 3 parts in 7,800) at the two ends, but at any one depth the radii agree to 8 parts in 78,000. The uncertainty in the physical determination of the hole area is therefore not more than 0.1 percent (item 10).

The effective area of the diaphragm is slightly larger than the hole area because of leakage of radiation through the edge of the holes [3]. The increased area amounts to about 1.8 percent for cesium-137 and about 3.5 percent for cobalt-60 radiation. It is estimated that the uncertainty

[3] in this leakage could not cause an error of more than 0.2 percent (item 11).

The uncertainty in the cavity chamber volume (item 12) is assumed to be the same as that estimated by Attix and Ritz [5] (0.1%).

The distance between the collimator and the source (87.1 cm) is determined by a cathetometer and vernier calipers reading to 0.1 cm. It is estimated that the error introduced by the uncertainty of this distance is less than 0.1 percent (item 13). However, the uncertainty of the source-to-cavity-chamber distance is somewhat larger—about 0.2 percent.

The accuracy of the correction for scattering from the walls of the room and from the cavity-chamber walls, and for the photon attenuation in the wall is estimated to be the same as that given by Attix and Ritz [5] (item 14).

The computed scattered photon contribution to the ionization for cesium-137 gamma rays amounts to about 4 percent of the electron contribution at 10.85 atm and about 2 percent at 3.96 atm; for cobalt-60 this contribution amounts to about 3½ percent for the pressures used. The agreement (see fig. 8) in the scattered photon contribution obtained at various pressures for a given radiation indicates that it is reproducible to about 0.1 percent (item 15).

The agreement (see fig. 7) in the electron contribution obtained at different pressures indicates that this quantity is reproducible to about 0.2 percent (item 16).

The theoretical values of K determined for cobalt-60 gamma rays by Roesch [16] are about 0.3 percent larger than those determined by Aglintsev and Ostromukhova [15]. Values obtained by Aglintsev and Ostromukhova are used here, but the uncertainty of this correction (item 17) has been assigned a value of 0.2 percent.

Probably the largest single uncertainty in the output determination by the cavity-chamber is in the stopping power ratio (item 18). Three different values for carbon-walled air ionization chambers have been suggested recently. The maximum difference between them is about 2 percent. However, the values labeled "Caldwell" in table 3 do not fit the data of Attix and Ritz [5] and of Whyte, who conducted experiments with cavity chambers having walls of different atomic number. The experimental data from these authors fit the "Bakker and Segre" and "NCRP" stopping-power ratios slightly better than those of "Caldwell" but neither obtained a direct measurement of the stopping power for air. The data of table 3 also indicate better agreement between the free-air chamber and cavity chamber for the "Bakker and Segre" and "NCRP" stopping-power ratios with the cobalt-60 source but poorer with the cesium-137 source. Attix and Ritz estimate the accuracy of the stopping-power ratios as 0.3 percent, but Whyte gives a value of 0.5 percent. The latter has been adopted for the present report.

The maximum possible error is obtained by adding the errors of item 2 through 18, and is 1.9 percent for the pressure chamber and 1.5 percent for the cavity measurements. Item 1 is greatly reduced by the multiplicity of observations. If one assumes that all of these items give random errors, the square root of the sum of their squares gives 0.6 percent for the pressure-chamber method and about 0.7 percent for the cavity-chamber method.

5. Summary

1. By a proper choice of the constant in the Jaffé-Zanstra method of extrapolating the ionization current to an infinite field strength, it has been shown that consistent saturation currents can be computed from ionization measurements made with noninfinite fields, at least for pressures of 4 to 12 atm in air. However, the best constant seems to be somewhat different than that previously used. It has also been shown that field strengths per atmosphere of greater than 85 and probably greater than 114 vcm^{-1} atm^{-1} are needed for the Kara-Michaelova and Lea extrapolation technique.

2. Design data for the construction of free-air chambers used in the measurement of cesium-137 and cobalt-60 gamma rays in roentgens are presented.

3. Determination of the gamma-ray output from a cesium-137 and a cobalt-60 source by means of a free-air chamber and a cavity chamber are indicated. The experiments are not sufficiently accurate to unambiguously decide which value of stopping-power ratios should be used.

4. It would seem from the estimate of errors that the uncertainty in the two methods of measurement is approximately the same and, therefore, that neither can be designated as the standard method.

The author thanks T. P. Loftus, who made all of the cavity chamber measurements; F. H. Attix, with whom many of the problems arising during the investigation were discussed; and G. H. Dempsey, who was of great assistance in setting up the equipment.

6. References

[1] International commission on radiological units and measurements, 1956 Rept., NBS Handbook **62,** (1957).

[2] G. W. C. Kaye and W. Binks, The ionization measurements of γ-radiation, Proc. Roy. Soc. (London)**A161,** 564 (1937).

[3] L. S. Taylor et al., Measurements in roentgens of the gamma radiation from radium by the free-air ionization chamber, Am. J. Roentgenol. Radium Therapy Nuclear Med. **44,** 428 (1940); also J. Research NBS **24,** 247 (1940).

[4] G. R. Grove, Measurement of cesium-137 and cobalt-60 gamma radiation with a pressure ionization chamber, J. Research NBS **48,** 147 (1952).

[5] F. H. Attix and V. H. Ritz, A determination of the gamma-ray emission of radium, J. Research NBS **59,** 293 (1957).

[6] W. Miller and R. J. Kennedy, Measurement of field distortion in free-air ionization chambers by an analog method, J. Research NBS **55,** 291 (1955).

[7] H. Zanstra, Ein kurzes verfahren zur bestimmung des sättigungsstromes nach der Jafféschen theorie der kolonnenionistron, Physica **2,** 817 (1935).

[8] L. S. Taylor, G. Singer, and A. L. Charlton, Measurement of super voltage X-rays with the free-air ionization chamber, J. Research NBS **21,** 19 (1938).
[9] J. W. Boag, Ionization chambers, Radiation Dosimetry (Academic Press, New York, N.Y., 1956).
[10] E. Kara-Michaelova and D. E. Lea, The interpretation of ionization measurements in gases at high pressures, Proc. Cambridge Phil. Soc. **36,** 101 (1940).
[11] H. O. Wyckoff and F. H. Attix, Design criteria for free-air ionization chambers, NBS Handbook **64** (1957).
[12] L. Costrell and F. H. Attix, Automatic timer simplifies small-current measurement, Nucleonics **15,** No. 2, 83 (1957).
[13] H. O. Wyckoff and F. S. Kirn, Standard ionization-chamber requirement for 250 to 500 kilovolt X-rays, J. Research NBS **58,** 111 (1957).
[14] F. H. Attix and L. DeLaVergne, Plate separation requirements for standard free-air ionization chambers, J. Research NBS **53,** 393 (1954).
[15] K. K. Aglintsev and G. P. Ostromukhova, Ionization distribution along the gamma-ray beam and reproduction of the roentgen by means of a standard ionization chamber, Atomnaya energ. **6,** 63 (1959).
[16] W. C. Roesch, Dose for nonelectronic equilibrium conditions, Radiation Research **9,** 399 (1958).
[17] G. White Grodstein, X-ray attenuation coefficients from 10 kev to 100 Mev, NBS Circ. **583** (1957).
[18] W. C. Roesch (private communication).
[19] G. Minton (private communication).
[20] G. N. Whyte, Measurement of the Bragg-Gray stopping power correction, Radiation Research **6,** 371 (1957).

Washington, D.C. Paper (64C2–28)

JOURNAL OF RESEARCH of the National Bureau of Standards—C. Engineering and Instrumentation
Vol. 64C, No. 2, April–June 1960

Apparatus for the Measurement of the Normal Spectral Emissivity in the Infrared

Arthur G. Maki, Ralph Stair, and Russell G. Johnston

(December 21, 1959)

Apparatus and methods are described for measuring in the infrared the normal spectral emissivity of metals and coatings or oxides which tightly adhere to metals. Examples of the use of this apparatus are given in measurements of the emissivity of platinum and of oxidized Inconel within the spectral region of 1.5 to 15 microns. Measured values were reproduced to better than 5 percent.

1. Introduction

The measurement of the spectral emissivity of heated substances may be accomplished by comparing the energy emitted by the substance under study with that emitted by a standard substance for radiation at various wavelengths. For such a standard one usually uses a blackbody, that is, a hollow body provided with a hole for viewing the radiation inside. The inside surface of the blackbody must be maintained at a uniform temperature. The wavelength separation may be accomplished using a double-beam monochromator or a single-beam monochromator.

The specimen under investigation may be formed into a rod, bar, ribbon, or other shape. Some workers have even formed the specimen into a blackbody. For such a specimen both the inside surface (the blackbody) and the outside surface (the specimen) are observed.

The double-beam monochromator and associated method have certain advantages especially with relation to the elimination of the effects of absorption by carbon dioxide and water vapor, but the optical adjustment is critical as compared with a single-beam instrument. Furthermore through the use of a single set of optics and equal path lengths in the single-beam monochromator the effects of both atmospheric absorption and differential reflectivity in the auxiliary optics are practically eliminated. The apparatus described herein is of the latter type.

The specimen may vary in temperature from point to point depending upon its shape, size, and method of heating. If made into the form of a blackbody the inside temperature may differ from that on the outside. A convenient shape is that of a long thin ribbon heated electrically by contacts at the two ends. The data presented in this paper apply to samples of this type for which the temperature is measured by means of thermocouples in metallic contact with the opposite face from the point of radiant energy measurement.

2. Apparatus and Method

This apparatus was set up as shown in figure 1. The blackbody and sample under investigation were mounted side by side on an optical bench (constructed from a lathe bed and table) so they could be alternately placed at the focal point of the optical system. The auxiliary optics, consisting of a plane and a spherical mirror (65-cm radius of curvature), were mounted rigidly on the monochromator base. The placing of the sample and blackbody aperture alternately at the same position ensured essentially equal light paths and the use of identical optics.

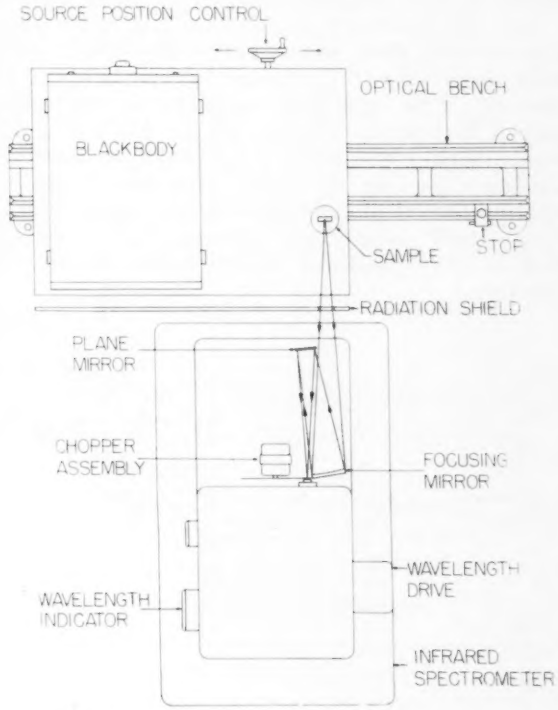

FIGURE 1. *Instrumental setup for the measurement of the normal spectral emissivity of heated substances.*

A single-beam monochromator incorporating a sodium chloride prism and thermocouple was modified to yield the arrangement shown in figure 1 for use in this work. It was calibrated for wavelength in the usual manner by using atmospheric and polystyrene absorption bands. The light beam was chopped at 10 cps and the thermocouple voltage amplified through the use of a ten-cycle thermocouple amplifier giving an approximately linear output.

The linearity of the amplifier was of importance as the emissivity was obtained as the ratio of the measured outputs for the blackbody and specimen, both being maintained at the same temperature. For the high emittance measurements the linearity of the amplifier was checked using filters of known transmission. In the case of the low-emissivity measurements an attenuator switch was used to bring the blackbody and specimen readings within a comparable range. This attenuator was then calibrated by comparing the measured values of the radiant energy from a blackbody at a high temperature with those from the blackbody at a lower temperature. Using the Planck blackbody radiation equation the ratio of the radiation from these two sources was calculated and used to calibrate the amplifier and attenuator.

In this work the wavelength bandwidth (half intensity width) averaged about 0.15 μ although it varied somewhat with the wavelength setting.

The blackbody cavity was constructed of an alloy casting of essentially 80 percent nickel–20 percent chromium (3 in. outside diam. by 6 in. in length, with a wall thickness of about ½ in.). The low reflectivity of this (oxidized) metal coupled with the fact that the aperture was only 0.3 percent of the interior surface area resulted in a blackbody of extremely high effective emissivity (probably 0.999 or above). The high heat capacity of the furnace employed in heating the blackbody gave it a high thermal stability and made manual temperature regulation easy (see fig. 2). The large size of the furnace, the method of heating, and the small furnace aperture used to permit viewing the blackbody yielded a very uniform temperature within the blackbody.

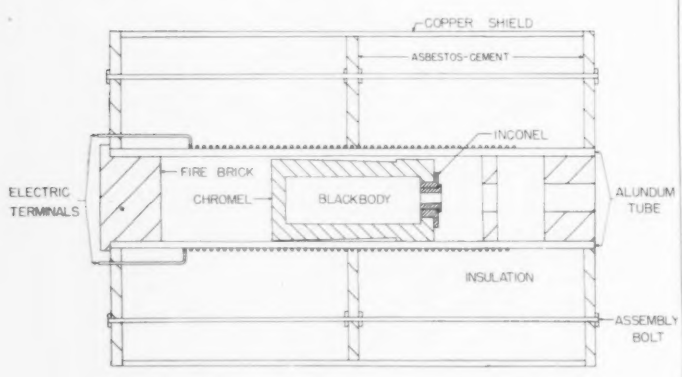

FIGURE 2. *Blackbody and furnace cross section.*

The temperature of the blackbody, as well as that of the sample under investigation, was measured through the use of platinum versus platinum–10 percent-rhodium thermocouples. Checks against standard thermocouples indicated that the absolute temperatures of the blackbody recorded herein are correct to within about $\pm 6°$ K.

The specimen consisted of a metal strip about 8½ in. long by ¼ in. wide and about 1/32 in. thick. The thermocouple used to measure the specimen temperature was welded to the back side of it directly behind the surface area from which the measurements were made. The thermocouple used was of rather small diameter wire (5 mils) so that the cooling of the surface which resulted from conduction along the thermocouple wire was quite small. The useful radiating surface area was about ⅜ in. by 1/16 in. and the radiation used was essentially normal to the surface. Observations with an optical pyrometer indicate that the temperature gradient over the observed surface was less than $\sim 4°$ K.

The specimen under examination was heated by passing through it an electric current of about 80 amp at 5 v. It was clamped rigidly at the two electrodes and held centrally located within a water-cooled metal tube, about 1¼ in. inner diameter. Although the inner surface of this tube was highly oxidized, reflection from its inner surface affected the emissivity measurements by about 1 percent. However, its use reduced air currents and added greatly to the stability of the temperature of the sample so that its temperature could be manually held constant within about $\pm 1.5°$ K even at 1,400° K.

3. Examples of the Use of This Apparatus

As examples of the use of this apparatus, the emittances of two very different substances, platinum and oxidized Inconel, were measured. The oxide coating on Inconel has a very high spectral emittance while the surface of platinum being highly reflective has a very low emissivity.

3.1. Oxidized Inconel

The Inconel strips were prepared by first cleaning the surface by sandblasting, and then heating in air for 6 hr at a high temperature in order to form an opaque oxide coating.

The spectral emittance of oxidized Inconel is given in table 1 and figure 3. These data are the average of the values obtained on three separate specimens each of which was run several times at each temperature.

The oxide coating has a very high emissivity as is characteristic of many oxides. The most prominent features of the emissivity curve are two minimums at around 6 and 6.5 μ. In this same wavelength region there are two strong absorption maximums for atmospheric water vapor. Although care was exercised to make the pathlengths for blackbody and specimen equal, the atmospheric absorption may be the cause of these minimums.

TABLE 1. *Normal spectral emittance of oxidized Inconel at 1,400° K, 1,050° K, and 780° K from 1.5 to 15 μ*

Wavelength	1,400° K	1,050° K	780° K
μ			
1.5	0.93	0.88	0.77
2.0	.92	.88	.79
2.5	.91	.86	.78
3.0	.90	.86	.77
3.5	.90	.85	.78
4.0	.90	.85	.78
4.5	.90	.84	.78
5.0	.90	.84	.77
5.5	.89	.83	.77
6.0	.86	.80	.72
6.5	.86	.80	.74
7.0	.88	.84	.78
7.5	.90	.87	.82
8.0	.91	.90	.85
8.5	.91	.90	.87
9.0	.92	.90	.87
9.5	.92	.90	.86
10.0	.92	.89	.86
10.5	.92	.90	.87
11.0	.92	.90	.88
11.5	.93	.91	.88
12.0	.94	.92	.89
12.5	.95	.93	.91
13.0	.95	.94	.92
13.5	.96	.94	.93
14.0	.96	.94	.90
14.5	.96	.94	.89
15.0	.96	.94	.87

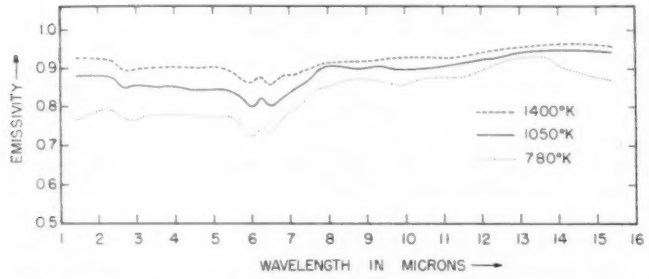

FIGURE 3. *Normal spectral infrared emissivity of oxidized Inconel at selected temperatures.*

Figure 3 shows the very distinct trend for the emissivity to increase with temperature. Many nonmetals seem to show very little change in emissivity with temperature. The change which we have observed, however, is attributed to the oxide coating because previous experiments indicate that coatings formed in the manner described are opaque to any radiation from the underlying metal. Moreover, although metals are expected to show such an increase in emissivity with temperature, the emissivity of metals is too low to be a contributing factor.

3.2. Platinum

The two platinum strips examined were first annealed by heating to about 1,525° K. One specimen was held at that temperature for 1 hr while the other was heated for only 10 min. Both specimens, although initially smooth surfaced, acquired a crystalline appearance after the annealing process. This crystalline surface would probably have a slightly different emissivity from a perfectly smooth surface, but infrared radiation, since it has relatively large wavelength, is rather insensitive to small surface irregularities.

The emissivity of the platinum strip is given in table 2 and the results are shown in figure 4. The low emissivity is characteristic of most metals. This follows from the fact that the reflectivity of metals is very high.

Price [1][1] measured the spectral emissivity of platinum at 1,400° K over the wavelength range of 0.65 to 4.75 μ. Price reported that due to the nonperfect blackbody which he used his emissivity values, if in error, were probably too high. This may account for the fact that our values are everywhere lower than Price's.

TABLE 2. *Calculated and observed values of the normal spectral emissivity of platinum at 1,400° K from 1.5 to 15 μ*

Wavelength	Calculated emissivity	Observed emissivity
μ		
1.5	0.189	0.197
2.0	.165	.179
2.5	.149	.154
3.0	.137	.139
3.5	.127	.128
4.0	.119	.117
4.5	.112	.108
5.0	.107	.100
5.5	.102	.094
6.0	.098	.090
6.5	.094	.088
7.0	.091	.090
7.5	.088	.092
8.0	.085	.093
8.5	.083	.091
9.0	.081	.091
9.5	.078	.090
10.0	.077	.087
10.5	.075	.083
11.0	.073	.080
11.5	.072	.078
12.0	.070	.075
12.5	.069	.072
13.0	.067	.068
13.5	.066	.066
14.0	.065	.064
14.5	.064	.063
15.0	.063	.065

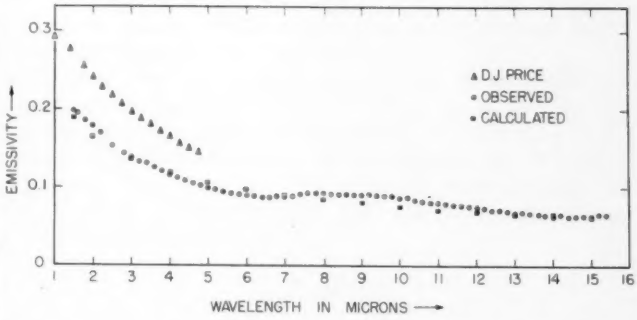

FIGURE 4. *Normal spectral infrared emissivity of commercial grade platinum at 1,400° K.*

Observations by D. J. Price shown by triangles (△); calculated emissivity shown by squares (□).

[1] Figures in brackets indicate the literature references at the end of this paper.

In the long wavelength region the emissivity of metals increases with increase in temperature. This fact has been verified for platinum by Hagen and Rubens [2]. Thus our results should be higher than measurements made at lower temperatures. As expected the reflectivity values for platinum at lower temperatures reported by other workers yield emissivity values lower than ours.

The measured spectral emissivity values for platinum may be compared with the theoretical emissivity calculated by using the Drude-Zener relation. This is valid only for metals for which the electrons are perfectly free. According to this relationship [3] the long wavelength spectral emissivity is given by

$$\epsilon = 0.365\left(\frac{\rho}{\lambda}\right)^{\frac{1}{2}} - 0.0464\frac{\rho}{\lambda}.$$

Here ρ is the electric resistivity of the metal in ohm centimeters and λ is the wavelength in centimeters. Table 2 and figure 4 include the theoretical emissivities calculated using this equation and the resistivity value 46.52 μohm cm measured at 1,400° K by Wm. F. Roeser [4].

At long wavelengths the measured emissivity is in excellent agreement with the theoretical values. There is, however, an unexpected rise in the observed values around 8, 9, and 10 μ. This may be due to very small amounts of impurities on the surface of the metal. The deviation at shorter wavelengths may be partially due to the fact that the theoretical curve is expected to apply only to the long wavelength region.

4. Conclusion

The apparatus described in this paper may be used to measure the emissivity of metallic substances or substances capable of forming tightly adhering coatings on metals to within about ± 3 percent for substances with a high emittance and to about ± 5 percent (of measured value) for substances with a low emittance. For highly emissive substances the temperature measurement is probably the principal source of error while for low-emittance specimens the amplifier stability becomes a major source of error. The reproducibility of the results has been found to be very good. It was checked by making repeated measurements on the same specimen and on different specimens of the same material. In addition a different operator was used to check some of the work.

One could also measure the emissivity by changing the blackbody temperature so as to equate the radiation of sample and blackbody. The principal source of error would then be due to the temperature measurement for all emissivity values. A big disadvantage of this procedure is the slowness of making measurements due to the large thermal inertia of the blackbody.

In conclusion the authors express their gratitude to Wm. F. Roeser of the Building Technology Division for helpful suggestions; also to Fred Shorten for assistance in taking some of the observations.

5. References

[1] D. J. Price, Proc. Phys. Soc. (London) **59,** 118 (1947).
[2] E. Hagen and H. Rubens, Ann. Physik **11,** 873 (1909)
[3] Max Jakob, Heat transfer, vol. I (John Wiley and Sons, Inc., New York, N.Y.).
[4] Temperature; its measurement and control in science and industry, p. 1312 (Reinhold Publishing Corp., New York, N.Y.).

Washington, D.C. (Paper 64C2–29)

JOURNAL OF RESEARCH of the National Bureau of Standards—C. Engineering and Instrumentation
Vol. 64C, No. 2, April–June 1960

Electrostatic Deflection Plates for Cathode-Ray Tubes. I. Design of Single-Bend Deflection Plates With Parallel Entrance Sections. II. Deflection Defocusing Distortion of Single-Bend Deflection Plates With Parallel Entrance Sections.

Lothar Frenkel [1]

(March 5, 1959)

In section I, a plate design system is offered which allows rapid and accurate determination of mechanical plate parameters to achieve given electrical plate characteristics. The design is suitable for single-bend plates with parallel entrance sections. The design curves were calculated under the conventional assumptions of small deflection theory, but corrections for the entrance and exit fields are included. The method of calculating the curves and corrections is indicated in an appendix.

Section II deals with deflection defocusing of such plates, a convenient formula for calculating the defocusing distortions of single-bend deflection plates is derived and compared with experiment. This type of distortion is proportional to the square of the deflection angle and is shown to be sensitive to plate design. In general, long deflection plates give lower distortions while the most "economical" plates yield larger distortions. Post deflection is shown to lead to increased distortions.

I. Design of Single-Bend Deflection Plates With Parallel Entrance Sections

1. Introduction

Designing a cathode-ray tube is as much an art as a science; experience and the correct choice of compromises between various parameters are both important. Experience suggests that the best tubes are designed in close cooperation between instrument designers and tube engineers. In many instances the tube designer in these discussions has nothing to go by except his experience, and any information of a quantitative nature is welcome. Such information is provided for the gun performance, for instance, by the work of H. Moss [1],[2] and it is hoped that the design system offered here will contribute to establishing this kind of information for the design of plates.

The design of cathode-ray tube deflection plates of specific characteristics is complicated by the choice of parameters available. Thus the shape of the plate may range from parallel plates to continuously flared plates, and the initial spacings from 0.030 in. to 0.1 in.

Given a definite plate shape, one can solve the equation of motion and thus determine the sensitivity and scan. The converse is not true, however, and tube designers have long needed a method which enables them to decide on suitable compromises without having to check design possibilities by laborious experiment. The design method offered here has been checked in many experiments over a span of five years and has been found accurate within the limits imposed by mechanical tube assembly.

2. Qualitative Considerations

A successful cathode-ray tube is one which will allow the ultimate utilization of the characteristics of the vertical amplifier for which it was designed. Such amplifiers are generally limited in voltage swing and bandwidth by the capacitance of the load which they have to drive. The requirements on the cathode-ray tube are therefore to provide best deflection sensitivity consistent with the required scan, capacitance, and writing speed. The most sensitive plates would be flared in such a manner that the fully deflected beam smoothly follows the positive deflection plate. Such optimum plate shapes have been described in the literature [2].

In practice continuous curvature is difficult to obtain, and approximation by bending is preferred. For the present design, single-bend plates with parallel entrance sections have been chosen. Such plates approach the optimum very closely, particularly in scan-limited tubes, which are used in the most advanced applications.

3. Theory

The most important design characteristics of a plate pair are its inverse sensitivity (say, in volts per inch) and the scan (in inches). The product of these parameters determines the maximum potential difference applied to the plates.

[1] Formerly, Tektronics—Portland, Oregon. This work was done at the A. B. DuMont Laboratories in 1953 and 1954.
[2] Figures in brackets indicate the literature references at the end of section I.

When, as is usually the case, the plates are arranged symmetrically about the undeflected beam, then one-half of this potential, V_{max}, determines the dimensions of the plate. Consider the parallel section first, as in figure 1. We arbitrarily stipulate that the width of the beam, w, should be 2/3 s, where s is the spacing of the plates, and that ¼ of the beam should be cut off by the plate edge. The deflection at the exit end is then given by:

$$y_1 = s/3 = e/m \int_0^{t_a} \int_0^{t_x} (V_{max}/s)\, dt\, dt \qquad (1)$$

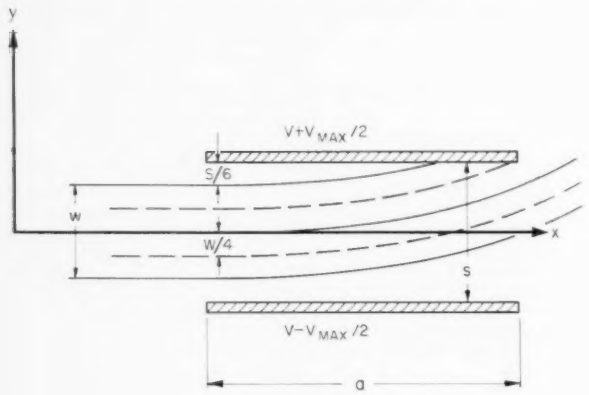

FIGURE 1. *The parallel section.*

where a is the length of plate. This equation serves to establish a as a function of s and V_{max}.

During transit in the flared section the beam is further deflected. The deflection due to the flared section alone gives, with reference to figure 2,

$$y_2 = e/m \int_c^{t_b} \int_c^{t_r} (V_{max}/\alpha r)\, dt\, dt, \qquad (2)$$

where we have assumed cylindrical field symmetry. The total deflection y_3 at the exit end of the combined plate is due to the deflection in each section plus the displacement in the flared section due to acceleration in the first, i.e.

$$y_3 = e/m \int_0^{t_a} \int_0^{t_x} (V_{max}/s)\, dt\, dt$$

$$+ e/m \left[\int_0^{a} (V_{max}/s)\, dt \right] t_{cb}$$

$$+ e/m \int_c^{t_b} \int_c^{t_r} (V_{max}/\alpha r)\, dt\, dt, \qquad (3)$$

where t_{cb} is the transit time from c to b. We now stipulate arbitrarily that at the exit end of the combined plate one-half of the beam should be cut off, i.e.,

$$y_3 = \alpha b/2. \qquad (4)$$

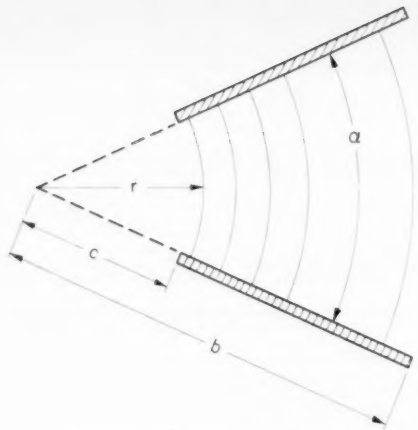

FIGURE 2. *The flared section.*

Thus, eqs (3) and (4) serve to give α as a function of s, a, V_{max}, and any arbitrary length of plate ($L = a + b - c$). In practice, α must be determined graphically. The sensitivity or inverse sensitivity may now be calculated for known screen distances. Additional assumptions, corrections, and the general formula are given in appendix 1 and 2. It should be noted that the determination of plate shape involves the simultaneous solution of eqs 1 to 4 and eq (a1) of appendix 3, after arbitrary decisions on spacing or length have been made.

On the other hand, the designs presented here are based on a large number of theoretical calculations in which the sensitivity was calculated as above after spacings, total lengths, and maximum voltages were arbitrarily chosen. As a result of calculating a large number of designs and tabulating the results, sets of curves are obtained which permit the selection of a plate shape for a given sensitivity and scan.

4. Method of Design

There are 3 sets of curves concerned with plate design parameters. All are based on the characteristic peak to peak plate cutoff voltage of 2 V_{max}. This may be defined as follows: Given a standard accelerating potential of 1 kv, $2V_{max}$ is the product of the desired total scan, times the inverse sensitivity (in volts per unit deflection).

The first set of curves A1 to A7 gives the inverse sensitivity as a function of $2V_{max}$. There are several sheets of curves each for a given total length of plate L. On each sheet there are several curves each for a specific entrance spacing s. The first set of curves thus serves to determine immediately what length and spacing are necessary to achieve a given scan and sensititivity.

The remaining two sets of curves B and C1 to C7 serve to establish the design completely by giving the length of the straight section and the angle of bend as functions of the parameter $2V_{max}$ and the length and spacing chosen from the first set. Thus it is not necessary to consult these sets for the initial discussion of a new cathode-ray tube design.

5. Post Acceleration

Post acceleration does not affect the value of V_{max} for a given plate but increases the inverse sensitivity by an amount variously called intensifier factor or compression factor. The factors vary depending on the bulb shape and the shape and the degree of continuity of the post accelerator. It differs also for the front and back plates of the same tube. To facilitate the design of post deflection accelerator tubes a set of curves D giving compression ratios for various tube types as a function of accelerator potential to anode potential ratio is included.

The compression factors for types quoted will apply approximately to all tubes of similar design. Type I has a straight-sided (T-shaped) bulb with 3 accelerator bands; type II has 1 accelerator band on a conical bulb; and type III uses a continuous accelerator in a bulb of exponential shape. For exact information the factors must be established experimentally for any given bulb shape, accelerator bands, and tube geometry. In general the continuous accelerator spiral gives the lowest loss in sensitivity.

6. Correction for Tube Length

The values of inverse sensitivity must be corrected by the ratio of the effective distance to the screen to the effective distance applicable for each sheet. This may be done as follows: The effective distance, with sufficient accuracy, may be taken as the distance of the screen from the exit end of the plate plus half the plate length. The distance D quoted on each sheet is the distance of the exit end of the plates on that sheet from the screen of the tube. The corresponding assumed effective distances therefore are greater in each case by about one-half of the plate length applicable to that sheet. The reason for this arrangement is that the design is needed mostly for the vertical plates of sensitive instrument tubes, and in considering the effect of changing plate lengths it is convenient to fit all designs to a standard length of tube.

7. Beam Width

The plate designs are based on an assumed beam width of ⅔ of the spacing s of the parallel section of the plates. If the limiting aperature size is taken in this manner cutoff is sharp and clean. For the highest performance types of tubes one might sacrifice edge performance, and values of ½ s for the diameter of the limiting aperture have been used in some tubes with consequent gain in brightness and definition in the center area of the screen.

Appendix I. Summary of Steps in Designing a Plate

1. *Establish the desired characteristics.* (a) Anode potential; (b) Post deflection accelerator ratio; (c) Desired inverse sensitivity; (d) Desired scan; and (e) Tube length.

2. *Find 2* V_{max}. Multiply the inverse sensitivity above by the desired scan.

3. *Normalize inverse sensitivity and 2* V_{max}. This is done by dividing both quantities by the anode potential in kilovolts.

4. *Adjust normalized inverse sensitivity for post deflection.* This is done by finding the compression factor from curves D and reducing the inverse sensitivity by it.

5. *Adjust normalized inverse sensitivity for tube length.* It is now necessary to select an approximate value of plate length and to find the corresponding value of D from the curves. The value for inverse sensitivity is then adjusted as outlined previously.

Steps 1 to 5 are easily accomplished, and the information is now available for a complete design.

6. *Establish a spacing* s *and complete design.* By consulting the set of curves A, a spacing may be selected for each of various possible plate lengths. This involves a compromise in terms of beam size, etc. When this choice has been made the straight length and bend angle may be found directly from the remaining two sets of curves. If it is found that the design chosen leads to unrealistic spacings or length it is necessary to modify the electrical characteristics and to try again. Since the whole procedure takes only a short time, a suitable compromise can be found quickly.

Appendix II. Corrections

An accurate small signal theory is given by Hutter [3]. More specific formulas [2, 4] have appeared in the literature from time to time, and the present method of design is based on the conventional assumptions of constant transit velocity and cylindrical field geometry in the flared part. Three corrections are, however, included in the final calculation which should be stated here.

(1) It is assumed that the field of the parallel section extends a distance $s/2$ beyond the plates.

(2) The electron with maximum deflection is assumed to travel along an equipotential line close to the positive deflection plate. Accordingly the field is inclined to the vertical by about the angle which the plate subtends with the axis. This means that the transverse acceleration results in a reduction of axial velocity. The term describing the transverse acceleration is corrected by the cosine of the plate angle, and the axial velocity through the drift space is corrected accordingly.

(3) It is also assumed that the axial motion is further retarded at the exit end while the transverse motion remains unchanged. Thus an electron just passing the edge of the positive plate has energy $e(V+V_{max}/2)$, but a short distance farther its energy is again eV and remains so to the screen. The corresponding field is axially directed since it usually terminates on grounded structures just ahead of the plates.

The axial velocity is reduced according'y.

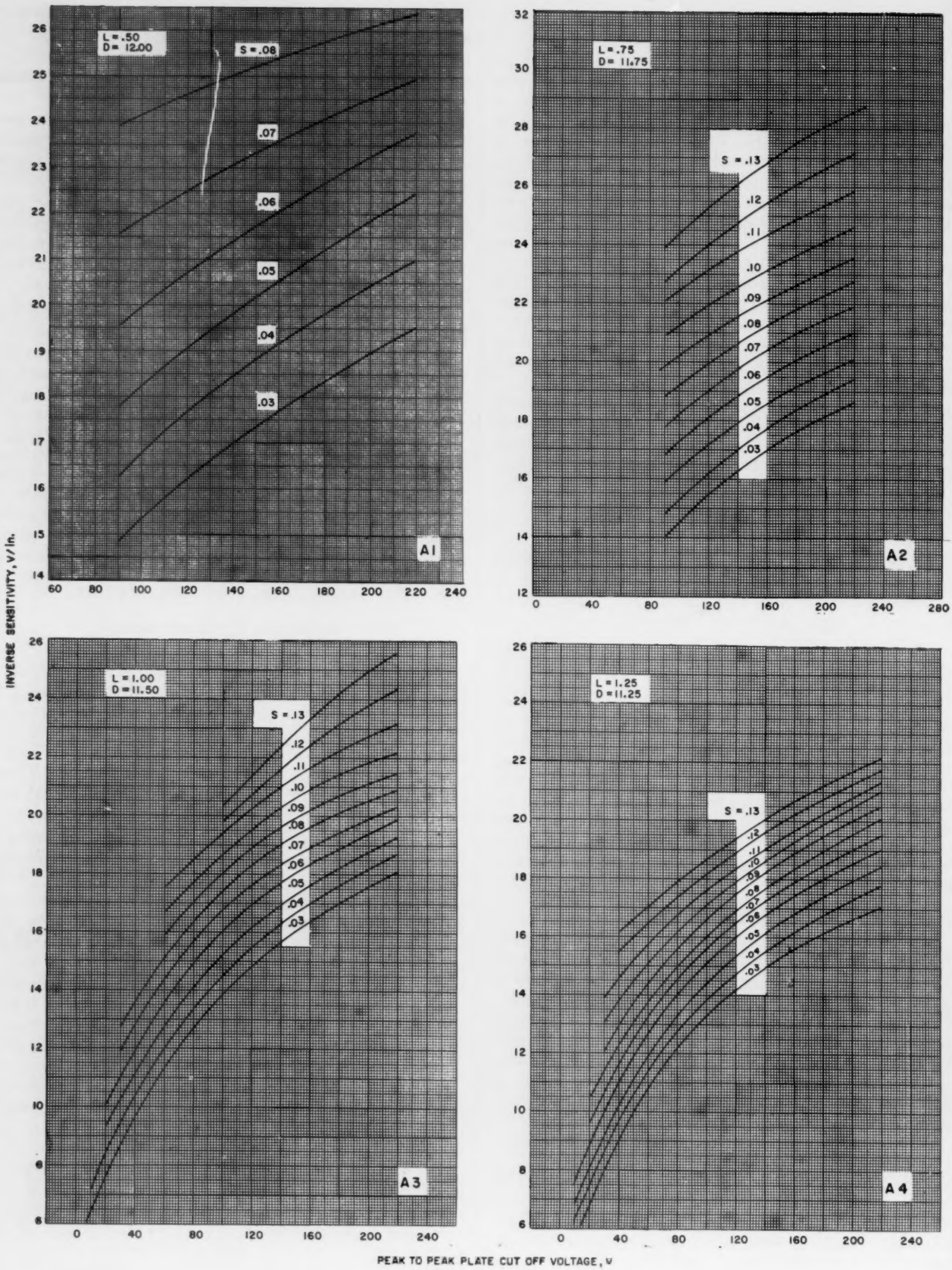
L = .50
D = 12.00
S = .08
.07
.06
.05
.04
.03
A1
L = .75
D = 11.75
S = .13
.12
.11
.10
.09
.08
.07
.06
.05
.04
.03
A2
L = 1.00
D = 11.50
S = .13
.12
.11
.10
.09
.08
.07
.06
.05
.04
.03
A3
L = 1.25
D = 11.25
S = .13
.12
.11
.10
.09
.08
.07
.06
.05
.04
.03
A4
INVERSE SENSITIVITY, v/in.
PEAK TO PEAK PLATE CUT OFF VOLTAGE, v

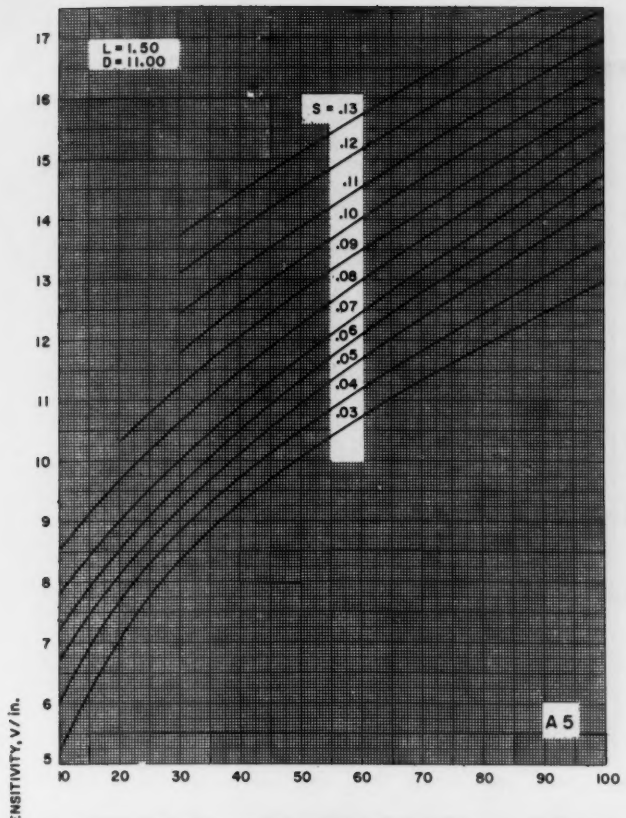
L = 1.50
D = 11.00
S = .13
.12
.11
.10
.09
.08
.07
.06
.05
.04
.03
A 5
INVERSE SENSITIVITY, V/in.

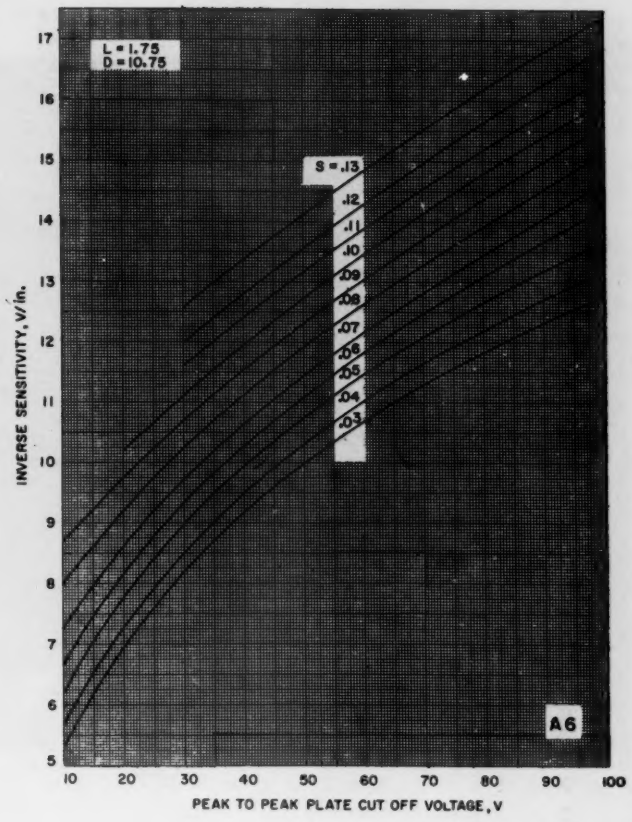
L = 1.75
D = 10.75
S = .13
.12
.11
.10
.09
.08
.07
.06
.05
.04
.03
A6
INVERSE SENSITIVITY, V/in.
PEAK TO PEAK PLATE CUT OFF VOLTAGE, V

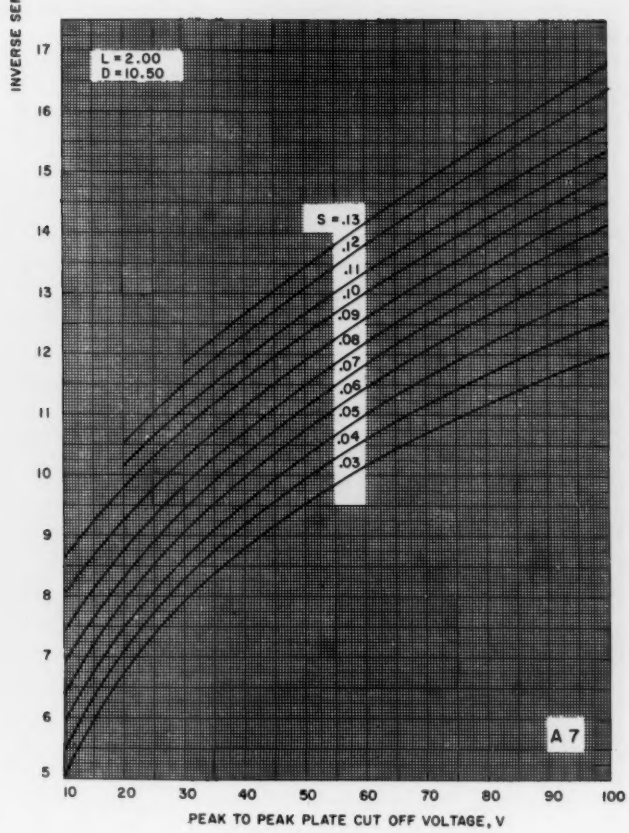
L = 2.00
D = 10.50
S = .13
.12
.11
.10
.09
.08
.07
.06
.05
.04
.03
A 7
INVERSE SENSITIVITY, V/in.
PEAK TO PEAK PLATE CUT OFF VOLTAGE, V

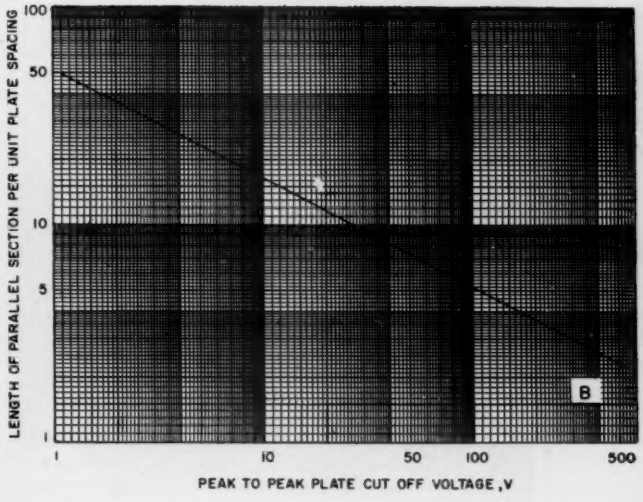
B
LENGTH OF PARALLEL SECTION PER UNIT PLATE SPACING
PEAK TO PEAK PLATE CUT OFF VOLTAGE, V

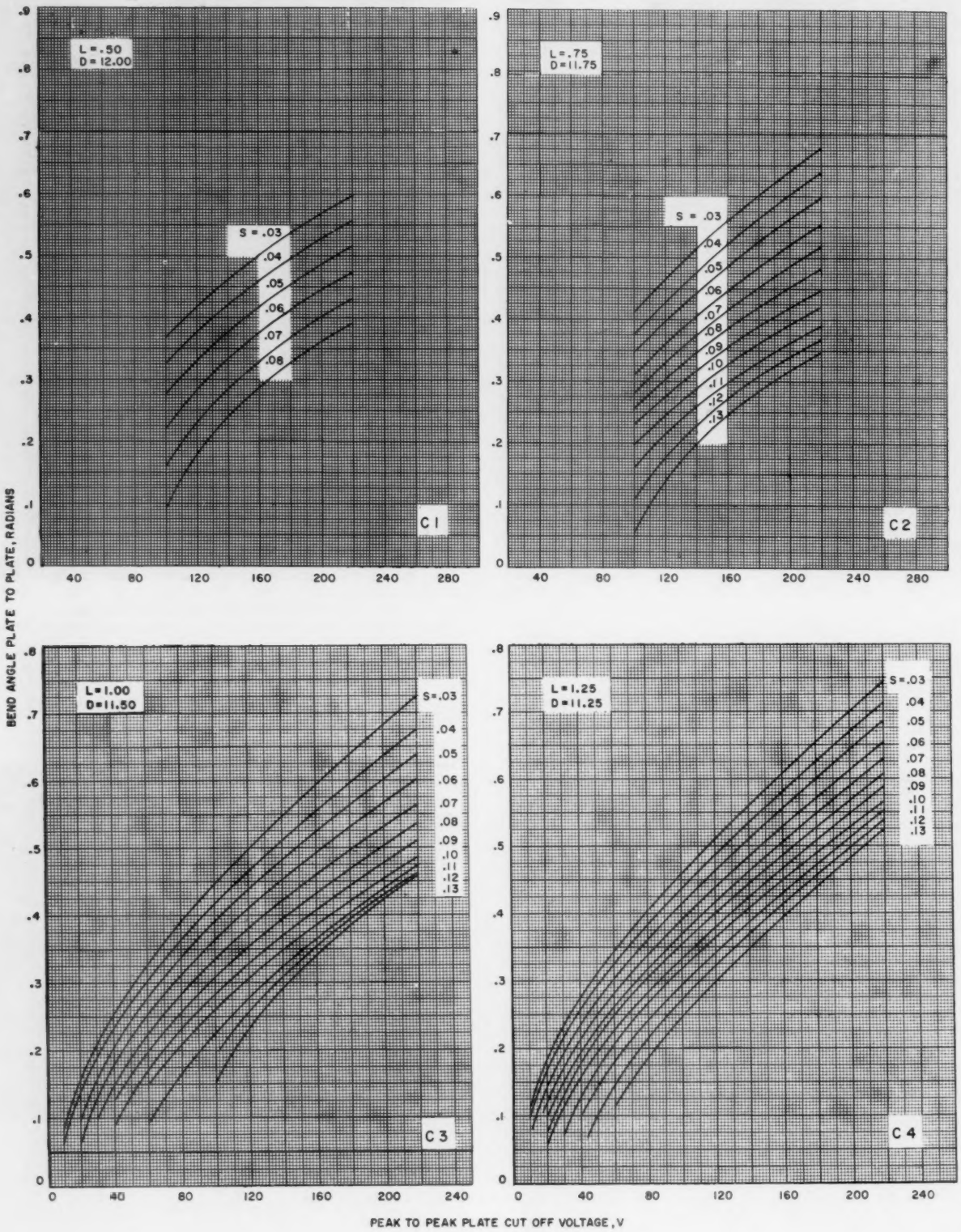
L=.50
D=12.00
S=.03
.04
.05
.06
.07
.08
C1
L=.75
D=11.75
S=.03
.04
.05
.06
.07
.08
.09
.10
.11
.12
.13
C2
L=1.00
D=11.50
S=.03
.04
.05
.06
.07
.08
.09
.10
.11
.12
.13
C3
L=1.25
D=11.25
S=.03
.04
.05
.06
.07
.08
.09
.10
.11
.12
.13
C4
BEND ANGLE PLATE TO PLATE, RADIANS
PEAK TO PEAK PLATE CUT OFF VOLTAGE, V

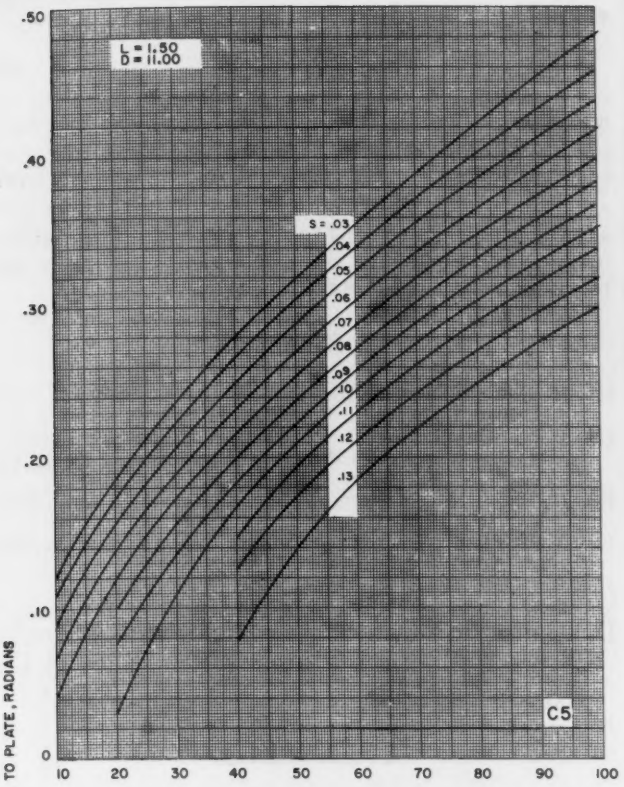
L = 1.50
D = 11.00
S = .03
.04
.05
.06
.07
.08
.09
.10
.11
.12
.13
C5
BEND ANGLE PLATE TO PLATE, RADIANS
0
.10
.20
.30
.40
.50
10
20
30
40
50
60
70
80
90
100

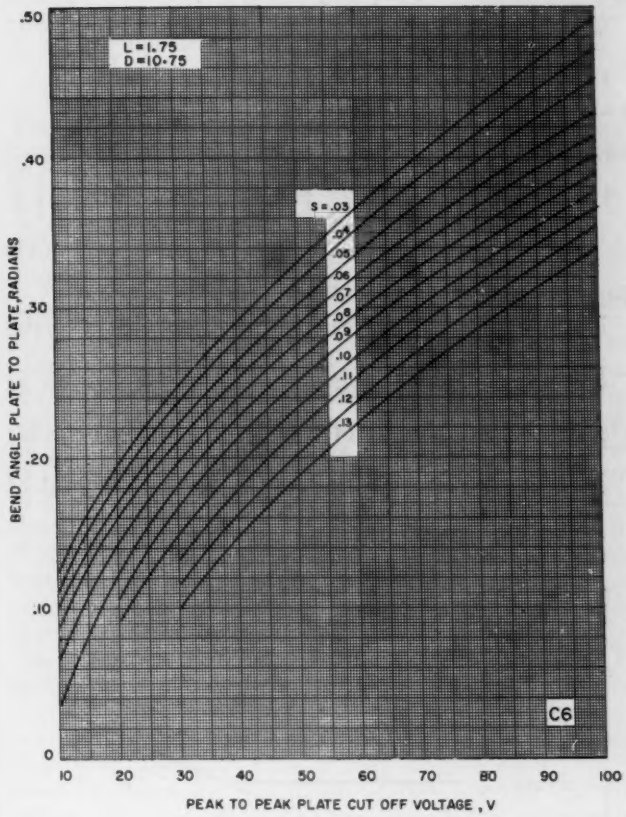
L = 1.75
D = 10.75
S = .03
.04
.05
.06
.07
.08
.09
.10
.11
.12
.13
C6
BEND ANGLE PLATE TO PLATE, RADIANS
0
.10
.20
.30
.40
.50
10
20
30
40
50
60
70
80
90
100
PEAK TO PEAK PLATE CUT OFF VOLTAGE , V

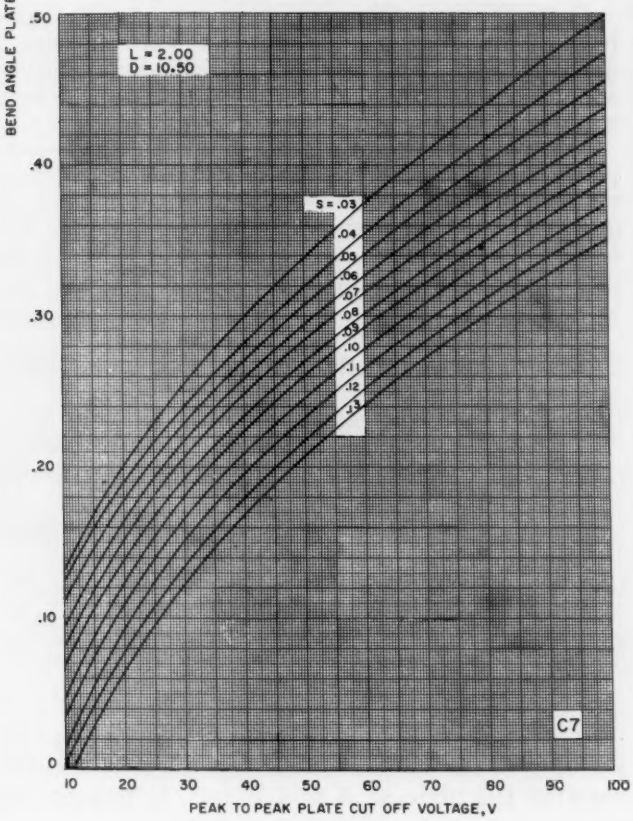
L = 2.00
D = 10.50
S = .03
.04
.05
.06
.07
.08
.09
.10
.11
.12
.13
C7
BEND ANGLE PLATE TO PLATE, RADIANS
0
.10
.20
.30
.40
.50
10
20
30
40
50
60
70
80
90
100
PEAK TO PEAK PLATE CUT OFF VOLTAGE, V

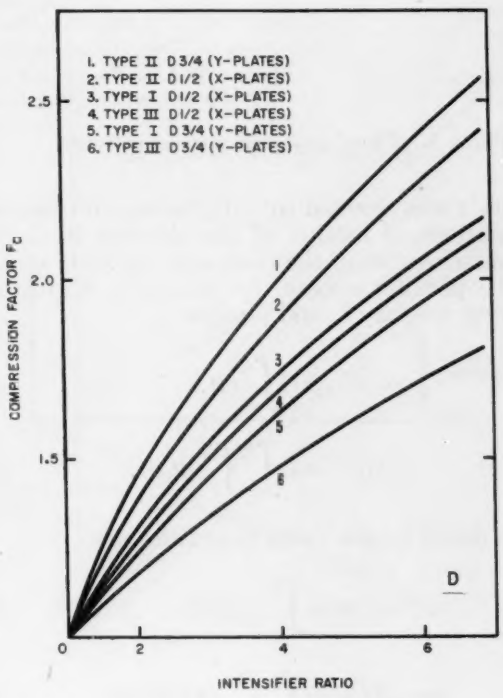
1. TYPE II D 3/4 (Y-PLATES)
2. TYPE II D 1/2 (X-PLATES)
3. TYPE I D 1/2 (X-PLATES)
4. TYPE III D 1/2 (X-PLATES)
5. TYPE I D 3/4 (Y-PLATES)
6. TYPE III D 3/4 (Y-PLATES)
1
2
3
4
5
6
D
COMPRESSION FACTOR F_C
0
1.5
2.0
2.5
0
2
4
6
INTENSIFIER RATIO

Appendix III. Theory

The general formula used for the design was:

$$y=\left(\frac{U}{VF_c}\right)\left[1+\frac{U}{4V}\left(1+\log\frac{b}{c}\right)\right]\left\{\frac{\bar{a}^2}{4s}+\frac{\bar{a}(b-c)}{2s}+D\left[\frac{a}{2s}+\frac{1}{2\alpha}\left(1-\frac{\alpha^2}{4}\right)\log\frac{b}{c}\right]+\frac{1}{2\alpha}\left[c-b\left(1-\log\frac{b}{c}\right)\right]\right\} \tag{a1}$$

where

$\bar{a}$ is the length of the straight section plus ½ of the spacing, s,
b is the terminal length of the flared section in polar coordinates,
c is the initial point of the flared section in polar coordinates,
D is the distance to the screen of the exit end of the plates,
$+V$ is the anode potential,
$V+U/2$, $V-U/2$ are the plate potentials,
y is the deflection at the screen,
F_c is the compression ratio,
s is the spacing of the plates, and
α is the plate angle.

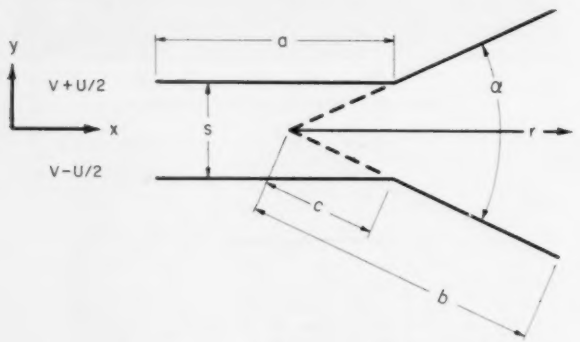

FIGURE 3. *Flared plate with parallel entrance.*

Formula 1 was derived by integrating and summing the equations of motion of the electron in the corresponding regions of the plate and the drift space.

In the parallel section, for example, we have for transverse velocity v_y and position y,

$$v_y=(eU/ms)\int_0^{t_x} dt, \tag{a2}$$

$$y=(eU/ms)\int_0^{t_{\bar{a}}}\int_0^{t_x} dt\,dt. \tag{a3}$$

For the flared region these quantities are

$$v_y=(eU/m\alpha)\int_{t_c}^{t_r}(1/r)dt, \tag{a4}$$

$$y=(eU/m\alpha)\int_{t_r}^{t_b}\int_{t_c}^{t_r}(1/r)dt\,dt. \tag{a5}$$

We also have, according to our assumption, the energy equation determining the axial velocity.

$$mv_x^2=2eV, \tag{a6}$$

and therefore,

$$dt=dx/\sqrt{2eV/m}, \tag{a7}$$

applying eq (a2) to (a5) to the corresponding regions, integrating by means of (a7) and applying the corrections outlined before there results eq (a1).

8. References

[1] H. Moss, The electron gun of the cathode ray tube, J. Brit. Inst. Radio Engrs. **6,** 99, (1946).
[2] I. G. Maloff and D. N. Eppstein, Electron optics in television, p. 100 (McGraw-Hill Book Co., Inc., New York, N. Y., 1938).
[3] R. G. E. Hutter, Electron beam deflection, J. Appl. Phys. **18,** 740, (1947).
[4] R. Benham, Inclined deflection plates, Wireless Eng. **13,** No. 148, p. 10 (1936).

II. Deflection Defocusing Distortion of Single-Bend Deflection Plates With Parallel Entrance Sections

1. Introduction

Cathode-ray oscilloscope displays generally suffer from a broadening of the trace with increasing deflection [1].[1] This is known as deflection distortion and has been treated in the literature in a general way [1, 2, 3].

Many standard cathode-ray tubes use single-bend plates with parallel entrance sections since these plates are both convenient and sensitive. A graphical design method for such plates has been described in section I. We now deal primarily with the calculation of the deflection distortion due to plates of this type.

2. Distortions Due to the Parallel Entrance Section

Let V be the mean potential in the plate region with respect to the cathode,
U be the deflection potential across the plates,
a be the length of the straight section,
s be the plate spacing,
e be the charge of the electron,
m be the mass of the electron,
F_1, F_x, F_y be field components,
v_1, v_x, v_y be velocity components,
E be a symbol for energy, and
w be the width of the beam.

Since electron energy at any point is given by the potential of the point in the field, we see that electrons entering the plate at A and B (fig. 1) respectively

[1] Figures in brackets indicate the literature references at the end of Section II.

have energies differing by

$$\Delta E = eUw/s. \tag{1}$$

Further, we see from figure 1 that this difference is nearly all due to the difference in horizontal velocity, since the vertical field components acting on the electrons entering the field are equal while the horizontal components are opposite.

We have during transit:

$$\text{field} = Fy = U/s \tag{2}$$

$$\text{force} = eU/s \tag{3}$$

$$\text{accel} = eU/ms \tag{4}$$

$$\text{time} = a/v_x \tag{5}$$

therefore,

$$vy = eaU/mSV_x, \tag{6}$$

whence the exit angle for small deflections is given by:

$$\theta \approx \tan\theta = eUa/msv_x^2 \tag{7}$$

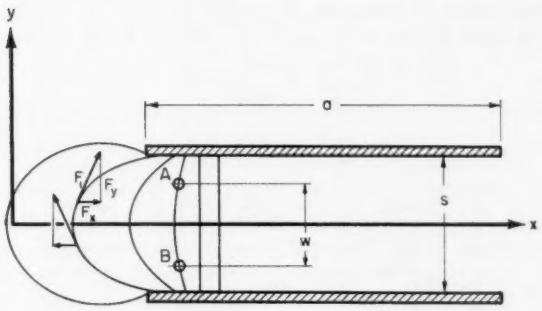

FIGURE 1. *The fringe field in the parallel section.*

But v_x differs for the two electrons, and to find the distortion we differentiate θ with respect to the entrance ordinate y.

We note that generally

$$E = mv^2/2 \tag{8}$$

and

$$\mathrm{E} = e(V + yU/s) \tag{9}$$

or, combining (8) and (9)

$$v^2 = 2e(V + yU/s)/m \tag{10}$$

and since, as we have seen, for purposes of energy computations v equals v_x, we get for θ

$$\theta = aU/2s(V + yU/s) \tag{11}$$

and by differentiation

$$\frac{d\theta}{dy} = -\frac{aU^2}{2s^2(V + U/s)^2}. \tag{12}$$

Using w for the separation dy of the two extreme electrons and substituting eq (11) in (12) we find:

$$\Delta\theta = -2w\theta^2/a. \tag{13}$$

Thus the distortion varies as the square of the deflection angle and linearly with beam width. We also note that it varies inversely as the plate length.

3. Flared Section

We will assume that the field in the flared section is cylindrically symmetrical.

One further assumption will be made which requires some discussion. We will again assume that the entire energy difference for the extreme electrons is due to the difference in v_x. This assumption may be justified as follows. The mean energy difference of the electrons at extreme ends of the cross section is of the order of U divided by the ratio of plate spacing at some arbitrary point to beam width. Since the deflecting field decreases as the spacing increases we may assume the effective ratio to be about 2 or 3 for plates in which the initial spacing is comparable to the beam width. For such plates the Y-directed velocity after transit through the plates corresponds to a kinetic energy of the order of U. Thus it follows that the energy differences across the beam are substantial fractions of the deflection energy. But it may be observed experimentally that the distortion is only a small fraction of the total deflection. Thus the energy differential involved in the vertical motion of the electrons in the cross section is negligible.

Let us express this analytically:

In figure 2, let

c = the radius at the entrance,
b = the radius at the exit,
α = the angle of flare, and
g = the final opening.

Then

$$mv_x^2/2 = e\alpha(V + yU/\alpha x - \epsilon). \tag{14}$$

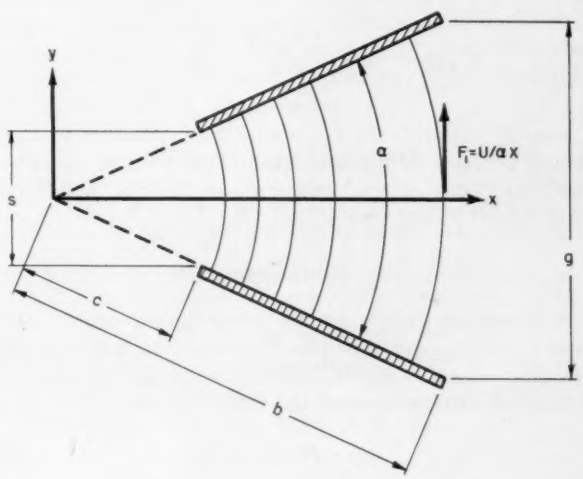

FIGURE 2. *The flared section.*

Here is a correction for the fact that some energy is contained in the vertical motion of the electron. Our assumption now states that ϵ may be larger than $yU/\alpha x$, but the differential of ϵ with respect to y is negligible compared to the differential of $(yU/\alpha x)$, at least in those parts of the field where deflection is effective. With these assumptions we proceed as before:

$$F_y=(U)/\alpha x) \text{ approx} \tag{15}$$

$$\text{(acceleration) } y=eU/m\alpha x. \tag{16}$$

But since the acceleration now depends on x we have to integrate to find v_y:

$$v_y=eU/m\alpha\int_{t_c}^{t_b}(1/x)\,dt \tag{17}$$

and since $dt=dx/v_x$ (18)

$$v_y=eU/m\alpha\int_c^b 1/(v_x x)dx. \tag{19}$$

For small angles we may sum the increment:

$$\theta=(eU/m\alpha)\int_c^b 1/(v_x^2 x)dx. \tag{20}$$

Substituting for v_x^2 from (14) we have

$$\theta=\frac{U}{2\alpha}\int_c^b\frac{dx}{x(V+yU/\alpha x-\epsilon)}. \tag{21}$$

To find the defocusing effect we differentiate (21) with respect to y, remembering that $d\epsilon/dy=0$; hence,

$$\frac{\partial\theta}{\partial y}=\frac{U}{2\alpha}\int_c^b\frac{Udx}{(V+yU/\alpha x-\epsilon)^2\alpha x^2}. \tag{22}$$

We may now integrate (21) and (22), disregarding small quantities, to get

$$\theta=(U/2\alpha V)\log(b/c), \tag{23}$$

and

$$\Delta\theta=-dy\frac{U^2}{2\alpha^2V^2}\left(\frac{b-c}{bc}\right). \tag{24}$$

Thus, $d\theta$ depends on U^2, and θ on U; hence in the inclined section $d\theta$ again depends on θ^2 and on $w=dy$, but its dependence on plate shape is now complicated as it involves log (b/c).

4. Total Distortion

A formula may now be established which allows direct investigation of the distortion of various plates designs. Let D be the distance to the screen; then the total broadening of the line will be

$$\Delta y=D(d\theta_1+d\theta_2) \tag{25}$$

where $d\theta_1$, $d\theta_2$ are the distortions of the straight and flared sections, respectively. Substituting in (25) from (12) and (24) we get, after some rearranging:

$$\Delta y=-\frac{wDU^2a}{2s^2V^2}\left[1+s\frac{(g-s)}{\alpha ga}\right]. \tag{26}$$

Here c and b have been eliminated by

$$\alpha c=s, \tag{27}$$

and

$$\alpha b=g, \tag{27a}$$

respectively. For practical designs (26) may be further simplified since g is much larger than s, i.e.,

$$\Delta y=-\frac{wDU^2a}{2V^2s}\left(1+\frac{s}{\alpha a}\right). \tag{28}$$

Equation (28) is useful in comparing the distortions of various possible designs. Thus, when using the plate designs described in section I of this paper, the parameters in eq (28) may be found from the electrical characteristics required of the plate, and it is possible to take distortions into consideration when discussing a particular design. An example of the application of formula 28 to three experimental plates for a tube is given in table 1. Plate C is about twice as long as the other plates and may be seen to have only about one-fourth as much distortion. For a given plate length, increased sensitivity gives slightly better distortion characteristics, but generally distortions are determined by the desired characteristics of the plate.

TABLE 1

A	B	C
W= 030 in.	W= 030 in.	W=030 in.
D= 10.50 in.	D= 12.25 in.	D= 11.25 in.
U= 150 v (full scan)	U= 125 v (full scan)	U= 85 v (full scan)
a= .220 in.	a= .210 in.	a= .300 in.
s= .060 in.	s= .050 in.	s= .060 in.
V=1675 v	V=1675 v	V=1675 v
α= .600 rad	α= .535 rad	α= .500 rad
$\frac{s}{\alpha a}$= .450	$\frac{s}{\alpha a}$= .445	$\frac{s}{\alpha a}$= .400
Δy= .128	Δy= .124 in.	Δy= .036 in.

5. Post Accelerator Field

Post acceleration generally reduces a scan pattern by the so-called compression factor shown in figure D of the plate design curves (see 5, section I). Since distortions are essentially a scan pattern they, too, are reduced by post acceleration, and eq (28) must be modified accordingly:

$$\Delta y=-\frac{wDU^2a}{2F_c s^2V^2}\left(1+\frac{s}{\alpha a}\right). \tag{29}$$

In evaluating the distortions of monoaccelerators versus post accelerators it must be remembered that the deflection voltage requirements in the latter in-

crease by the factor F_c. In eq (29) therefore, at equal deflection, Δy would be increased by a factor of F_c since for a given plate and for a fixed deflection, U would have to be increased as post acceleration is applied.

6. Agreement With Experiment

Maloff and Eppstein [1] have stated that distortions due to deflection in well-designed tubes are several times less severe than those to be expected from elementary theory. It is interesting therefore to see how eqs (28) or (29) compare with experiment. A typical experiment is shown in figure 3. The

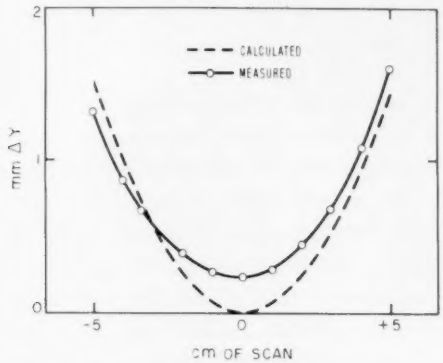

FIGURE 3. *Deflection defocusing.*

plate here is similar to plate A of table 1 but a compression factor of $F_c=2$ applies. The agreement between calculated and experimental values are seen to be good in this instance. When making observations of deflection defocusing some points have to be carefully considered. Most modern plates are marginal, i.e., they intercept some of the beam toward the edge of the scan, and therefore the spot there tends to be less distorted than it would be theoretically. Another point of experimental significance is the mode of focusing. Consider for instance figure 4 in which 2 positions are shown for the screen.

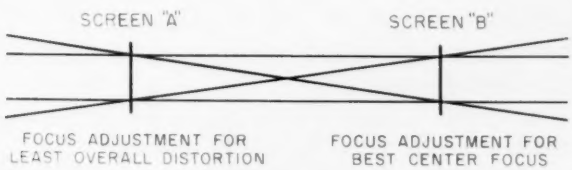

FIGURE 4. *Two possible focus adjustments relative to screen position.*

Position *a* shows an "underfocused" beam while position *b* corresponds to an overfocused beam. It is clear that deflection distortion, which consists of a focusing action with deflection, will be more effective in position *b* than in position *a*. The conclusion is that defocusing depends on the adjustment of the focusing lens and on the nature of beam formation about which not much is known.

7. Corrections for Defocusing

Qualitative reasoning suggests that no effective correction can be found which does not simultaneously result in severe deflection linearity distortion. This may be seen as follows: Since Δy is a negative function of y, deflection results in overfocusing. Nothing can be done about this in a nearly parallel section which is present in any deflection plate, for in such a region the assumptions made here are rigidly true.

At the exit end of the plates however, where the beam is already deflected across the axis, our assumptions do not hold, and the field may be shaped in such a manner as to deflect the electron traveling closer to the positive plate more than the electron at the other end of the cross section. If this is done it is clear that the correction is applied in a region of rapidly increasing separation of the entire beam from the axis. Thus what is required here is a variation of the effective strength of the deflection field in a transverse direction which is effective over the cross section of the beam. Consider now the effect of such a field on the central electron in a beam. As the deflection is increased the central electron travels in regions of increasingly effective deflection fields, and consequently the overall deflection becomes nonlinear.

The foregoing conclusion is particularly true of arrangements employing corrective static lenses such as positive wires lined up parallel to the exit edge of the plates.

In contrast with the qualitative argument given above, detailed mathematical treatment has led other authors [3, 4, 5], to propose plate shapes for which various degrees of correction are claimed.

8. Conclusions

Deflection defocusing in single-bend plates with parallel entrance sections is approximately proportional to the square of the deflection, it is linearly dependent on beam width, and is roughly inversely proportional to plate length and is therefore susceptible to changes in plate design.

9. References

[1] I. G. Maloff and D. W. Eppstein, Electron optics in television, p. 203 (McGraw-Hill Book Co., Inc., New York, N.Y., 1938).

[2] J. R. Pierce, Theory and design of electron beams, p. 43 (D. Van Nostrand Co., Inc., New York, N.Y., 1954).

[3] J. E. Rosenthal, Correction of deflection defocusing in CRT's, Proc. I.R.E. **39,** 10 (1951).

[4] R. G. E. Hutter, Electron beam deflection J. Appl. Phys. **18,** 797 (1947).

[5] R. G. E. Hutter, Advances in electronics, Vol. I, p. 167 (Academic Press, New York, N.Y., 1949).

WASHINGTON, D.C. (Paper 64C2–30)

JOURNAL OF RESEARCH of the National Bureau of Standards—C. Engineering and Instrumentation
Vol. 64C, No. 2, April–June 1960

The Functional Synthesis of Linear Plots[1]

J. P. Vinti and R. F. Dressler[2]

(January 26, 1960)

In practical engineering or experimental work one often encounters a function F of many variables, F (x's, y's, z's), represented only by the families of curves obtained by plotting F against each of the x's on Cartesian graph paper, against each of the y's on semi-log paper, and against each of the z's on double-log paper. It frequently happens that these curves are all approximately straight lines over a limited range of interest. On the assumption that they are all true straight lines, the present note shows how to synthesize all the graphical representations, for any number of parameters, into the most general formula possible, expressing F as the product of a multilinear function of the x's and the exponential of a constant-free multilinear function of the y's and of the log z's, the coefficients in both multilinear functions being independent of the x's, y's, and z's.

1. Introduction

In an investigation by one of the authors on assemblages of elastic shells, the various results for certain components of stress and displacement exhibited approximately linear behavior over the limited ranges of interest of the relevant parameters, when plotted on Cartesian graph paper, semi-log paper, or double-log paper. These results, derived from various numerical calculations and corroboratory experiments, are functions of many parameters, such as the various geometrical ratios defining shell shapes, the shell thickness, Poisson's ratio, the number of coupled shells, and other significant quantities. Rather than to retain these extensive results in the form of cumbersome families of graphs, it was desirable and useful to combine them in such a way as to obtain a single explicit formula for each dependent quantity, in terms of the above-mentioned independent parameters.

The problem of combining such results is, of course, not peculiar to investigations in elasticity but often arises in experimental or engineering work of any nature. One can very easily construct simple functions which will exhibit some of these "linear" properties, but the most general answer to the inverse problem is less obvious, especially when the number of parameters is large. Then an unsystematic attempt to effect such a synthesis may prove infeasible or incomplete, and furnish no assurance that one has indeed constructed the most general function with these properties. Our present note, therefore, formulates the general problem for any number of variables in a precise manner and derives its *most general* solution. For the simple case of only three parameters, the solution is illustrated by a few examples.

2. The General Problem

In the following developments we shall assume that all the pertinent quantities have been grouped into independent dimensionless combinations, so as to take advantage of whatever information is provided by the Buckingham Pi theorem.[3] Let us then consider a dimensionless function F of the dimensionless independent variables $x_1, x_2, \ldots, x_m; y_1, y_2, \ldots, y_p; z_1, z_2, \ldots, z_q;$ and $u_1, u_2, \ldots, u_r$, such that a straight line results when we plot F against any x on ordinary Cartesian graph paper, against any y on semi-log paper, or against any z on double-log paper. Let the u's denote all other dimensionless variables on which F may depend, but for which no such "linear" property exists. It is understood, of course, that in practice such linearity may hold only approximately, and only for a certain bounded range of the variable used as abscissa, and only for certain bounded ranges of the remaining variables, which appear as parameters. With no loss of generality, however, we relax these restrictions, assuming that each plot is a straight line for all values of abscissa and parameters.

[1] This research was supported by the United States Air Force, through the Office of Scientific Research of the Research and Development Command.

[2] On leave to Institute of Mathematical Sciences, New York University, New York, N.Y.

[3] P. W. Bridgman, Dimensional analysis, p. 36 (Yale Univ. Press, New Haven, Conn., 1931).

We put

$$\ln z_1 = y_{p+1}, \quad \ln z_2 = y_{p+2}, \quad \ldots, \quad \ln z_q = y_n, \qquad (n = p+q); \tag{1}$$

then $F(x_1, \ldots x_m, y_1, \ldots y_n, u)$ is a function such that the plot of F against any x or of $\ln F$ against any y is a straight line on Cartesian graph paper. Here u denotes the set $u_1, u_2, \ldots, u_r$. Then

$$\ln F = A_k y_k + B_k \qquad (k = 1, 2, \ldots, n) \tag{2}$$

where A_k and B_k are functions of $x_1 \ldots x_m$, $y_1 \ldots y_{k-1}$, $y_{k+1} \ldots y_n$, and of the u's. We then ask: if $\ln F$ is linear in each y when the other y's are all held constant, what is the most general form for $\ln F$, as a function of the y's, that will represent such a property?

To answer this preliminary question, we first recall the definition of a *multilinear* function G, of several variables $t_1, t_2, \ldots, t_s$, as a function which is the sum of a constant and a linear combination of all the products of the t's taken one at a time, two at a time, $\ldots$, s at a time, without repetition. For example, if $s=3$,

$$G(t_1,t_2,t_3) = a_0 + a_1t_1 + a_2t_2 + a_3t_3 + b_1t_2t_3 + b_2t_3t_1 + b_3t_1t_2 + ct_1t_2t_3. \tag{3}$$

Any such multilinear function satisfies the differential equations

$$\partial^2 G / \partial t_k^2 = 0 \qquad (k = 1,2, \ldots, s). \tag{4}$$

(When the constant term vanishes, we term G a constant-free multilinear function.) It is then easily shown by induction that $G(t_1,t_2, \ldots, t_s)$ is the most general function of $t_1,t_2, \ldots, t_s$ which is linear in each t.

2.1. The Synthesis for the y's Alone

On applying these considerations to (2), we find that

$$\ln F = g(x_1,x_2, \ldots, x_m, u) + N^{(x,u)}(y_1,y_2, \ldots, y_n), \tag{5}$$

where $N^{(x,u)}$ denotes a general constant-free multilinear function of the y's, with coefficients which are, a priori, functions of $x_1, \ldots, x_m, u$. On placing

$$\exp g = f(x_1,x_2, \ldots, x_m,u), \tag{6}$$

we obtain

$$F = f(x_1,x_2, \ldots, x_m,u) \exp N^{(x,u)}, \tag{7}$$

which gives the synthesis of the linearities of $\ln F$ versus the y's.

2.2. The Complete Synthesis

Since F is linear in each x, it follows from the property of multilinear functions that

$$F = P^{(y,u)}(x_1,x_2, \ldots, x_m), \tag{8}$$

where $P^{(y,u)}$ is a general multilinear function of the x's, the coefficients being functions of the y's and the u's. Then

$$F = f(x_1,x_2, \ldots, x_m,u) \exp N^{(x,u)} = P^{(y,u)}(x_1,x_2, \ldots, x_m), \tag{9}$$

where by (4)

$$\partial^2 N / \partial y_k^2 = 0 \qquad (k = 1,2, \ldots, n) \tag{10}$$

$$\partial^2 P / \partial x_j^2 = 0 \qquad (j = 1,2, \ldots, m). \tag{11}$$

We next show that f is a multilinear function of the x's. To do so, put every y equal to zero in (9). Since N contains no constant term, it then vanishes, so that (9) becomes

$$f(x_1, x_2, \ldots, x_m, u) = M^{(u)}(x_1, x_2, \ldots, x_m). \tag{12}$$

Here $M^{(u)}$ is simply the expression for $P^{(y,u)}$ with each coefficient evaluated at each $y=0$, so that it is a multilinear function of the x's with coefficients depending only upon the u's.

We now show that the coefficients in $N^{(x,u)}$ are independent of the x's, as follows. Insert (12) into (7), so that

$$F = M^{(u)} \exp N^{(x,u)} \tag{13}$$

and require that (13) satisfy (11). It follows that

$$\frac{\partial^2 M}{\partial x_j^2} + M\frac{\partial^2 N}{\partial x_j^2} + 2\frac{\partial M}{\partial x_j}\frac{\partial N}{\partial x_j} + M\left(\frac{\partial N}{\partial x_j}\right)^2 = 0 \tag{14}$$

where we have omitted the superscripts for convenience. Since M is multilinear in the x's, it follows from (4) that

$$\partial^2 M/\partial x_j^2 = 0, \tag{15}$$

so that

$$M\frac{\partial^2 N}{\partial x_j^2} + 2\frac{\partial M}{\partial x_j}\frac{\partial N}{\partial x_j} + M\left(\frac{\partial N}{\partial x_j}\right)^2 = 0. \tag{16}$$

If we now differentiate (16) twice with respect to y_k, we find with use of (10) that

$$2M\left(\frac{\partial^2 N}{\partial x_j \partial y_k}\right)^2 = 0, \tag{17}$$

whence

$$\frac{\partial}{\partial y_k}\left(\frac{\partial N}{\partial x_j}\right) = 0 \quad \begin{cases} j = 1,2, \ldots, m, \\ k = 1,2, \ldots, n. \end{cases} \tag{18}$$

Equation (18) means that $\partial N/\partial x_j$ can be a function only of the x's and the u's. But N and $\partial N/\partial x_j$ are constant-free multilinear functions of the y's, with coefficients that are, a priori, functions of the x's and the u's. These results are compatible if and only if

$$\partial N/\partial x_j = 0 \qquad (j = 1,2, \ldots, m) \tag{19}$$

so that each coefficient in the constant-free multilinear function N must be independent of the x's.

We may thus rewrite (13) as

$$F = M^{(u)}(x_1, x_2, \ldots, x_m) \exp \mathrm{N}^{(u)}(y_1, y_2, \ldots, y_n). \tag{20}$$

When we return to the original formulation of the problem in terms of the x's, y's, and z's, it follows that the *most general* functional form for F is given by

$$F = M^{(u)}(x_1, x_2, \ldots, x_m) \exp \mathrm{N}^{(u)}(y_1, y_2, \ldots, y_p, \ln z_1, \ln z_2, \ldots, \ln z_q), \tag{21}$$

where $M^{(u)}$ is a general multilinear function of the x's and $N^{(u)}$ a general constant-free multilinear function of the y's and $\ln z$'s, the coefficients in both being functions only of the u's.

3. Some Elementary Examples

As short illustrations of the general result (21), we append a few cases where F has linear plots against only three variables. For each we list the specific form that (21) assumes and the slopes and intercepts on the appropriate plots. By comparing the behavior of the slopes

and intercepts in the various experimentally given families of curves that define the function F with these listed formulas, one can readily determine which coefficients vanish, if any, and thus obtain a specific formula for F in any actual case. Here "ln" denotes a natural logarithm and "log" a common logarithm. For an x or a y the intercept is taken at zero, while for a z it is taken at $z=1$. For the logarithmic plots the slopes and intercepts are those of $\log F$. In the following formulas, it is understood that the constants may be functions of the u's.

(a) **x, y_1, y_2**

$$F=(k_1x+k_2)\exp(a_1y_1+a_2y_2+by_1y_2)$$

Cartesian plot versus x:

slope $S=k_1\exp(a_1y_1+a_2y_2+by_1y_2)$

intercept $I=k_2\exp(a_1y_1+a_2y_2+by_1y_2)$

Semi-log plot versus y_1:

slope $S=0.4343(a_1+by_2)$

intercept $I=\log(k_1x+k_2)+0.4343a_2y_2$

(b) **x, y, z**

$$F=(k_1x+k_2)e^{a_1y}z^{a_2+by}$$

Cartesian plot versus x:

slope $S=k_1e^{a_1y}z^{a_2+by}$

intercept $I=k_2e^{a_1y}z^{a_2+by}$

Semi-log plot versus y:

slope $S=0.4343a_1+b\log z$

intercept $I=\log(k_1x+k_2)+a_2\log z$

Double-log plot versus z:

slope $S=a_2+by$

intercept $I=\log(k_1x+k_2)+0.4343a_1y$

(c) **y_1, y_2, z**

$$F=ke^{a_1y_1+a_2y_2+b_3y_1y_2}z^{a_3+b_1y_1+b_2y_2+cy_1y_2}$$

Semi-log plot versus y_1:

slope $S=0.4343(a_1+b_3y_2)+(b_1+cy_2)\log z$

intercept $I=\log k+0.4343a_2y_2+(a_3+b_2y_2)\log z$

Double-log plot versus z:

slope $S=a_3+b_1y_1+b_2y_2+cy_1y_2$

intercept $I=\log k+0.4343(a_1y_1+a_2y_2+b_3y_1y_2)$

(d) **y, z_1, z_2**

$$F=ke^{a_1y}z_1^{a_2+b_1y}z_2^{a_3+b_2y}H$$

where

$$H = z_1^{(b_3+cy)\ln z_2} = z_2^{(b_3+cy)\ln z_1}$$

Semi-log plot versus y:

slope $\quad S = 0.4343a_1 + b_1 \log z_1 + b_2 \log z_2 + 2.303c \log z_1 \log z_2$

intercept $\quad I = \log k + a_2 \log z_1 + a_3 \log z_2 + 2.303b_3 \log z_1 \log z_2$

Double-log plot versus z_1:

slope $\quad S = a_2 + b_1 y + 2.303(b_3 + cy) \log z_2$

intercept $\quad I = \log k + 0.4343a_1 y + (a_3 + b_2 y) \log z_2$

WASHINGTON, D.C. (Paper 64C2–31)

JOURNAL OF RESEARCH of the National Bureau of Standards—C. Engineering and Instrumentation
Vol. 64C, No. 2, April–June 1960

Radiation Field From a Rectangular Source[1]

J. H. Hubbell, R. L. Bach, and J. C. Lamkin

(January 12, 1960)

Many radiation shielding problems involve calculations of the response of an isotropic detector to radiation of arbitrary angular distribution from uniform rectangular sources. In calculations of this type the family of integrals $\int_S(\cos\theta dS/r^2)P_l(\cos\theta)$ and the integral $\int_S(dS/r^2)\exp(-\mu t/\cos\theta)$ are frequently encountered, where θ is obliquity with respect to an axis perpendicular to the plane containing the rectangular radiant surface, S, r is the distance from an element of source area, dS, to the detector, μ is the attenuation coefficient, and t is the barrier thickness. Solutions of the first type of integral facilitate use of Legendre expansion representations of radiation directional distributions, and may also have application in other radiant surface studies, such as illumination and heat exchange engineering. The second integral relates to exponentially attenuated radiation from a plane isotropic rectangular source separated from the detector by a layer of material of thickness t. Formulas, expansions, and numerical results are presented.

1. Introduction

The penetration of radiation into structures has been the subject of theoretical [1,2] [2] and experimental [3] investigations as part of a general program at the National Bureau of Standards and other agencies. The theoretical investigations are usually performed in two stages: (a) *penetration* and (b) *geometry*. The penetration stage refers to generation of data relating to interaction of the radiation with barrier materials [4], and geometry refers here to the application of such data to specific configurations of source, barrier, and detector. This paper treats the geometrical stage of problems involving rectangular sources, e.g., ceilings of buildings or shelters. We draw to some extent from similar treatments in illumination [5 to 8] and heat-exchange [9] engineering. The methods developed in this paper, in turn, have application to rectangular sources of light and heat as well as gamma radiation.

In the geometrical stage of many shielding problems, the following situation, generalized in figure 1, arises: one has a radiation detector and a surface S through which radiation emerges. In the schematization of reference [1], the flow of radiation through each element of surface, dS, is independent of position on the surface, and no scattering of radiation occurs after emergence from surface S. The intensity and angular distribution, $g(\cos\theta)$, of radiation crossing the plane S is assumed known from the penetration stage of the analysis. The quantity $g(\cos\theta)$, usually called the *flux* [4], is the radiation intensity per solid angle (e.g., photons per cm^2 per second per steradian) traveling in the direction θ with respect to the z-axis (see fig. 1). If the detector has an isotropic response it will register a value I_s proportional to an integral of $g(\cos\theta)$ over the total solid angle, Ω_S, subtended by the surface S from the detector:

$$I_S = \int_S d\Omega_S(\theta)\ g(\cos\theta). \tag{1}$$

where

$$d\Omega_S(\theta) = dS \cdot \cos\theta / r^2$$

and r is the distance from surface element dS to the detector.

Introducing the quantity $\psi_S(\theta)$, which is the total range of azimuthal angle, φ, defined by the intersection of a θ-cone with the surface S, as in figure 1, we may write (1) in polar coordinates as

---

[1] Work supported jointly by the Office of Civil and Defense Mobilization, the Navy Bureau of Yards and Docks, and the Defense Atomic Support Agency.

[2] Figures in brackets indicate the literature references at the end of this paper.

$$I_S=\int_{-1}^{1} d(\cos\theta)g(\cos\theta)\int_0^{\psi_S(\theta)} d\varphi \tag{2a}$$

$$=\int_{-1}^{1} d(\cos\theta)g(\cos\theta)\psi_S(\theta). \tag{2b}$$

As in the example in figure 1, $\psi_S(\theta)$ may consist of more than one "piece" of azimuth, $\Delta_i\varphi_S(\theta)$, so that in the general case it is a summation over all such pieces:

$$\psi_S(\theta)=\Delta_1\varphi_S(\theta)+\Delta_2\varphi_S(\theta)+\ldots. \tag{3}$$

This quantity is identical with the "angular response function," $\psi(\theta)$, of reference [1] except for a factor 2π.[3]

The surface S may now be specified as a rectangle, as shown in figure 2, with corners at x and y coordinates $(0, 0)$, $(w, 0)$, (w, l), and $(0, l)$. The detector is on the z-axis, hereafter referred to as the "corner position," at $z=h$. Since the solid angle integration indicated in eq (1) is dependent on relative rather than absolute distances we may reduce the number of parameters by dividing all dimensions and coordinates by h, i.e.,

$$a=w/h, \quad b=l/h, \quad \alpha=x/h, \quad \text{and } \beta=y/h.$$

This representation of the relative geometry, rather than representation by horizontal and vertical "eccentricities" as in references [1] and [2], is used here in order that the interchangeability of length and width might be used as a partial check of the results.

Figure 3 shows the use of these scaled coordinates in describing a typical rectangular source problem. Radioactive material is uniformly distributed over the roof slab of an underground shelter, and the problem is to calculate the detector response to radiation transmitted by the rectangular ceiling, or rectangular portions of the ceiling, into the enclosure below.

---

[3] Berger and Lamkin [1] included in $\psi(\theta)$ a normalizing factor $1/2\pi$, here omitted. Thus the quantity $\psi_S(\theta)$ defined in (3), above, is equivalent to their azimuthal range parameter A_θ.

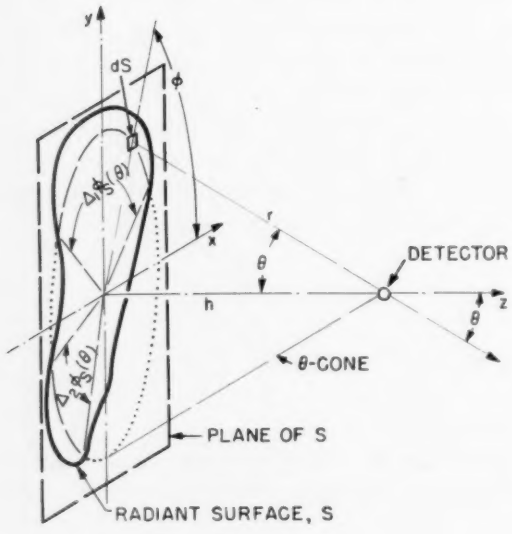

GURE 1. *Geometrical schematization of a detector at distance h from a plane source S of arbitrary shape.*

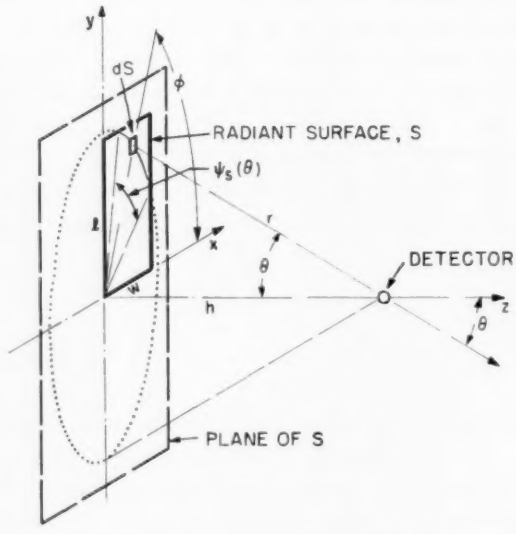

FIGURE 2. *Schematization when S is a rectangle of width w and length l with the detector in a "corner position" at distance h from the plane of S.*

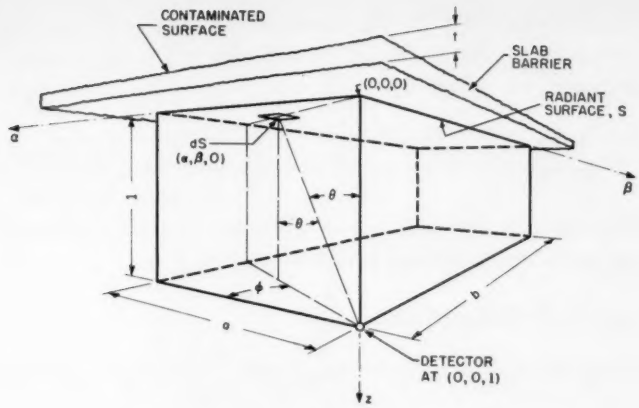

FIGURE 3. *Underground shelter situation in which the coordinates and dimensions in figure 2 are divided by h, i.e., $\alpha=x/h$, $\beta=y/h$, $a=w/h$ and $b=l/h$.*

There are several ways to evaluate the integral (1) for a rectangle, either in polar form (2 a,b) or using the cartesian parameters α, β. Berger and Lamkin [1] performed the integrations numerically, using the polar form, for a few representative angular distributions $g(\cos\theta)$ and a variety of rectangular shapes. Spencer [2] has approximated the function $\psi_S(\theta)$, which may now be written for a rectangle as $\psi(\theta,a,b)$, by step functions so as to reduce (2b) to a combination of values of the cumulative integral $\int_x^1 d(\cos\theta)\, g(\cos\theta)$.

In this paper, advantage is taken of the fact that $g(\cos\theta)$ may usually be represented as a sum of Legendre polynomials, i.e.,

$$g(\cos\theta)=\sum_{l=0}^{\infty}\left(l+\frac{1}{2}\right)g_l P_l(\cos\theta), \tag{4}$$

where

$$g_l=\int_{-1}^{1} d(\cos\theta)\, g(\cos\theta)\, P_l(\cos\theta). \tag{5}$$

Thus the integral (2b) may be expressed as a sum of elementary integrals

$$I(a,b)=\sum_{l=0}^{\infty}\left(l+\frac{1}{2}\right)g_l p_l(a,b), \tag{6}$$

where the $p_l(a,b)$'s are coefficients of the expansion

$$\psi(\theta,a,b)=\sum_{l=0}^{\infty}\left(l+\frac{1}{2}\right)p_l(a,b)\,P_l(\cos\theta). \tag{7}$$

The $p_l(a,b)$'s, which are *purely geometrical* and independent of the penetration stage of the problem (i.e., source energy, barrier thickness and material, etc.), may be evaluated as

$$p_l(a,b)=\int_S d\Omega_S(\theta)P_l(\cos\theta) \tag{8}$$

in which a and b completely specify the surface S. Evaluation of the $p_l(a,b)$'s will be outlined in section 4.1.

The sum (6) converges rapidly if *either* the g_l or the p_l converge rapidly. Since the g_l's are provided more readily from transport theory [4] than $g(\cos\theta)$, it is desirable to use (6) wherever applicable.

In the case of penetrating radiations, as from fallout, convergence of (6) may be inadequate as a result of the presence of the unscattered radiation component, which has an angular distribution of the form

$$g^0(\tau,\cos\theta)=\frac{\sigma}{4\pi}\exp\,(-\tau/\cos\theta)/\cos\theta. \tag{9}$$

The superscript ^{o} refers to unscattered radiation, τ is the slab thickness, μt, in mean-free-paths, and σ is the surface density of radioactive material. Since the $g_l^o(\tau)$'s evaluated from (5) and (9) converge too poorly for use in the expansion (6) when $0 \leq \tau \lesssim 1$, an alternative expansion

$$I^o(\tau,a,b)=\frac{\sigma}{4\pi}\sum_{n=0}^{\infty}\tau^n q_n(a,b) \tag{10}$$

is useful. The geometry-dependent coefficients $q_n(a,b)$, which are obtained by substituting (9) into (1), expanding in τ^n and integrating term by term, are given in section 5.2.

2. Notation and Definitions

Notation relevant to this paper, much of which has already been introduced, is listed for convenience as follows:

detector=device with response proportional to the radiation flux at a given point in space,

S=symbolic reference to a specific surface lying in the x,y plane,

h=distance from surface to detector in the z-direction,

w,l=width and length of a rectangular surface,

x,y=rectangular coordinates parallel to w and l, respectively, with origin at one corner of the rectangle,

corner position=detector position on a line perpendicular to the rectangle at one of its corners, i.e., at $(0,0,h)$,

$a=w/h$, $b=l/h$,

$\alpha=x/h$, $\beta=y/h$,

dS=element of area of the surface S,

θ=obliquity with respect to the z axis,

φ=azimuth of the plane through the z axis and the center of dS, measured from the x,z plane,

$\psi_S(\theta)$=range of φ covered by all surface elements dS from which the detector can be seen at obliquity θ,

$\psi(\theta,a,b)=\psi_S(\theta)$ when S refers to a rectangle and the detector is in a corner position,

r=distance from dS to the detector,

$d\Omega_S(\theta)$=solid angle subtended from the detector by element dS at obliquity θ
$=dS\cdot\cos\theta/r^2$,

$g(\cos\theta)$=radiation flux (e.g., number of photons) traveling in direction θ per unit solid angle, unit time, and unit area normal to direction θ,

g_l=coefficients of a Legendre polynomial expansion of $g(\cos\theta)$,

p_l=coefficients of a Legendre polynomial expansion of $\psi_S(\theta)$,

I_S=response of an isotropic detector to surface S radiating according to $g(\cos\theta)$, above,

$I(a,b)=I_S$ when S is a rectangle and the detector is in a corner position,

$I(a,b;\alpha,\beta)=I_S$ when the detector lies at $(h\alpha,h\beta,h)$.

The remaining quantities refer specifically to applications involving penetrating radiations, typified by the "fallout problem" shown in figure 3:

$\tau=\mu t$=mean-free-path thickness of layers of material between primary source and the electron, where μ is the attenuation coefficient in reciprocal units of the linear thickness t,

$\sigma/4\pi$=surface density of contaminant, in the case of the fallout problem, in units of photons emitted per unit time from unit surface area into unit solid angle,

$I(\tau,a,b)=I^o(\tau,a,b)+I^s(\tau a,b)$
=the detector response to the unscattered and scattered components, respectively, of radiation transmitted by a slab barrier having thickness τ and a rectangular exit surface of dimensions a,b.

3. Arbitrary Detector Positions

Although the results in this paper relate directly to the response of a detector in a corner position, the response at an arbitrary position (α,β) (shown in fig. 4) is of more general interest.

A compounding rule found in standard illuminating engineering texts [10] yields the detector response, $I(a,b;\alpha,\beta)$, at such a position by combining corner-position data from four related rectangles:

$$I(a,b;\alpha,\beta)=I(\alpha,\beta)+I(a-\alpha,\ b-\beta)+I(\alpha,\ b-\beta)+I(a-\alpha,\ \beta), \tag{11}$$

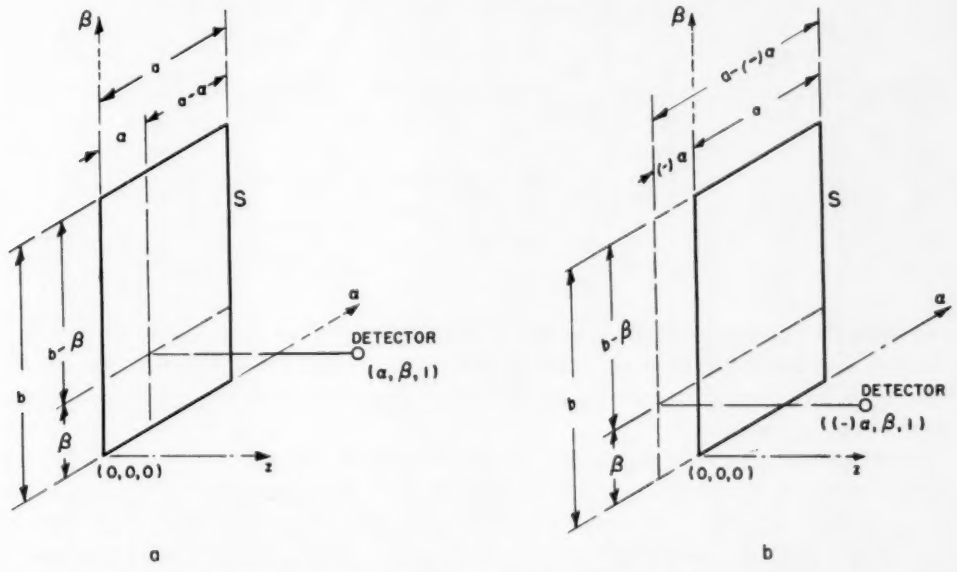

a b

FIGURE 4. *Examples using the scaled coordinates of figure 3, of noncorner positions (a) within the rectangular area directly under the source and (b) outside this area.*

in which the terms on the right are obtained by replacing the parameters (a,b) of (6) or (10) by the quantities indicated. Since both (6) and (10) are odd functions in ab, i.e.,

$$I(\pm a,\mp b)=-I(a,b), \tag{12}$$

the rule in (11) applies not only to detector positions $0\leq\alpha\leq a$, $0\leq\beta\leq b$ as in figure 4a, but to any position $-\infty<\alpha<+\infty$, $-\infty<\beta<+\infty$ as shown in the example in figure 4b.

4. Legendre Expansion of the Response Function

4.1. Isotropic Detector

The primary task performed in this work is the evaluation of the Legendre expansion coefficients $p_l(a,b)$ by performing the integrations indicated in (8).

Use of scaled cartesian coordinates leads to the transformations

$$\cos\theta=h/r=1/\sqrt{\alpha^2+\beta^2+1} \tag{13}$$

and

$$d\Omega_S(\theta)=dS\cdot\cos\theta/r^2=d\alpha d\beta\cdot(\alpha^2+\beta^2+1)^{-3/2} \tag{14}$$

so that we may write (8) explicitly as

$$p_l(a,b)=\int_0^a d\alpha\int_0^b d\beta\cdot(\alpha^2+\beta^2+1)^{-\frac{3}{2}}\cdot P_l(1/\sqrt{\alpha^2+\beta^2+1}). \tag{15}$$

Evaluation of this family of double integrals is outlined in appendix A. The first four $p_l(a,b)$'s were found to be

$$p_0(a,b)=\tan^{-1}\frac{ab}{\sqrt{a^2+b^2+1}}, \tag{16}$$

$$p_1(a,b)=\frac{1}{2}\left\{\frac{b}{\sqrt{b^2+1}}\tan^{-1}\frac{a}{\sqrt{b^2+1}}+\frac{a}{\sqrt{a^2+1}}\tan^{-1}\frac{b}{\sqrt{a^2+1}}\right\} \tag{17}$$

$$p_2(a,b)=\frac{1}{2}\frac{ab}{\sqrt{a^2+b^2+1}}\left\{\frac{1}{a^2+1}+\frac{1}{b^2+1}\right\}, \tag{18}$$

and

$$\begin{aligned}p_3(a,b)=\frac{1}{8}\Bigg\{&-\left(\frac{b}{\sqrt{b^2+1}}\tan^{-1}\frac{a}{\sqrt{b^2+1}}+\frac{a}{\sqrt{a^2+1}}\tan^{-1}\frac{b}{\sqrt{a^2+1}}\right)\\&+\frac{5}{2}\Bigg[\frac{b}{(b^2+1)^{\frac{3}{2}}}\tan^{-1}\frac{a}{\sqrt{b^2+1}}+\frac{a}{(a^2+1)^{\frac{3}{2}}}\tan^{-1}\frac{b}{\sqrt{a^2+1}}\\&+\frac{ab}{a^2+b^2+1}\left(\frac{1}{a^2+1}+\frac{1}{b^2+1}\right)\Bigg]\Bigg\}.\end{aligned} \tag{19}$$

The $p_0(a,b)$ term is the result given by Spencer [2] for a diffuse (i.e., $g(\cos\theta)=$constant) rectangular source and isotropic detector, and $p_1(a,b)$ is the result given by illumination [5–8] and heat-exchange [9] engineering studies for a diffuse rectangular source and a surface-type detector parallel to the source plane.

The terms become progressively more complicated with increasing l, but the even and odd general terms as given by (38) and (42) in appendix A are amenable to programing for an automatic computer. Table 1 contains $p_l(a,b)$'s evaluated using an IBM type 704 computer for $0\leq l\leq 13$ over a grid of a and b values $0.1\leq a\leq b\leq 20$. These may now be inserted in (6) to give the detector response $I(a,b)$ in a corner position.

These $p_l(a,b)$'s may be checked by reconstructing $\psi(\theta,a,b)$ according to (7) and comparing with the exact results given in reference [1]. As shown in figure 5, ψ (θ,a,b) is reasonably well described for the case $a=1$, $b=2$, neglecting terms in excess of $l=7$. If, however, higher g_l terms are available and contain appreciable information, as for a severely peaked angular distribution, greater accuracy may be achieved by including additional terms in (6).

4.2. Cosine Detector

The g_l coefficients may in principle be generated for *any* azimuthally independent uniform plane source by performing the integration indicated in (5) by analytic, numerical, or graphical means. Thus the Legendre expansion method might also be fruitful in similar rectangular source studies in illumination and heat-exchange engineering in which the $g(\cos\theta)$ is known. In these studies, however, the radiation field is usually described in terms of a surface-element detector ("plane detector") whose response is proportional to the cosine of the angle of incidence.

The orientation of such a plane detector may be specified by its direction cosines A, B, and C with respect to the α, β, and z axes. Legendre expansion coefficients $p_{l,A,B,C}(a,b)$ (analogous to the isotropic detector $p_l(a,b)$'s) may each be written as the sum of three components (see ref [8], eq (17)),

$$p_{l,A,B,C}(a,b)=Ap_{l\alpha}(a,b)+Bp_{l\beta}(a,b)+Cp_{lz}(a,b), \tag{20}$$

where $p_{l\alpha}$ (a,b) and $p_{l\beta}$ (a,b) are the Legendre coefficients for a plane detector perpendicular to S and to the α- or β-axis, respectively, and the p_{lz} (a,b)'s are the coefficients for a detector parallel to S, i. e., perpendicular to the z-axis.

TABLE 1.* *Coefficients* $p_l(a, b)$ *of the Legendre expansion* (7) *of the angular response function* $\psi(\theta, a, b)$

l	b=0.1 a=0.1	b=0.2 a=0.1	b=0.2 a=0.2	b=0.5 a=0.1	b=0.5 a=0.2	b=0.5 a=0.5
0	9.9012 (−3)	1.9516 (−2)	3.8471 (−2)	4.4514 (−2)	8.7819 (−2)	2.0136 (−1)
1	9.8685	1.9358	3.7980	4.2915	8.4281	1.8807
2	9.8034	1.9046	3.7010	3.9869	7.7547	1.6330
3	9.7064	1.8585	3.5587	3.5656	6.8256	1.3035
4	9.5781	1.7984	3.3750	3.0658	5.7261	9.3443 (−2)
5	9.4193	1.7254	3.1545	2.5301	4.5524	5.7010
6	9.2312	1.6408	2.9031	2.0015	3.3997	2.4985
7	9.0151	1.5461	2.6270	1.5177	2.3514	2.2553 (−4)
8	8.7724	1.4430	2.3332	1.1076	1.4701	−1.5825 (−2)
9	8.5047	1.3333	2.0287	7.8884 (−3)	7.9220 (−3)	−2.3202
10	8.2140	1.2188	1.7206	5.6642	3.2668	−2.3214
11	7.9020	1.1015	1.4159	4.3403	5.7140 (−4)	−1.8030
12	7.5710	9.8316 (−3)	1.1211	3.7609	−5.2395	−1.0173
13	7.2231	8.6565	8.4197 (−3)	3.7105	−4.9818	−2.0192 (−3)

l	b=1.0 a=0.1	b=1.0 a=0.2	b=1.0 a=0.5	b=1.0 a=1.0	b=2.0 a=0.1	b=2.0 a=0.2
0	7.0418 (−2)	1.3912 (−1)	3.2175 (−1)	5.2360 (−1)	8.9117 (−2)	1.7632 (−1)
1	6.3910	1.2572	2.8332	4.3521	7.4970	1.4769
2	5.2552	1.0233	2.1667	2.8868	5.3170	1.0348
3	3.9093	7.4574 (−2)	1.3858	1.3137	3.2627	6.1652 (−2)
4	2.6458	4.8456	6.6728 (−2)	8.0187 (−3)	1.9494	3.4619
5	1.6848	2.8473	1.4080	−5.6244 (−2)	1.4458	2.3811
6	1.1172	1.6480	−1.4393	−6.2546	1.3947	2.2105
7	8.9990 (−3)	1.1601	−2.1736	−3.2689	1.3716	2.1019
8	8.9914	1.1114	−1.6157	4.4199 (−3)	1.1807	1.6654
9	9.5780	1.1850	−6.8461 (−3)	2.6786 (−2)	8.9548 (−3)	1.0498
10	9.5857	1.1468	−3.5674 (−4)	2.7119	6.8459	5.9365 (−3)
11	8.5803	9.1332 (−3)	1.0787 (−3)	1.1910	6.2105	4.4251
12	6.8321	5.4331	−1.0131	−5.9052 (−3)	6.3528	4.5618
13	4.9912	1.6968	−3.4306	−1.5587 (−2)	6.1304	4.0585

l	b=2.0 a=0.5	b=2.0 a=1.0	b=2.0 a=2.0	b=5.0 a=0.1	b=5.0 a=0.2	b=5.0 a=0.5
0	4.1152 (−1)	6.8472 (−1)	9.2730 (−1)	9.7727 (−2)	1.9351 (−1)	4.5396 (−1)
1	3.3564	5.2582	6.5269	7.7896	1.5352	3.4997
2	2.1822	2.8577	2.6667	5.0420	9.7983 (−2)	2.0456
3	1.0654	7.0518 (−2)	−2.6030 (−2)	2.9189	5.4792	8.9638 (−2)
4	3.3703 (−2)	−4.0423	−1.2049 (−1)	1.9463	3.4566	3.3712
5	4.3254 (−3)	−6.6172	−6.0731 (−2)	1.7051	2.8992	1.7192
6	7.2294 (−4)	−2.9200	2.8998	1.5548	2.5295	8.4961 (−3)
7	1.3615 (−3)	8.1359 (−3)	5.6423	1.2639	1.8859	−4.1356
8	−3.9207	1.9132 (−2)	1.9243	9.8612 (−3)	1.2767	−1.3530 (−2)
9	−1.1888 (−2)	9.8109 (−3)	−2.5299	8.6130	9.8248 (−3)	−1.3389
10	−1.4791	−8.7945 (−4)	−3.1339	8.1909	8.6299	−8.0041 (−3)
11	−9.9201 (−3)	−2.6009 (−3)	−3.7923 (−3)	7.3200	6.6370	−4.5171
12	−1.6638	9.0735 (−4)	2.0619 (−2)	5.9839	3.8145	−3.6896
13	3.7038	1.4956 (−3)	1.7773	5.0339	1.8646	−1.7941

l	b=5.0 a=1.0	b=5.0 a=2.0	b=5.0 a=5.0	b=10.0 a=0.1	b=10.0 a=0.2	b=10.0 a=0.5
0	7.6616 (−1)	1.0697 (0)	1.2925 (0)	9.9172 (−2)	1.9640 (−1)	4.6117 (−1)
1	5.5285	6.9768 (−1)	7.6053 (−1)	7.8117	1.5396	3.5108
2	2.5907	2.1768	1.3464	4.9749	9.6643 (−2)	2.0122
3	3.8325 (−2)	−8.0873 (−2)	−1.6067	2.8872	5.4156	8.8055 (−2)
4	−4.7545	−1.1485 (−1)	−9.3400 (−2)	1.9878	3.5396	3.5782
5	−4.1089	−1.5559 (−2)	5.5039	1.7418	2.9725	1.9018
6	−1.4967	5.0088	6.8498	1.5308	2.4815	7.2960 (−3)
7	−3.3765 (−3)	3.2101	−1.4585	1.2260	1.8101	−6.0253
8	6.9961 (−4)	−1.1825	−4.9763	9.9606 (−3)	1.2966	−1.3032 (−2)
9	7.9552 (−3)	−2.3266	−4.7962 (−3)	8.9743	1.0547	−1.1588
10	1.2904 (−2)	−4.7751 (−3)	3.4526 (−2)	8.2073	8.6626 (−3)	−7.9255 (−3)
11	7.2894 (−3)	9.7856	1.4253	7.0017	6.0006	−6.1052
12	−4.0976	6.8161	−2.1923	5.8764	3.5995	−4.2231
13	−9.4124	−1.0631	−1.8035	5.2905	2.3776	−5.1238 (−4)

l	b=10.0 a=1.0	b=10.0 a=2.0	b=10.0 a=5.0	b=10.0 a=10.0	b=20.0 a=0.1	b=20.0 a=0.2
0	7.8045 (−1)	1.0973 (0)	1.3500 (0)	1.4300 (0)	9.9544 (−2)	1.9715 (−1)
1	5.5503	7.0183 (−1)	7.6864 (−1)	7.7903 (−1)	7.8146	1.5402
2	2.5244	2.0484	1.0771	6.9836 (−2)	4.9567	9.6278 (−2)
3	3.5197 (−2)	−8.6847 (−2)	−1.7179	−1.8686 (−1)	2.8829	5.4071
4	−4.3432	−1.0684 (−1)	−7.6187 (−2)	−5.1368 (−2)	2.0009	3.5657
5	−3.7478	−8.6468 (−3)	6.8721	8.6458	1.7470	2.9830
6	−1.7360	4.5362 (−2)	5.7789	4.1505	1.5206	2.4612
7	−7.1162 (−3)	2.4916	−2.9008	−4.7938	1.2200	1.7982
8	1.7058	−9.7509 (−3)	−4.4287	−3.4798	1.0040	1.3126
9	1.1525 (−2)	−1.6370 (−2)	9.3314 (−3)	2.8212	9.0385 (−3)	1.0675
10	1.3040	−4.6562 (−3)	3.3426 (−2)	2.9638	8.1452	8.5385 (−3)
11	4.1349 (−3)	3.6459	1.2963 (−3)	−1.6478	6.9345	5.8661
12	−5.1356	4.9501	−2.4409 (−2)	−2.5371	5.9230	3.6927
13	−6.8582	3.9658	−6.9441 (−3)	8.8627 (−3)	5.3592	2.5151

See footnote at end of table, p. 128.

TABLE 1.* *Coefficients* p_l(a, b) *of the Legendre expansion* (7) *of the angular response function* $\psi(\theta, a, b)$—Continued

l	b=20.0 a=0.5	b=20.0 a=1.0	b=20.0 a=2.0	b=20.0 a=5.0	b=20.0 a=10.0	b=20.0 a=20.0
0	4.6302 (−1)	7.8415 (−1)	1.1047 (0)	1 3673 (0)	1.4593 (0)	1.5002 (0)
1	3.5122	5.5532	7.0240 (−1)	7.6994 (−1)	7.8112 (−1)	7.8379 (−1)
2	2.0031	2.5062	2.0124	9.9215 (−2)	5.5376 (−2)	3.5245 (−2)
3	8.7841 (−2)	3.4772 (−2)	−8.7686 (−2)	−1.7372 (−1)	−1.8997 (−1)	−1.9395 (−1)
4	3.6436	−4.2128	−1.0426 (−1)	−7.0077 (−2)	−4.0924 (−2)	−2.6306 (−2)
5	1.9280	−3.6957	−7.6179 (−3)	7.1094	9.0285	9.5183
6	6.7898 (−3)	−1.8370	4.3358 (−2)	5.3034	3.3318	2.1754
7	−6.3214	−7.7066 (−3)	2.3750	−3.1702	−5.2295	−5.7885
8	−1.2633 (−2)	2.5016	−8.1707 (−3)	−4.0518	−2.8235	−1.8836
9	−1.1268	1.2164 (−2)	−1.5107 (−2)	1.2254	3.2956	3.9067
10	−8.2358 (−3)	1.2420	−5.8884 (−3)	3.0463	2.4392	1.6728
11	−6.4412	3.4648 (−3)	2.3212	−1.7760 (−3)	−2.1487	−2.7972
12	−3.9897	−4.6694	5.8792	−2.2148 (−2)	−2.1264	−1.5087
13	−1.6924 (−4)	−6.1736	5.3201	−3.7939 (−3)	1.4029	2.0756

*Note: The figures in parenthesis in tables 1, 2, 3, and 4 indicate the power of ten by which the numbers alongside and below in the same column are to be multiplied; e.g., 9.9012(−3)=0.0099012.

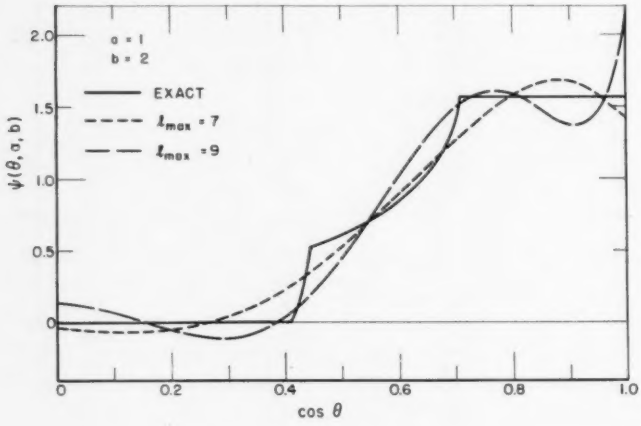

FIGURE 5. *Reconstruction of the response function* $\psi(\theta,a,b)$ *according to* (10) *for* $a=b=1$ *using terms* $0\leq l\leq 7$ *(dotted line) and* $0\leq l\leq 9$ *(dashed line). The exact function as given by Berger and Lamkin* [1] *is shown as the solid line.*

The dependence on the angle of incidence of radiation on a plane detector for geometries described by $p_{l\alpha}$ (a,b) and $p_{l\beta}$ (a,b) reduces to $\alpha \cos\theta$ and $\beta \cos\theta$, respectively, modifying the integrand in (15) to give

$$p_{l\alpha}(a,b)=\int_0^b d\beta\int_0^a \alpha d\alpha P_l(1/\sqrt{\alpha^2+\beta^2+1})/(\alpha^2+\beta^2+1)^2 \tag{21}$$

and

$$p_{l\beta}(a,b)=\int_0^a d\alpha\int_0^b \beta d\beta P_l(1/\sqrt{\alpha^2+\beta^2+1})/(\alpha^2+\beta^2+1)^2. \tag{22}$$

Evaluation of these integrals should be similar to that for (15). In the geometry described by the p_{lz} (a,b)'s, the angles of emission and incidence are identical, so that the integrand in (15) requires only an additional factor of $\cos\theta$. Thus, using the relation

$$\cos\theta P_l(\cos\theta)=\{lP_{l-1}(\cos\theta)+(l+1)P_{l+1}(\cos\theta)\}/(2l+1), \tag{23}$$

the p_{lz} (a,b)'s may be obtained from the p_l (a,b)'s in table 1 as

$$P_{lz}(a,b)=\{lp_{l-1}(a,b)+(l+1)p_{l+1}(a,b)\}/(2l+1). \tag{24}$$

5. Unscattered Radiation Component

In cases involving penetrating radiations, such as gamma rays from the plane source shown in figure 3, it is usually desirable to make a separate calculation of the unscattered radiation component, $I^o(\tau,a,b)$. Two reasons for this separation of components are:

(a) In contrast to the scattered radiation component, $I^s(\tau,a,b)$, the unscattered component, $I^o(\tau,a,b)$, is analytic in nature and independent of the barrier material, so that it may be calculated once and for all for the relevant parameters τ, a, and b.

(b) Since the angular distribution, $g^o(\tau, \cos\theta)$, of unscattered radiation from a plane isotropic source as expressed in (9) tends toward $\frac{\sigma}{4\pi}(1/\cos\theta)$ as τ becomes small, representation as a Legendre expansion in positive powers of $\cos\theta$ becomes impractical. This difficulty usually does not arise for the scattered component.

5.1. $\tau \gtrsim 1$: Legendre Expansion

In order to examine the behavior discussed in (b), above, $g_l^o(\tau)$'s were evaluated by substituting (9) into (5). The result

$$g_l^o(\tau)=\frac{\sigma}{4\pi}\{P_l E_{j+1}(\tau)\}, \tag{25}$$

where $E_j(\tau)$ is the exponential integral [11]

$$E_j(\tau)=\int_1^\infty e^{-\tau u}u^{-j}du, \tag{26}$$

and $P_l\{E_{j+1}(\tau)\}$ is obtained by replacing $(\cos\theta)^j$ in $P_l(\cos\theta)$ by $E_{j+1}(\tau)$. Since these $g_l^o(\tau)$, although of fairly general interest, do not seem to appear explicitly in the literature, a tabulation of the quantity $\frac{4\pi}{\sigma}(l+\frac{1}{2})g_l^o(\tau)$, (i.e., $(l+\frac{1}{2})P_l\{E_{j+1}(\tau)\}$), for $0 \leq l \leq 13$ and $0.001 \leq \tau \leq 100$ is presented in table 2.

A check on the values in table 2 is shown in figure 6, in which $(4\pi/\sigma)e^\tau g^o(\tau, \cos\theta)$, reconstructed according to (4) for $0 \leq l \leq 7$ and $0.2 \leq \tau \leq 10$, are indicated by the dotted curves. Comparison may now be made with similar results from the exact expression (9), shown by the

TABLE 2. *Coefficients* $(4\pi/\sigma)(l+\frac{1}{2})g_l^o(\tau)$ *of a Legendre expansion* (4) *of the angular distribution* $(4\pi/\sigma)g^o(\tau, \cos\theta)$ *of unscattered radiation from a plane isotropic source*

The factor $4\pi/\sigma$ implies unit source strength per steradian per unit of source area, and $(l+\frac{1}{2})$ is included to allow cumulative multiplication directly with the $p_l(a,b)$'s (see table 1) according to (6).

l \ τ	0.001	0.01	0.1	0.2	0.5	1.0
0	3.1943 (0)	2.0190 (0)	9.1145 (−1)	6.1135 (−1)	2.7989 (−1)	1.0970 (−1)
1	1.4889	1.4245	1.0838 (0)	8.6130	4.8996	2.2275
2	−6.1143	−3.2090	−7.1755 (−1)	−2.0852	1.3130	1.3712
3	−2.2989	−2.1124	−1.2757 (0)	−8.3188	−2.6901	−2.6555 (−2)
4	7.2752	3.3973	3.6314 (−1)	−9.1715 (−2)	−2.1634	−9.3776
5	2.8703	2.5450	1.2524 (0)	6.7606 (−1)	1.0298	−3.3952
6	−8.0184	−3.4034	−9.6551 (−2)	2.4954	1.9507	4.0965
7	−3.3335	−2.8604	−1.1624 (0)	−5.1631	−8.9640 (−3)	3.9813
8	8.5595	3.3377	−9.7963 (−2)	−3.2542	−1.4873 (−1)	−9.6373 (−3)
9	3.7303	3.1040	1.0492 (0)	3.7667	−3.8228 (−2)	−3.0111 (−2)
10	−8.9790	−3.2372	2.3859 (−1)	3.5348	1.0293 (−1)	−4.9996 (−3)
11	−4.0810	−3.2983	−9.3042	−2.6113	5.7819 (−2)	1.8731 (−2)
12	9.3161	3.1186	−3.3868	−3.5306	−6.4944	1.0139
13	4.3971	3.4559	8.1428	3.3172	−6.1991	−9.7479 (−3)

l \ τ	2.0	5.0	10.0	15.0	20.0	100.0
0	2.4451 (−2)	5.7415 (−4)	2.0785 (−6)	9.5930 (−9)	4.9178 (−11)	1.8418 (−46)
1	5.6301	1.4947 (−3)	5.7483	2.7162 (−8)	1.4107 (−10)	5.4717
2	5.1875	1.8564	8.1118	4.0293	2.1490	8.9433
3	2.1895	1.6196	8.8022	4.7268	2.6263	1.2159 (−45)
4	−6.1965 (−3)	1.0195	7.9587	4.7804	2.8115	1.5034
5	−1.4221 (−2)	3.9434 (−4)	6.1188	4.2970	2.7243	1.7498
6	−5.7195 (−3)	−1.1402 (−5)	3.9668	3.4702	2.4242	1.9500
7	3.9476	−1.4339 (−4)	2.0817	2.5187	1.9934	2.1009
8	5.1706	−9.8609 (−5)	9.1367 (−7)	1.6300	1.5167	2.2013
9	5.1102 (−4)	−1.3120	8.0998 (−8)	9.1882 (−9)	1.0653	2.2522
10	−2.6394	3.0530	−1.5133 (−7)	4.3555	6.8479 (−11)	2.2561
11	−1.5451	2.4977	−1.4134	1.4721	4.0174	2.2172
12	8.7741	3.8280 (−6)	−5.0961 (−8)	1.6851 (−10)	2.0205	2.1418
13	1.2960 (−3)	−9.5729 (−6)	4.5106 (−9)	−2.5223 (−11)	9.8335 (−12)	2.0335

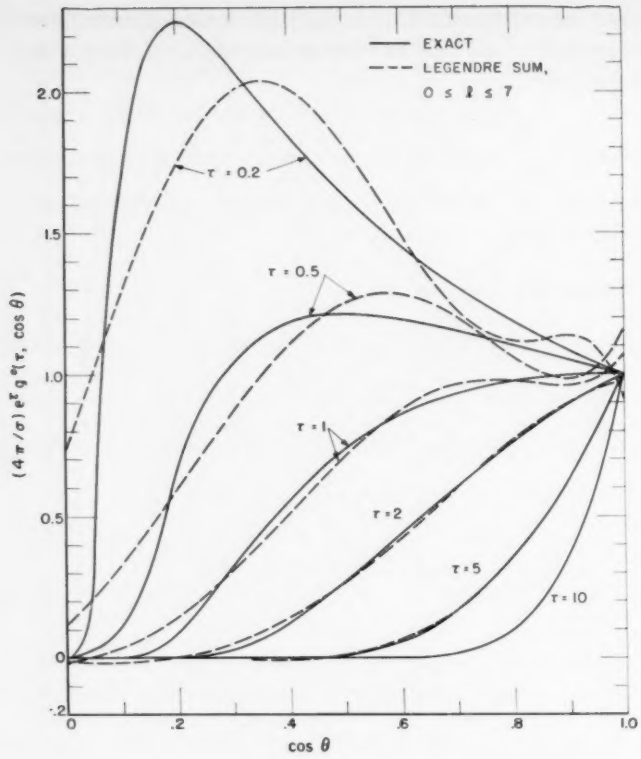

FIGURE 6. *The angular distribution of unscattered radiation from a plane isotropic source reconstructed according to (4) and (25) (dotted lines) as compared with the exact expression (9) (solid lines) for* $0.2 \leq \tau \leq 10$.

solid curves. From both table 2 and figure 6 it can be seen that the Legendre expansion approach, using tables 1 and 2, should give reliable results for *unscattered* as well as scattered radiation in the region $1 \lesssim \tau \lesssim 15$.

5.2. $\tau \lesssim 1$: Power Series Expansion

The parameter τ may in some cases be very small, and for this reason it seemed desirable to find a method for evaluating $I^o(\tau,a,b)$, i.e.,

$$I^o(\tau,a,b)=\frac{\sigma}{4\pi}\int_S (dS/r^2)\exp(-\tau/\cos\theta), \tag{27}$$

for small τ. No success was had in obtaining a closed-form result, but $q_n(a,b)$ coefficients of the τ^n power series in (10) were evaluated (see appendix B) which provide adequate convergence of (10) from $\tau=0$ up to values of τ for which the $g_l^o(a,b)$'s converge rapidly.

The first five $q_n(a,b)$ terms are

$$q_0(a,b)=\frac{\pi}{2}\sinh^{-1}a-\frac{b}{a}\sum_{i=0}^{\infty}\frac{1}{2i+1}\left(\frac{a^2}{a^2+1}\right)^{i+1}\left\{\frac{\sqrt{a^2+1}}{b}\tan^{-1}\frac{\sqrt{a^2+1}}{b}-\sum_{j=0}^{i-1}\frac{2^{2j}(j!)^2}{(2j+1)!}\left(\frac{a^2+1}{a^2+b^2+1}\right)^{j+1}\right\}, \tag{28}$$

in which the inner sum over j vanishes for $i=0$,

$$q_1(a,b)=-\left\{b\sinh^{-1}\frac{a}{\sqrt{b^2+1}}+a\sinh^{-1}\frac{b}{\sqrt{a^2+1}}-\tan^{-1}\frac{ab}{\sqrt{a^2+b^2+1}}\right\}, \tag{29}$$

$$q_2(a,b)=\frac{ab}{2!}, \tag{30}$$

$$q_3(a,b)=-\frac{1}{3!}\left\{-\frac{q_1(a,b)}{3}+\frac{1}{2\cdot3}\left[b(b^2+1)\sinh^{-1}\frac{a}{\sqrt{b^2+1}}+a(a^2+1)\sinh^{-1}\frac{b}{\sqrt{a^2+1}}\right]+\frac{ab\sqrt{a^2+b^2+1}}{3}\right\}, \tag{31}$$

and

$$q_4(a,b)=\frac{1}{4!}\left\{(2!)q_2(a,b)+\frac{a^3b}{3\cdot1}+\frac{ab^3}{1\cdot3}\right\}. \tag{32}$$

For large a and b, $(a\leq b)$, the expression within the braces in (28) becomes small very quickly with increasing i. Indeed, over the *entire range* of a and b, i.e., $0\leq a\leq b\leq\infty$, summation over i from $i=0$ to $i=6$ gives values for $q_0\ (a,b)$ departing less than 0.01 percent from their respective values when the summation is carried to $i>20$. A partial check of (28) is obtained by noting that the series part of the expression vanishes for large b, that is,

$$\lim_{b\to\infty} q_0(a,b)=\frac{\pi}{2}\sinh^{-1}a, \tag{33}$$

in agreement with the result of Andrews [12] for the detector response to an infinite strip source in a nonattenuating medium.

The remaining $q_n\ (a,b)$ terms form two distinct sets, as did the $p_l\ (a,b)$'s, depending on whether n is even or odd. The general terms for these sets are given in (57) and (58) of appendix B.

Values of $I^o\ (\tau,a,b)4\pi/\sigma$ for $0.01\ \leq\tau\leq\ 10$ and $0.1\ \leq a\leq b\leq\ 20$, as evaluated with the help of an IBM 704 computer, are presented in table 4. Numbers preceded by asterisks were evaluated using the Legendre expansion approach (15) and (25) for $0\leq l\leq\ 13$, and the others using the τ^n series (10) for $0\leq n\leq\ 20$.

Since evaluation of (10) for small specific values of τ may be faster than interpolation from table 4, $q_n\ (a,b)$ is given in table 3 for $0\ \leq n\leq 9$ and $0.1<a<b<\ 20$.

TABLE 3. *Coefficients* $q_n(a,b)$ *of the* τ^n *power series expansion (10) of the corner position flux* $I^\circ\ (\tau,a,b)$ *of unscattered radiation from a rectangular plane isotropic source*

n	$b=0.1$ $a=0.1$	$b=0.2$ $a=0.1$	$b=0.2$ $a=0.2$	$b=0.5$ $a=0.1$	$b=0.5$ $a=0.2$	$b=0.5$ $a=0.5$
0	9.9340 (−3)	1.9675 (−2)	3.8971 (−2)	4.6222 (−2)	9.1603 (−2)	2.1600 (−1)
1	−9.9669	−1.9836	−3.9481	−4.8047	−9.5656	−2.3215
2	5.0000	10.0000 (−3)	2.0000	2.5000	5.0000	1.2500
3	−1.6722	−3.3609	−6.7547 (−3)	−8.6819 (−3)	−1.7443	−4.4960 (−2)
4	4.1944 (−4)	8.4722 (−4)	1.7111	2.2639	4.5694 (−3)	1.2153
5	−8.4169 (−5)	−1.7086	−3.4679 (−4)	−4.7282 (−4)	−9.5873 (−4)	−2.6333 (−3)
6	1.4075	2.8716 (−5)	5.8574 (−5)	8.2390 (−5)	1.6783	4.7647 (−4)
7	−2.0174 (−6)	−4.1368 (−6)	−8.4805 (−6)	−1.2320	−2.5213 (−5)	−7.4048 (−5)
8	2.5302 (−7)	5.2148 (−7)	1.0744	1.6141 (−6)	3.3183 (−6)	1.0090
9	−2.8208 (−8)	−5.8435 (−8)	−1.2101 (−7)	−1.8819 (−7)	−3.8869 (−7)	−1.2248 (−6)

n	$b=1.0$ $a=0.1$	$b=1.0$ $a=0.2$	$b=1.0$ $a=0.5$	$b=1.0$ $a=1.0$	$b=2.0$ $a=0.1$	$b=2.0$ $a=0.2$
0	7.8327 (−2)	1.5540 (−1)	3.6887 (−1)	6.3951 (−1)	1.1046 (−1)	2.1946 (−1)
1	−8.8020	−1.7535	−4.2718	−7.9336	−1.4421	−2.8755
2	5.0000	10.0000 (−2)	2.5000	5.0000	10.0000 (−2)	2.0000
3	−1.9154	−3.8455	−9.8624 (−2)	−2.1346	−4.9338	−9.8916 (−2)
4	5.5694 (−3)	1.1222	2.9514	6.9444 (−2)	1.9472	3.9111
5	−1.3114	−2.6517 (−3)	−7.1478 (−3)	−1.8357	−6.5195 (−3)	−1.3113
6	2.6050 (−4)	5.2848 (−4)	1.4593	4.1049 (−3)	1.9117	3.8496 (−3)
7	−4.4892 (−5)	−9.1365 (−5)	−2.5829 (−4)	−7.9826 (−4)	−5.0012 (−4)	−1.0081
8	6.8492 (−6)	1.3982	4.0448 (−5)	1.3771	1.1811	2.3829 (−4)
9	−9.3939 (−7)	−1.9233 (−6)	−5.6906 (−6)	−2.1392 (−5)	−2.5399 (−5)	−5.1290 (−5)

n	$b=2.0$ $a=0.5$	$b=2.0$ $a=1.0$	$b=2.0$ $a=2.0$	$b=5.0$ $a=0.1$	$b=5.0$ $a=0.2$	$b=5.0$ $a=0.5$
0	5.2536 (−1)	9.3072 (−1)	1.4074 (0)	1.3708 (−1)	2.7263 (−1)	6.5729 (−1)
1	−7.0456	−1.3285 (0)	−2.2916	−2.3108	−4.6120	−1.1372 (0)
2	5.0000	1.0000	2.0000	2.5000	5.0000	1.2500
3	−2.5139	−5.3007 (−1)	−1.2410	−2.3179	−4.6397	−1.1666
4	1.0069	2.2222	6.1111 (−1)	1.9451	3.8944	9.8090 (−1)
5	−3.4104 (−2)	−7.8243 (−2)	−2.5253	−1.4685	−2.9404	−7.4123
6	1.0095	2.3951	9.0494 (−2)	9.9117 (−2)	1.9849	5.0081
7	−2.6625 (−3)	−6.5116 (−3)	−2.8734	−5.9935	−1.2004	−3.0320
8	6.3366 (−4)	1.5949	8.2096 (−3)	3.2671	6.5448 (−2)	1.6550
9	−1.3730	−3.5550 (−4)	−2.1351	−1.6173	−3.2405	−8.2045 (−2)

TABLE 3. *Coefficients* $q_n(a,b)$ *of the* τ^n *power series expansion (10) of the corner position flux* $I^\circ(\tau,a,b)$ *of unscattered radiation from a rectangular plane isotropic source*—Continued

n	b=5.0 a=1.0	b=5.0 a=2.0	b=5.0 a=5.0	b=10.0 a= 0.1	b=10.0 a= 0.2	b=10.0 a= 0.5
0	1.1879 (0)	1.8793 (0)	2.7262 (0)	1.4685 (−1)	2.9217 (−1)	7.0607 (−1)
1	−2.1837	−3.9333	−7.3832	−2.9966	−5.9833	−1.4798 (0)
2	2.5000	5.0000	1.2500 (1)	5.0000	10.0000	2.5000
3	−2.3782	−5.0728	−1.6595	−8.6256	−1.7256 (0)	−4.3227
4	2.0139	4.4444	1.8403	1.4307 (0)	2.8622	7.1701
5	−1.5272	−3.4397	−1.7554	−2.1472	−4.2957	−1.0762 (1)
6	1.0353	2.3716	1.4695	2.8721	5.7461	1.4399
7	−6.2923 (−1)	−1.4665	−1.0971	−3.4332	−6.8689	−1.7217
8	3.4493	8.1909 (−1)	7.3983 (0)	3.6949	7.3929	1.8536
9	−1.7178	−4.1614	−4.5541	−3.6090	−7.2214	−1.8112

n	b=10.0 a= 1.0	b=10.0 a= 2.0	b=10.0 a= 5.0	b=10.0 a=10.0	b=20.0 a= 0.1	b=20.0 a= 0.2
0	1.2849 (0)	2.0692 (0)	3.1467 (0)	3.7961 (0)	1.5182 (−1)	3.0211 (−1)
1	−2.8671	−5.2864	−1.0571 (1)	−1.6127 (1)	−3.6878	−7.3658
2	5.0000	1.0000 (1)	2.5000	5.0000	10.0000	2.0000 (0)
3	−8.7046	−1.7838	−5.0356	−1.2892 (2)	−3.3683 (0)	−6.7373
4	1.4444 (1)	2.9722	8.8889	2.8194	1.1195 (1)	2.2391 (1)
5	−2.1687	−4.4719	−1.3854 (2)	−5.3227	−3.3586	−6.7176
6	2.9038	6.0067	1.9201	8.8285	8.9635	1.7928 (2)
7	−3.4758	−7.2190	−2.3848	−1.3066 (3)	−2.1364 (2)	−4.2732
8	3.7462	7.8159	2.6756	1.7475	4.5831	9.1672
9	−3.6647	−7.6824	−2.7323	−2.1341	−8.9221	−1.7846 (3)

n	b=20.0 a= 0.5	b=20.0 a= 1.0	b=20.0 a= 2.0	b=20.0 a= 5.0	b=20.0 a=10.0	b=20.0 a=20.0
0	7.3091 (−1)	1.3345 (0)	2.1679 (0)	3.3843 (0)	4.2228 (0)	4.8801 (0)
1	−1.8253 (0)	−3.5577	−6.6641	−1.3955 (1)	−2.2546 (1)	−3.3719 (1)
2	5.0000	1.0000 (1)	2.0000 (1)	5.0000	1.0000 (2)	2.0000 (2)
3	−1.6854 (1)	−3.3781	−6.8107	−1.7800 (2)	−3.9741	−1.0231 (3)
4	5.6007	1.1222 (2)	2.2611 (2)	5.9444	1.3972 (3)	4.4611
5	−1.6803 (2)	−3.3669	−6.7850	−1.7901 (3)	−4.3433	−1.6801 (4)
6	4.4847	8.9882	1.8127 (3)	4.8099	1.2006 (4)	5.5605
7	−1.0690 (3)	−2.1430 (3)	−4.3264	−1.1564 (4)	−2.9741	−1.6422 (5)
8	2.2935	4.5990	9.2953	2.5046	6.6542	4.3835
9	−4.4652	−8.9564	−1.8123 (4)	−4.9253	−1.3550 (5)	−1.0685 (6)

TABLE 4. *Unscattered flux* $(4\pi/\sigma)I^\circ(\tau,a,b)$ *of radiation, at a corner position, from a rectangular plane isotropic source calculated using tables 1 and 2 (numbers preceded by asterisks) and using table 3 (no asterisks)*

τ	b=0.1 a=0.1	b=0.2 a=0.1	b=0.2 a=0.2	b=0.5 a=0.1	b=0.5 a=0.2	b=0.5 a=0.5
0	9.93 (−3)	1.97 (−2)	3.90 (−2)	4.62 (−2)	9.16 (−2)	2.16 (−1)
0.01	9.83	1.95	3.86	4.57	9.07	2.14
0.02	9.74	1.93	3.82	4.53	8.97	2.11
0.05	9.44	1.87	3.70	4.39	8.69	2.05
0.1	8.99	1.78	3.52	4.17	8.25	1.94
0.2	8.13	1.61	3.18	3.75	7.43	1.74
	*8.48	*1.65	*3.21	*3.78	*7.44	*1.75
0.5	6.02	1.19	2.35	2.75	5.44	1.26
	*5.63	*1.15	*2.31	*2.72	*5.44	*1.26
1.0	3.64	7.18 (−3)	1.42 (−2)	1.64	3.23	7.38 (−2)
	*3.66	*7.02	*1.42	*1.64	*3.23	*7.38
2.0	1.34	2.62	5.14 (−3)	5.79 (−3)	1.14	2.53
	*1.37	*2.67	*5.20	*5.82	*1.14	*2.54
5.0	6.60 (−5)	1.28 (−4)	2.47 (−4)	2.60 (−4)	5.04 (−4)	1.04 (−3)
	*6.59	*1.27	*1.94	*2.59	*5.02	*1.03
10.0	*4.37 (−7)	*8.26 (−7)	*1.54 (−6)	*1.50 (−6)	*2.83 (−6)	*5.15 (−6)

τ	b=1.0 a=0.1	b=1.0 a=0.2	b=1.0 a=0.5	b=1.0 a=1.0	b=2.0 a=0.1	b=2.0 a=0.2
0	7.83 (−2)	1.55 (−1)	3.69 (−1)	6.40 (−1)	1.10 (−1)	2.19 (−1)
0.01	7.75	1.54	3.65	6.32	1.09	2.17
0.02	7.66	1.52	3.60	6.24	1.08	2.14
0.05	7.40	1.47	3.48	6.01	1.04	2.06
0.1	7.00	1.39	3.29	5.65	9.70 (−2)	1.93
0.2	6.26	1.24	2.93	4.99	8.53	1.69
	*6.28	*1.24	*2.93	*5.00	*8.53	*1.69
0.5	4.47	8.85 (−2)	2.07	3.45	5.82	1.15
	*4.45	*8.93	*2.07	*3.46	*5.79	*1.15
1.0	2.56	5.06	1.17	1.87	3.14	6.20 (−2)
	*2.57	*5.06	*1.17	*1.87	*3.14	*6.21
2.0	8.49 (−3)	1.67	3.74 (−2)	5.61 (−2)	9.57 (−3)	1.88
	*8.53	*1.67	*3.74	*5.62	*9.60	*1.88
5.0	3.85 (−4)	7.55 (−4)	1.77 (−3)	7.99 (−3)		
	*3.29	*6.35	*1.31	*1.69	*3.37 (−4)	*6.54 (−4)
10.0	*1.67 (−6)	*3.16 (−6)	*5.77 (−6)	*6.49 (−6)	*1.67 (−6)	*3.16 (−6)

TABLE 4. *Unscattered flux* $(4\pi/\sigma)I^{\circ}(\tau,a,b)$ *of radiation, at a corner position, from a rectangular plane isotropic source calculated using tables 1 and 2 (numbers preceded by asterisks) and using table 3 (no asterisks)*—Con.

τ	$b=2.0$ $a=0.5$	$b=2.0$ $a=1.0$	$b=2.0$ $a=2.0$	$b=5.0$ $a=0.1$	$b=5.0$ $a=0.2$	$b=5.0$ $a=0.5$
0	5.25 (−1)	9.31 (−1)	1.41 (0)	1.37 (−1)	2.73 (−1)	6.57 (−1)
0.01	5.18	9.18	1.38	1.35	2.68	6.46
0.02	5.11	9.05	1.36	1.33	2.64	6.35
0.05	4.91	8.67	1.30	1.26	2.51	6.03
0.1	4.60	8.07	1.20	1.16	2.31	5.55
0.2	4.03	7.01	1.02	9.93 (−2)	1.97	4.72
	*4.02	*6.99	*1.02	*9.97	*1.98	*4.73
0.5	2.72	4.62	6.38 (−1)	6.38	1.27	3.00
	*2.72	*4.62	*6.39	*6.35	*1.26	*2.99
1.0	1.44	2.35	3.02	3.27	6.46 (−2)	1.50
	*1.44	*2.35	*3.02	*3.27	*6.45	*1.50
2.0	4.24 (−2)	6.43 (−2)	7.46 (−2)			
	*4.24	*6.43	*7.45	*9.69 (−3)	*1.90	*4.28 (−2)
5.0	*1.32 (−3)	*1.75 (−3)	*1.80 (−3)	*3.37 (−4)	*6.54 (−4)	*1.35 (−3)
10.0	*5.79 (−6)	*6.51 (−6)	*6.52 (−6)	*1.67 (−6)	*3.16 (−6)	*5.79 (−6)

τ	$b=5.0$ $a=1.0$	$b=5.0$ $a=2.0$	$b=5.0$ $a=5.0$	$b=10.0$ $a=0.1$	$b=10.0$ $a=0.2$	$b=10.0$ $a=0.5$
0	1.19 (0)	1.88 (0)	2.73 (0)	1.47 (−1)	2.92 (−1)	7.06 (−1)
0.01	1.17	1.84	2.65	1.44	2.86	6.92
0.02	1.15	1.80	2.58	1.41	2.81	6.77
0.05	1.08	1.69	2.39	1.33	2.65	6.38
0.1	9.92 (−1)	1.53	2.10	1.21	2.41	5.79
0.2	8.35	1.26	1.64	1.02	2.02	4.84
	*8.37	*1.26	*1.65	*1.02	*2.02	*4.84
0.5	5.14	7.27 (−1)	8.53 (−1)	6.42 (−2)	1.27	3.01
	*5.14	*7.27	*8.49	*6.39	*1.27	*3.01
1.0	2.47	3.20	3.44			
	*2.47	*3.20	*3.44	*3.27	*6.47 (−2)	*1.50
2.0	*6.51 (−2)	*7.57 (−2)	*7.69 (−2)	*9.69 (−3)	*1.90	*4.28 (−2)
5.0	*1.75 (−3	*1.80 (−3)	*1.80 (−3)	*3.37 (−4)	*6.54 (−4)	*1.35 (−3)
10.0	*6.51 (−6)	*6.53 (−6)	*6.54 (−6)	*1.67 (−6)	*3.16 (−6)	*5.79 (−6)

τ	$b=10.0$ $a=1.0$	$b=10.0$ $a=2.0$	$b=10.0$ $a=5.0$	$b=10.0$ $a=10.0$	$b=20.0$ $a=0.1$	$b=20.0$ $a=0.2$
0	1.28 (0)	2.07 (0)	3.15 (0)	3.80 (0)	1.52 (−1)	3.02 (−1)
0.01	1.26	2.02	3.04	3.64	1.48	2.95
0.02	1.23	1.97	2.94	3.49	1.45	2.88
0.05	1.15	1.83	2.67	3.10	1.36	2.70
0.1	1.04	1.63	2.30	2.58	1.22	2.43
0.2	8.60 (−1)	1.31	1.74	1.86	1.02	2.03
	*8.58	*1.30	*1.73	*1.83	*1.06	*2.03
0.5	5.18	7.34 (−1)	8.65 (−1)	8.78 (−1)		
	*5.18	*7.33	*8.62	*8.77	*6.39 (−2)	*1.27
1.0	*2.47	*3.21	*3.44	*3.45	*3.27	*6.47 (−2)
2.0	*6.51 (−2)	*7.56 (−2)	*7.69 (−2)	*7.68 (−2)	*9.69 (−3)	*1.90
5.0	*1.75 (−3)	*1.80 (−3)	*1.80 (−3)	*1.80 (−3)	*3.37 (−4)	*6.54 (−4)
10.0	*6.51 (−6)	*6.53 (−6)	*6.53 (−6)	*6.53 (−6)	*1.67 (−6)	*3.16 (−6)

τ	$b=20.0$ $a=0.5$	$b=20.0$ $a=1.0$	$b=20.0$ $a=2.0$	$b=20.0$ $a=5.0$	$b=20.0$ $a=10.0$	$b=20.0$ $a=20.0$
0	7.31 (−1)	1.33 (0)	2.17 (0)	3.38 (0)	4.22 (0)	4.88 (0)
0.01	7.13	1.30	2.10	3.25	4.01	4.56
0.02	6.96	1.27	2.04	3.12	3.81	4.28
0.05	6.50	1.18	1.88	2.79	3.30	3.59
0.1	5.86	1.05	1.65	2.36	2.68	2.81
0.2	4.86	8.63 (−1)	1.31	1.75	1.89	1.92
	*4.85	*8.62	*1.31	*1.74	*1.86	*1.89
0.5	*3.01	*5.18	*7.34	*8.63 (−1)	*8.79 (−1)	*8.82 (−1)
1.0	*1.50	*2.47	*3.21	*3.44	*3.45	*3.45
2.0	*4.28 (−2)	*6.51 (−2)	*7.56 (−2)	*7.69 (−2)	*7.68 (−2)	*7.68 (−2)
5.0	*1.35 (−3)	*1.75 (−3)	*1.80 (−3)	*1.80 (−3)	*1.80 (−3)	*1.80 (−3)
10.0	*5.79 (−6)	*6.51 (−6)	*6.53 (−6)	*6.53 (−6)	*6.53 (−6)	*6.53 (−6)

6. Examples

Comparison of the results in the above sections 4 and 5 is made in table 5 with similar results of Berger and Lamkin [1] for a water barrier of $\tau=4$ and $a=b=2$, using the compounding rule in section 3 for noncorner positions. Agreement is within 5 percent.

There exists little *experimental* information on flux fields from rectangular gamma-ray sources. However, an additional partial check on $q_0(a,b)$ was supplied by Auxier et al., [3] as shown by the circles, triangles, and squares in figure 7. The distributed source was represented by an array of matched ($\pm 5\%$) Co^{60} sources spaced 2 ft apart over a 24- by 32-ft rectangle. The detectors were pocket ionization chambers with an average response of 14.4 milliroentgens per hour at 1 ft from a 1-millicurie point Co^{60} source. This response calibration was made in a geometry such that the combined effects of backscattering from the ground, the buildup factor in air, and the exponential attenuation by air were roughly equivalent to these combined effects in the actual measurements. Thus, since the experimental data in figure 7 are related to a source strength of 1 millicurie per square foot, the dimensional factor $\sigma/4\pi$ in (10) may be identified as 14.4 milliroentgens per square foot, and we may multiply $q_0(a,b;\ \alpha,\beta)$ by this number for an *absolute* comparison. The curves in figure 7 represent $14.4 \cdot q(a,b;\ \alpha,\beta)$, and agree with the experimental data to within ± 10 percent despite neglect of attenuation and scattering effects.

TABLE 5. *Dose rate, in milliroentgens per hour per millicuries per square foot of source strength, at a number of positions* $\alpha=x/h$, $\beta=y/h$ *at distance* h *from a rectangular surface of relative dimensions* $w/h=2$, $l/h=2$ *separated from a plane source of 1-Mev photons by a layer of water of thickness* $\tau=4$

The numbers in parenthesis* are from table 1 of Berger and Lamkin [1].

β \ α	0	0.25	0.50	0.75	1.0
0	0.211 (.22)				
.25	.275 (.28)	0.361 (.37)			
.50	.323 (.33)	.425 (.44)	0.503 (.51)		
.75	.350 (.35)	.462 (.48)	.546 (.55)	0.593 (.60)	
1.0	.359 (.37)	.473 (.49)	.559 (.57)	.608 (.62)	0.624 (.63)

*Arithmetic error in the Berger-Lamkin result at $\alpha=0.25$, $\beta=0.25$ is here corrected.

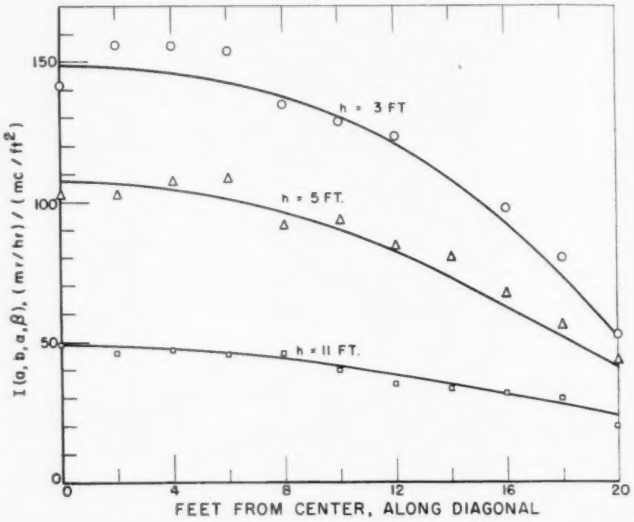

FIGURE 7. *Detector response in milliroentgens per hour at $h=3$, 5 and 11 ft above the diagonal of a rectangle of dimensions $w=24$ ft, $l=32$ ft covered with one millicurie per foot [2] of* Co^{60}. *The circles, triangles, and squares are experimental values of Auxier et al. [3] and the curves are results from (28) compounded according to (11).*

The authors thank M. J. Berger and L. V. Spencer for their interest, encouragement, and helpful criticism regarding this effort.

Appendix A. Evaluation of the p_l (a, b) Coefficients

The Legendre polynomials, $P_l(\cos\theta)$, may be written in the form [13]

$$P_l(\cos\theta)=\sum_{j=0}^{m}\frac{(-1)^j(2l-2j)!}{2^l j!(l-j)!(l-2j)!}(\cos\theta)^{l-2j}, \tag{34}$$

where $m=l/2$ if l is even, and $m=(l-1)/2$ if l is odd. Substituting (34) into (15) and using the notation

$$\binom{n}{r}=\frac{n!}{(n-r)!r!} \tag{35}$$

for the r'th coefficient of an n'th degree binomial expansion, we have for the *even* p_l's

$$p_{2l}=\sum_{j=0}^{l}\frac{(-1)^j}{2^{2l}}\binom{2l-j}{j}\binom{4l-2j}{2l-j}\int_{\alpha=0}^{a}\int_{\beta=0}^{b}\frac{d\alpha\,d\beta}{(\alpha^2+\beta^2+1)^{l-j+3/2}}. \tag{36}$$

Integration over α yields[14]

$$p_{2l}=\sum_{j=0}^{l}\sum_{i=0}^{l-j}\frac{(-1)^{i+j}}{2^{2l}(2i+1)}\binom{2l-j}{j}\binom{4l-2j}{2l-j}\binom{l-j}{i}a^{2i+1}\int_0^b\frac{d\beta}{(\beta^2+1)^{l-j+1}(a^2+\beta^2+1)^{i+\frac{1}{2}}}. \tag{37}$$

For $l=0$, integration over β, using eq (234.19a), reference [14], yields the result in (16). For the higher *even* terms, use of eq (234.18a) leads to (18) and higher terms which may be expressed in the general form

$$p_{2l}=\frac{1}{l(2l+1)\,2^{2l}}\frac{ab}{\sqrt{a^2+b^2+1}}\sum_{k=0}^{l-1}\frac{(-1)^{l-k-1}\,2^{2k}\binom{2l+2k}{l+k}\binom{l+k}{l-k-1}}{\binom{2k}{k}(2k+1)}$$

$$\times(2l+2k+1)\sum_{j=0}^{k}\frac{\binom{2j}{j}}{2^{2j}}\frac{1}{(a^2+b^2+1)^j}\left(\frac{1}{(a^2+1)^{k-j+1}}+\frac{1}{(b^2+1)^{k-j+1}}\right). \tag{38}$$

The *odd* p_l's as obtained from (15) and (34) may be expressed as

$$p_{2l+1}=\sum_{j=0}^{l}\frac{(-1)^j}{2^{2l+1}}\binom{2l+1-j}{j}\binom{4l+2-2j}{2l+1-j}\int_{\alpha=0}^{a}\int_{\beta=0}^{b}\frac{d\alpha\,d\beta}{(\alpha^2+\beta^2+1)^{l-j+2}}. \tag{39}$$

Integration over α yields (see ref. 14 eqs 15, 15a, b)

$$p_{2l+1}=\frac{1}{2^{2l+2}}\sum_{j=0}^{l}(-1)^j\binom{2l+1-j}{j}\binom{4l+2-2j}{2l+1-j}\binom{2l-2j+1}{l-j}$$

$$\times\left[\frac{1}{2^{3l-3j}}\int_{\beta=0}^{b}\frac{\tan^{-1}\left(a/\sqrt{\beta^2+1}\right)d\beta}{(\beta^2+1)^{l-j+3/2}}\right.$$

$$\left.+a\sum_{i=0}^{l-j}\frac{1}{2^{2i}\binom{2l-2j-2i+1}{l-j-i}(l-j-i+1)}\int_{\beta=0}^{b}\frac{d\beta}{(\beta^2+1)^{i+1}\,(a^2+\beta^2+1)^{l-j-i+1}}\right]. \tag{40}$$

The integral containing the arctangent was amenable to integration by parts, and the purely algebraic integrand was reduced to terms of standard form by successive application of the identity

$$\frac{1}{(\beta^2+1)\,(a^2+\beta^2+1)}=\frac{1}{a^2}\left(\frac{1}{\beta^2+1}-\frac{1}{a^2+\beta^2+1}\right), \tag{41}$$

leading to the general form for the odd terms, including (17) and (19),

$$p_{2l+1}=\frac{1}{2^{2l+1}(2l+1)}\sum_{k=0}^{l}\frac{(-1)^{l+k}}{2^{2k}}\binom{l}{k}\binom{l+k+1}{k}\binom{2l+2k+1}{l+k}$$

$$\times\left\{\frac{1}{(b^2+1)^k}\frac{b}{\sqrt{b^2+1}}\tan^{-1}\frac{a}{\sqrt{b^2+1}}+\frac{1}{(a^2+1)^k}\frac{a}{\sqrt{a^2+1}}\tan^{-1}\frac{b}{\sqrt{a^2+1}}\right.$$

$$\left.+ab\sum_{j=1}^{k}\frac{2^{2j-1}}{j\binom{2j}{j}}\cdot\frac{1}{(a^2+b^2+1)^j}\left(\frac{1}{(a^2+1)^{k-j+1}}+\frac{1}{(b^2+1)^{k-j+1}}\right)\right\}. \tag{42}$$

Appendix B. Evaluation of the q_n (a, b) Coefficients

The integral (27) may be written in cartesian coordinates as

$$I^o(\tau,a,b)=\frac{\sigma}{4\pi}\int_0^a d\alpha\int_0^b d\beta\,\exp\,(-\tau\sqrt{\alpha^2+\beta^2+1})/(\alpha^2+\beta^2+1). \tag{43}$$

The substitution

$$\alpha=\sqrt{\beta^2+1}\,\tan\,\eta \tag{44}$$

yields

$$I^o(\tau,a,b)=\frac{\sigma}{4\pi}\int_0^b\frac{d\beta}{\sqrt{\beta^2+1}}\int_0^{\tan^{-1}\frac{a}{\sqrt{\beta^2+1}}}\exp\,(-\tau\sqrt{\beta^2+1}\,\sec\,\eta)d\eta. \tag{45}$$

Expanding the exponential as a power series of its argument we have

$$I^o(\tau,a,b)=\frac{\sigma}{4\pi}\int_0^b\frac{d\beta}{\sqrt{\beta^2+1}}\int_0^{\tan^{-1}\frac{a}{\sqrt{\beta^2+1}}}\left\{\sum_{n=0}^{\infty}\frac{1}{n!}\,(-\tau\sqrt{\beta^2+1}\,\sec\,\eta)^n\right\}d\eta. \tag{46}$$

The first integration is then simply over powers of sec η, which can be found in integral tables as standard forms [15], giving

$$I^o(\tau,a,b)=\frac{\sigma}{4\pi}\int_0^b\left\{\frac{1}{\sqrt{\beta^2+1}}\,\tan^{-1}\frac{a}{\sqrt{\beta^2+1}}-\tau\,\sinh^{-1}\frac{a}{\sqrt{\beta^2+1}}\right.$$

$$\left.+\frac{\tau^2}{2!}\,a-\frac{\tau^3}{3!}\left[a\,\frac{\sqrt{a^2+\beta+1}}{2}+\frac{\sqrt{\beta^2+1}}{2}\,\sinh^{-1}\frac{a}{\sqrt{\beta^2+1}}\right]+\frac{\tau^4}{4!}\left[\frac{a^3}{3}+a(\beta^2+1)\right]-\ldots.\right\}d\beta. \tag{47}$$

Integration term by term over β then yields a power series in τ of the desired form (10), in which the coefficients $q_n(a,b)$ are

$$q_0(a,b)=\int_0^b\frac{1}{\sqrt{\beta^2+1}}\,\tan^{-1}\frac{a}{\sqrt{\beta^2+1}}\,d\beta, \tag{48}$$

$$q_1(a,b)=-\int_0^b\sinh^{-1}\frac{a}{\sqrt{\beta^2+1}}\,d\beta, \tag{49}$$

$$q_2(a,b)=\frac{a}{2!}\int_0^b d\beta,\ \text{etc.}, \tag{50}$$

as evaluated using (47).

No success was had in evaluating $q_0(a,b)$ in closed form. However, use of the arctangent expansion [16]

$$x\,\tan^{-1}x=\sum_{m=0}^{\infty}\frac{2^{2m}(m!)^2}{(2m+1)!}\left(\frac{x^2}{1+x^2}\right)^{m+1} \tag{51}$$

yields the series of integrable terms

$$q_0(a,b)=\frac{1}{a}\int_0^b\sum_{m=1}^{\infty}\frac{2^{2m}(m!)^2}{(2m+1)!}\left(\frac{a^2}{a^2+\beta^2+1}\right)^{m+1}d\beta. \tag{52}$$

Integration of these terms (see ref 15, p. 25) gives the result

$$q_0(a,b)=\tan^{-1}\frac{b}{\sqrt{a^2+1}}\cdot\frac{\sqrt{a^2+1}}{a}\sum_{i=0}^{\infty}\frac{1}{2i+1}\left(\frac{a^2}{a^2+1}\right)^{i+1}$$

$$+\frac{b}{a}\sum_{i=0}^{\infty}\frac{1}{2i+1}\left(\frac{a^2}{a^2+1}\right)^{i+1}\sum_{j=0}^{i-1}\frac{2^{2j}(j!)^2}{(2j+1)!}\left(\frac{a^2+1}{a^2+b^2+1}\right)^{j+1}. \tag{53}$$

in which the double summation vanishes for $i=0$. Since convergence of the summations in (53) is poor when both a and b are large as compared with unity, it is advantageous to rewrite the first member of the right-hand side, using the substitutions

$$\tan^{-1}\frac{b}{\sqrt{a^2+1}}=\frac{\pi}{2}-\tan^{-1}\frac{\sqrt{a^2+1}}{b} \tag{54}$$

and

$$\frac{\sqrt{a^2+1}}{a}\sum_{i=0}^{\infty}\frac{1}{2i+1}\left(\frac{a^2}{a^2+1}\right)^{i+1}=\tanh^{-1}\frac{a}{\sqrt{a^2+1}}=\sinh^{-1}a. \tag{55}$$

This gives

$$q_0(a,b)=\frac{\pi}{2}\sinh^{-1}a-\tan^{-1}\frac{\sqrt{a^2+1}}{b}\cdot\frac{\sqrt{a^2+1}}{a}\sum_{i=0}^{\infty}\frac{1}{2i+1}\left(\frac{a^2}{a^2+1}\right)^{i+1}$$
$$+\frac{b}{a}\sum_{i=0}^{\infty}\frac{1}{2i+1}\left(\frac{a^2}{a^2+1}\right)^{i+1}\sum_{j=0}^{i-1}\frac{2^{2j}(j!)^2}{(2j+1)!}\left(\frac{a^2+1}{a^2+b^2+1}\right)^{j+1} \tag{56}$$

which, after factoring the quantity

$$-\frac{b}{a}\sum_{i=0}^{\infty}\frac{1}{2i+1}\left(\frac{a^2}{a^2+1}\right)^{i+1}$$

from the last two members, may be identified with the result in eq (28). Now, since the inner summation over j in (28) consists of the leading terms of the expansion of $(\sqrt{a^2+1}/b)\times\tan^{-1}(\sqrt{a^2+1}/b)$ according to (51), the quantity within the braces in (28) is the *remainder* after $i-1$ terms of this expansion, causing the outer summation over i to converge very quickly for all values of a and b.

The remaining q_n (a,b) coefficients for n even and odd, respectively, may be written in the general forms

$$q_{2n}(a,b)=\frac{1}{(2n)!}\left\{(-1)^n\sum_{i=0}^{n-2}(-1)^i\binom{n-1}{i}(2i+2)!\,q_{2i+2}(a,b)+\sum_{i=0}^{n-1}\binom{n-1}{i}\frac{a^{2n-2i-1}b^{2i+1}}{(2n-2i-1)(2i+1)}\right\} \tag{57}$$

and

$$q_{2n+1}(a,b)=-\frac{1}{(2n+1)!}\left\{(2n-1)!\,\frac{2n-1}{2n+1}\left[-q_{2n-1}(a,b)\right]\right.$$
$$+\frac{2n!}{2^{2n}(n!)^2(2n+1)}\left[b(b^2+1)^n\sinh^{-1}\frac{a}{\sqrt{b^2+1}}+a(a^2+1)^n\sinh^{-1}\frac{b}{\sqrt{a^2+1}}\right.$$
$$\left.\left.+ab\sqrt{a^2+b^2+1}\sum_{i=0}^{n-1}\frac{2^{2i}(i!)^2}{(2i+1)!}(a^2+b^2+1)^i\{(a^2+1)^{n-i-1}+(b^2+1)^{n-i-1}\}\right]\right\} \tag{58}$$

from which $q_n(a,b)$'s for $1\leq n\leq 4$ are given in (29 to 32).

References

[1] M. J. Berger and J. C. Lamkin, Sample calculations of gamma-ray penetration into shelters: contributions of sky shine and roof contamination, J. Research NBS **60,** 109 (1958) RP2827.

[2] L. V. Spencer, Structure shielding against fallout radiation from nuclear weapons (to be published as an NBS Monograph).

[3] J. A. Auxier, J. O. Buchanan, C. Eisenhauer, and H. E. Menker, Experimental evaluation of the radiation protection afforded by residential structures against distributed sources, CEX 58.1, ORNL (Jan. 19, 1959).

[4] U. Fano, L. V., Spencer, and M. J. Berger, Penetration and diffusion of X-rays, Encyclopedia of Physics (Springer-Verlag, **38** II, 1959).
[5] R. A. Herman, A treatise on geometrical optics, p. 210 (Cambridge Univ. Press, London, 1900).
[6] Z. Yamanouti, Geometrical calculation of illumination due to light from luminous sources of simple forms. Researches Electrotech. Lab. (Tokyo) No. 148 (1924).
[7] P. Moon and D. E. Spencer, Light distribution from rectangular sources, J. Franklin Inst. **241,** 195 (1946).
[8] A. I. Mahan and W. F. Malmborg, Radiation characteristics of semicircular, circular and rectangular surface sources, J. Optical Soc. Amer. **44,** 644 (1954).
[9] O. Seiber, Die Wärmeaufnahme der bestrahlten Kesselheizfläche, Arch. Wärmwirtsch. **9,** 180 (1928).
[10] See, for example, W. B. Boast, Illuminating engineering, 1st ed., p. 89 (McGraw-Hill Book Co., New York, N.Y., 1942).
[11] G. Placzek, The function $E_n(x)=\int_1^\infty e^{-xu}u^{-n}du$, MT–1, NRC No. 1547, Chalk River, Ont. (1946).
[12] D. G. Andrews, Gamma ray shielding for engineers, U.K.A.E.A., Report Risley 5225 (Sept. 1954).
[13] R. V. Churchill, Fourier series and boundary value problems, 1st ed., p. 177 (McGraw-Hill Book Co., New York, N.Y., 1941).
[14] W. Gröbner and N. Hofreiter, Integraltafel I, Eqn. 234.17b. (Unbestimmte Integrale), (Springer-Verlag, 1957).
[15] H. B. Dwight, Tables of Integrals and Other Mathematical Data, 3d ed., p. 97 (McGraw-Hill Book Co., New York, N.Y., 1957).
[16] E. P. Adams and R. L. Hippisley, Smithsonian mathematical formulae and tables of elliptic functions, p. 122 (Smithsonian Institution, Washington, D.C., 1922).

Washington, D. C. (Paper 64C2–32)

JOURNAL OF RESEARCH of the National Bureau of Standards—C. Engineering and Instrumentation
Vol. 64C, No. 2, April–June 1960

Microwave Attenuation Measurements With Accuracies From 0.0001 to 0.06 Decibel Over a Range of 0.01 to 50 Decibels

G. F. Engen and R. W. Beatty

(January 15, 1960)

The application of certain power stabilization and measurement techniques to the problem of attenuation measurement has yielded a measurement system with a stability and resolution of the order of 0.0001 decibel. A practical application for this technique was recently provided in the calibration of a rotary vane type of variable microwave attenuator.

In order to take complete advantage of this increased stability it was necessary to apply refined techniques to the evaluation and reduction of mismatch error.

This proved to be by far the most exacting practical application of the cited techniques encountered to date, but the results of this calibration showed excellent agreement with the mathematically predicted values used in marking the attenuator dial.

1. Introduction

The following is a report on some recent work at the Radio Standards Laboratories of the National Bureau of Standards at Boulder, Colo. It is believed that this work represents perhaps the most accurate measurements of microwave attenuation yet made.

In the measurement of microwave attenuation, the stability or resolution of the associated measuring system places a limit on the accuracy with which small values of attentuation may be measured, because the reduction of other sources of error (such as mismatch) will tend to make the total error approach this value. In practice this limit has been typically of the order of ± 0.01 db.

The application of certain power stabilization [1] and measurement [2] techniques to the problem of attenuation measurement has yielded a measurement system with a nominal hundredfold increase in resolution and stability. A practical application for demonstrating the capabilities of this technique was recently provided in the calibration of a rotary vane type of variable microwave attenuator which is characterized, in part, by a high degree of resolution for small values of attenuation. Thus when a recent application called for this characteristic in a variable attenuator, and when a preliminary study of the mismatch and stability characteristics of an attenuator of this type indicated that such a step was warranted, it proved desirable to experimentally confirm the mathematically predicted values of attenuation which were engraved on the attenuator dial. This proved to be by far the most exacting practical application of the cited techniques encountered to date.

In order to take complete advantage of the improved stability, refined techniques were applied to the evaluation and reduction of the mismatch error. The capability of the system is indicated by the tabulated results of the attenuation calibration, and the estimate of the limits of error is supported by an analytic and experimental treatment.

---

[1] Glenn F. Engen, Amplitude stabilization of a microwave signal source, IRE Trans. on Microwave Theory & Tech. **MTT-6,** No. 2, 202–206 (Apr. 1958).

[2] Glenn F. Engen, A self-balancing direct-current bridge for accurate bolometric power measurements, J. Research NBS **59,** No. 2, 101–105 (Aug. 1957) RP2776.

2. The Calibration System

A simplified diagram of the calibration system is shown in figure 1. The attenuator under test is placed between an amplitude stabilized microwave signal source [1] and a bolometer mount and power meter. The power meter consists of a self-balancing d-c bolometer bridge [2] with provisions for measuring and recording the d-c bias power required to maintain the bolometer at its operating resistance of 200 ohms. The two bolometer mounts M_1 and M_2 shown in the temperature stabilized water bath are for power measurement and signal source stabilization, respectively. A reasonable amount of care was exercised to obtain good performance from each item of equipment, with a resultant system performance as shown in figures 2a and 2b. Figure 2a shows the stability and repeatability with the attenuator alternately set at the 0.00- and 0.01-db positions. It will be noted that the stability and repeatability are better than 0.0001 db (10 microbels). A recording of the long term system stability is given in figure 2b where the maximum variation is of the order of ± 10 microbels.

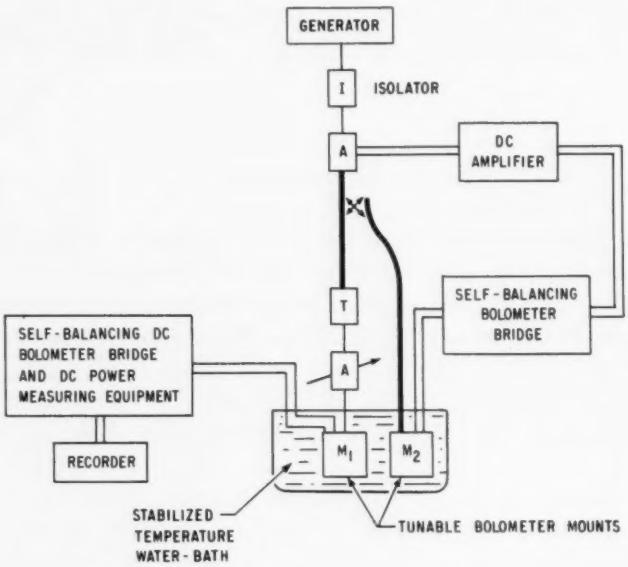

FIGURE 1. *Simplified diagram of calibration system.*

The absolute accuracy of measurement of small changes in d-c power at this level is estimated to be of the order of 0.02 μw. This indicates that further improvement could be expected in the results if the system stability could be improved in some manner, perhaps by use of a frequency-stabilized signal source.

3. Theory of Measurement

One could make an attenuation measurement by measuring the microwave powers P_1 and P_2 absorbed by the bolometer mount M_1 when the attenuator is set first on zero, then to some other setting. The relative attenuation A at this setting is

$$A=10 \log_{10} \frac{P_1}{P_2}. \tag{1}$$

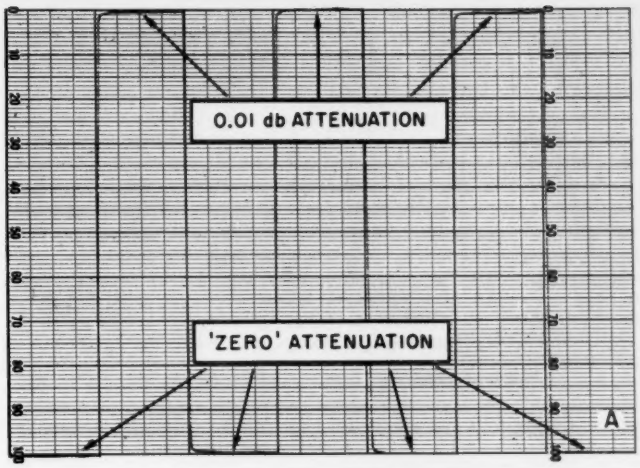

FIGURE 2a. System response to a 0. 01 db change in attenuation.

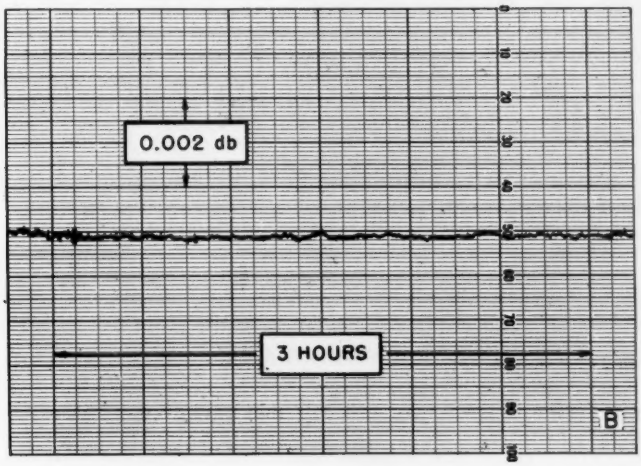

FIGURE 2b. Long-term system stability.

In making such a measurement, one assumes that the microwave power P absorbed by the bolometer element is proportional[3] to the d-c power W withdrawn in order to keep the bolometer resistance constant. Letting W_0 represent the d-c power required to bias the bolometer at its operating resistance when P equals zero,

$$A=10 \log_{10} \frac{W_0-W_1}{W_0-W_2}, \tag{2}$$

where W_1 and W_2 are the d-c bias powers corresponding to P_1 and P_2. (For the bolometer used, $W_0 \approx 15$mw and $P_1 \approx 10$mw.)

The apparatus employed permitted direct measurements of differences in d-c power, a procedure permitting greater accuracy and convenience than calculation of differences from separate measurements. The changes in d-c power level during an attenuation measurement are shown in figure 3.

[3] The constant of proportionality is determined by the substitution error of the bolometer which is known from other experimental data to be independent of power level.

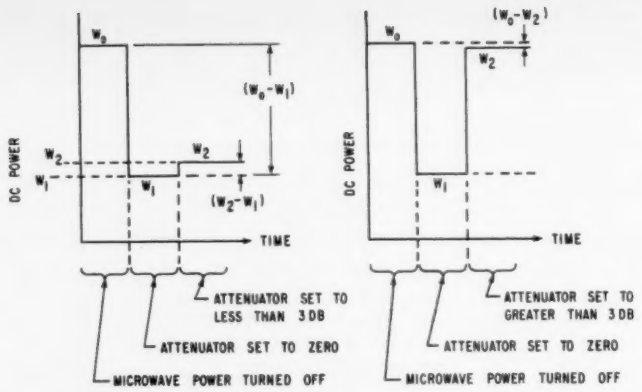
DC POWER
TIME
ATTENUATOR SET TO LESS THAN 3 DB
ATTENUATOR SET TO ZERO
MICROWAVE POWER TURNED OFF
ATTENUATOR SET TO GREATER THAN 3 DB

FIGURE 3. *Changes in d-c power level during an attenuation measurement.*

For attenuations less than approximately 3 db, the power difference W_2-W_1 was measured directly. If we let $W_{21}=W_2-W_1$, and $W_{01}=W_0-W_1$, eq (2) may be written

$$A=10\log_{10}\left(\frac{1}{1-\frac{W_{21}}{W_{01}}}\right). \tag{3}$$

For attenuations greater than approximately 3 db, the power difference W_0-W_2 or W_{02} was measured directly. Equation (2) becomes

$$A=10\log_{10}\frac{W_{01}}{W_{02}}. \tag{4}$$

4. Propagation of Error in Measuring D-C Power Differences

It is estimated that the error in measuring d-c power differences is within 0.1 percent $+0.1$ μw. When W_2-W_1 is measured, it can be shown that the limit of error in determining the attenuation is

$$\epsilon=10\log_{10}\left[\frac{1}{1-\frac{1}{1-\frac{W_{21}}{W_{01}}}\left(\frac{0.1\mu\text{w}}{W_{01}}+0.001\frac{W_{21}}{W_{01}}\right)}\right] \tag{5}$$

and when W_2-W_0 is measured,

$$\epsilon=10\log_{10}\left[\frac{1}{1-\frac{0.1\mu\text{w}+0.001\,W_{02}}{W_{02}}}\right]. \tag{6}$$

The calculated limits of error are shown in figure 4.

5. Mismatch Errors

The mismatch error[4] in calibrating a variable attenuator depends upon the reflections from the system in which the attenuator is placed and upon the changes in characteristics of the attenuator as its dial is moved from the reference position. The graph of figure 4 shows calculated

[4] R. W. Beatty, Mismatch errors in the measurement of ultrahigh-frequency and microwave variable attenuators, J. Research NBS **52**, No. 1, 7-9 (1954) RP2465.

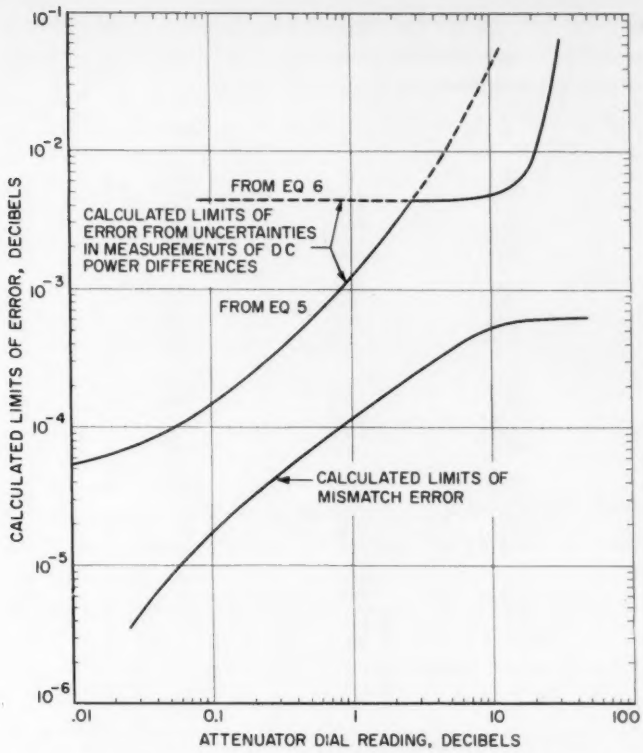

FIGURE 4. Limits of error as a function of attenuation.

limits of error [5] for the attenuator used, based upon measurements of the magnitude of the changes in the scattering coefficients S_{11} and S_{22} of the attenuator. It was assumed that there was no phase change in S_{21}. The mismatch error is below 0.0001 db for attenuator settings up to 0.1 db, and remains below 0.001 db for higher settings.

6. Results

The calibration data taken at 9.3897 kMc is shown in table 1. Three sets of data are shown in order to give an idea of the resettability of the attenuator, and more significant figures are given than one can normally use when interpolating between the marked dial divisions. It should be noted that the calibration is not necessarily representative of this type of attenuator, because only one such attenuator was calibrated by this procedure, and this was done at only one frequency. It should also be noted that this type of calibration is not available on a routine basis, because there are as yet no commercially available attenuators which can be read and are repeatable to 0.0001 db.

The estimated limit of error for the complete range of the attenuator, as determined from figure 4, is also shown in table 1. Above 20 db, the calibration was made in two parts: Measurement of the 20 db step, and measurement of the additional attenuation referred to this step. For these values, the quoted limit of error is the sum of the errors in the individual steps. The accuracy of setting the attenuator dial on the marks is not as good as the accuracy of the measurements.

It is noted that at the low end, the estimated accuracy of the measurement is also better than the repeatability of setting the attenuator on the mark. One concludes that further improvements in attenuators need to be made if we are to take full advantage of the most accurate measurement techniques.

[5] See appendix.

TABLE 1. *Results of three sets of measurements and calculated errors in single measurements*

Attenuator dial reading	Measured attenuations corresponding to dial reading				Maximum deviation from average	Calculated limit of error in single measurements
	1	2	3	Avg		
db	*db*	*db*	*db*	*db*	*db*	*db*
0.01	0.01077	0.01083	0.01044	0.0107	0.0003	0.000055
.02	.02123	.02145	.02145	.0214	.0002	.000068
.03	.03015	.03035	.03038	.0303	.0001	.000080
.04	.04043	.04088	.04074	.0407	.0003	.000091
.05	.05181	.05216	.05226	.0521	.0003	.00010
.06	.06102	.06067	.06086	.0609	.0002	.00011
.07	.06992	.07027	.06985	.0700	.0003	.00013
.08	.07991	.08056	.08017	.0802	.0004	.00014
.09	.09075	.09104	.09078	.0909	.0001	.00015
.1	.10226	.10203	.10210	.1021	.0002	.00016
.12	.11886	.11884	.11951	.1191	.0004	.00019
.14	.13681	.13760	.13819	.1375	.0007	.00021
.16	.15737	.15765	.15703	.1573	.0003	.00024
.18	.17806	.17792	.17888	.1783	.0006	.00026
.2	.20071	.20089	.20041	.2007	.0003	.00029
.25	.24702	.24709	.24724	.2471	.0001	.00035
.5	.49799	.49762	.49795	.4979	.0003	.00065
1	1.0037	1.0037	1.0037	1.004	.0000	.0013
2	1.9954	1.9972	1.9948	1.996	.0010	.0029
3	2.9968	2.9975	2.9993	2.998	.0015	.0047
5	4.9841	4.9923	4.9927	4.990	.006	.0048
10	9.9624	9.9671	9.9647	9.965	.003	.0053
15	14.991	14.988	15.001	14.99	.000	.0063
20	19.963	19.956	19.945	19.95	.01	.0093
25	24.999	25.031	24.987	25.01	.02	.014
30	30.080	30.049	30.074	30.07	.02	.015
40	40.354	40.281	40.367	40.33	.05	.02
50	52.338	52.041	52.336	52.24	.20	.06

7. Appendix

The analysis (see footnote 4) of mismatch errors in the calibration of variable attenuators yielded an equation for the error in terms of the scattering coefficients of two fourpoles corresponding to two settings of the attenuator dial, and the reflection coefficients of the system in which the attenuator was inserted. The measurement of all these quantities may be tedious or difficult, and an approximate method has been developed. One obtains reasonably close limits within which the error lies from a fairly simple experimental procedure.

The complete expression for the mismatch error is

$$\epsilon = 20 \log_{10} \left| \frac{(1-S'_{11}\Gamma_G)(1-S'_{22}\Gamma_L)-(S'_{21})^2\Gamma_G\Gamma_L}{(1-S_{11}\Gamma_G)(1-S_{22}\Gamma_L)-(S_{21})^2\Gamma_G\Gamma_L} \right|, \tag{1a}$$

where scattering coefficients are denoted by S_{mn}, and Γ_G, Γ_L represent, respectively, the reflection coefficients of the system "looking towards" the generator and load. Primes are used to designate a setting of the attenuator other than the zero or reference setting.

For small reflections, the following expression is derived from (1a):

$$\epsilon \approx 20 \log_{10} |1-(S_{11}-S_{11})\Gamma_G-(S'_{22}-S_{22})\Gamma_L+[S'_{11}S'_{22}-S_{11}S_{22}-(S'_{21})^2+S_{21}{}^2]\Gamma_G\Gamma_L|. \tag{2a}$$

If the attenuator VSWR is small, the products $S'_{11}S'_{22}$ and $S_{11}S_{22}$ may be neglected. Then (2a) becomes

$$\epsilon \approx 20 \log_{10} |1+(S_{11}-S'_{11})\Gamma_G+(S_{22}-S'_{22})\Gamma_L+[S_{21}{}^2-(S'_{21})^2]\Gamma_G\Gamma_L|. \tag{3a}$$

It is convenient to determine the magnitudes of the individual terms but not their phases, so that the limit of error, allowing random phase variations in S_{11} and S_{22}, but none in S_{21} is

$$\epsilon \approx 20 \log_{10} [1+|S'_{11}-S_{11}|\,|\Gamma_G|+|S'_{22}-S_{22}|\,|\Gamma_L|+(|S_{21}|^2-|S'_{21}|^2)\,|\Gamma_G\Gamma_L|]. \tag{4a}$$

The quantity $|S_{11}-S'_{11}|$ is determined as follows. With the attenuator under test connected as shown in figure 5, and set to its zero or reference position, tuner A is adjusted for a detector null, and tuner B is then adjusted until the reflection coefficient Γ_{2i} of the equivalent generator at terminal plane 2 vanishes. (This condition may be recognized by means of an auxiliary reflectometer.)

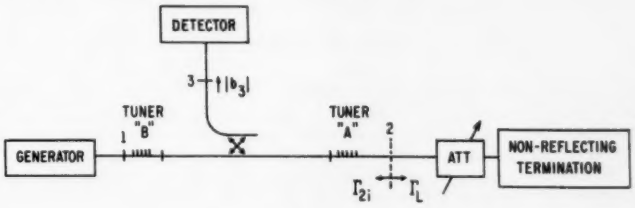

FIGURE 5. *Schematic of system for measuring* $|S_{11}-S'_{11}|$.

Movement of the attenuator dial to some other setting will then give an observable detector output. Using the theory[6] of a directional coupler with auxiliary tuners, one can obtain $|S_{11}-S'_{11}|$ in the following way.

The amplitude of the output power from the sidearm of the directional coupler in figure 5 has the magnitude $|b_3|=k\left|\frac{1+K\Gamma_L}{1-\Gamma_{2i}\Gamma_L}\right|$, where k is a constant for a given stable generator operating level.

With the attenuator set first on zero, $\Gamma_L=S_{11}$. Adjusting tuner A for $|b_3|=0$ changes K so that $KS_{11}=-1$. Adjusting tuner B for $\Gamma_{2i}=0$ makes the dependence of $|b_3|$ on Γ_L take the simple form:

$$|b_3|=k\left|1-\frac{\Gamma_L}{S_{11}}\right|.$$

Suppose the attenuator dial is moved to a new position such that Γ_L now equals S'_{11}; then $|b_3|=k|1-\frac{S'_{11}}{S_{11}}|=\frac{k}{|S_{11}|}|S_{11}-S'_{11}|$. The factor $k/|S_{11}|$ is obtained by replacing the attenuator by a waveguide section containing a sliding short. Upon sliding the short, $|b_3|$ goes through small variations so that one may observe $|b_3|_{max}$ and $|b_3|_{min}$. It is easily shown that

$$\frac{k}{|S_{11}|}=\frac{1}{2}(|b_3|_{max}+|b_3|_{min}).$$

One can assume that $|b_3|_{max}=|b_3|_{min}$ and employ a fixed short circuit with negligible error if the VSWR corresponding to S_{11} is less than 1.15. It may be that this error is tolerable for higher VSWR's since it is not important to know $|S_{11}-S'_{11}|$ to great accuracy.

The quantity $|S_{22}-S'_{22}|$ is found in the same way as above with the attenuator turned end for end.

The authors acknowledge the assistance of James E. Gilbert and Morris E. Harvey in making the attenuation measurements and of Wilbur J. Anson and Ronald Ridge in matching the system and making measurements to evaluate the limits of mismatch error. G. E. Schafer read the manuscript and provided information on phase shifts in variable attenuators.

---

[6] R. W. Beatty and D. M. Kerns, Recently developed microwave impedance standards and methods of measurement, IRE Trans. on Instr., I-7, Nos. 3 & 4, 319-321 (Dec. 1958).

BOULDER, COLO. (Paper 64C2-33)

JOURNAL OF RESEARCH of the National Bureau of Standards—C. Engineering and Instrumentation
Vol. 64C, No. 2, April–June 1960

Effect of Oleophobic Films on Metal Fatigue

H. E. Frankel, J. A. Bennett, and W. L. Holshouser

(January 15, 1960)

The fatigue strengths of a low-alloy steel, a magnesium alloy, and a copper-beryllium alloy were increased by coating the specimens with certain polar organic compounds. Also the dispersion of the results was much less for coated specimens of these materials than for clean ones. Similar tests showed no effect with titanium or 6061 aluminum alloy, and only a slight improvement for 17–7 PH stainless steel.

The full beneficial effect of the coatings was found only with compounds having a carbon chain of at least twelve, and this effect was not significantly reduced when the coated specimens were tested in water. Organic solvents (benzene and xylene) had a deleterious effect on the fatigue life of materials that were improved by oleophobic coatings.

It is suggested that the effect of the coatings is principally due to their ability to present a barrier to water and oxygen molecules.

1. Introduction

It is well known that environment has an important effect on the fatigue strength of metals. Lehmann [1],[1] in 1926, showed that the fatigue strength of a metal was greatly influenced by various media surrounding the specimen. Gough and Sopwith [2, 3] presented evidence which indicated that even the mild corrosion involved when fatigue tests were run in air affected the results.

Additional work by Ferguson and Bouton [4] verified the findings of the earlier investigations. In more recent findings, Frankel and Bennett [5] showed that an oil film increased the fatigue life of quenched and tempered low-alloy steel.

Not all environments which exclude air are beneficial, however. Karpenko [6] and Karpenko and Karlashov [7] showed that certain surface active media such as light oil+2 percent of oleic acid or water+2 percent of isopentanol can cause a reduction in the fatigue strength of structural steel. A recent review by Gilbert [8] summarizes much of the published work on corrosion fatigue.

A study of the literature revealed that, in many studies of the effect of environment, the media used were complex mixtures, not suitable for mechanism studies, and the data were valid only for a specific set of conditions involving many variables. In an effort to obtain more basic information on the effect of surface reactions on the fatigue process, the National Aeronautics and Space Administration sponsored an investigation at the National Bureau of Standards. This paper contains a report on one phase of this investigation.

Zisman and his associates [9] at the Naval Research Laboratory have made extensive investigations of the phenomena occurring at liquid-solid interfaces. As a result of this work, they found that certain classes of polar organic compounds form films on metal surfaces that are unwetted by, or are oleophobic to, all but the lowest-boiling hydrocarbons and other nonpolar liquids. These films are also highly hydrophobic, and are known to be effective in preventing corrosion. It was thought important to determine the effect that they might have on fatigue.

[1] Figures in brackets indicate the literature references at the end of this paper.

2. Materials and Testing Procedure

Six alloys were selected for the investigation, as follows:

Material	*Condition*
SAE 4340 steel	Quenched, double tempered
Aluminum alloy 6061–T6	Solution treated and aged
Titanium (75–A)	Hot rolled
17–7 PH stainless	Annealed (condition A)
Copper –1.75% beryllium	Solution annealed
Magnesium (AZ63–H24)	Hot rolled

All of the tests were conducted on rotating-beam fatigue testing machines of the R. R. Moore type, which apply pure bending moments to the test section. The machines were operated at approximately 2,000 rpm to minimize overheating effects. The specimens were machined with a smooth test section in which the longitudinal radius of curvature was held constant at 3½ in.; the minimum diameter was 0.310 in. for magnesium and 0.250 in. for the other materials. The straight cylindrical shanks were held in collet-type chucks in the bearing boxes of the machines. After the specimens were rough machined, they were ground to size with a 7-in. diameter wheel, the plane of which was parallel to the length of the specimen. To avoid overheating the surface, very shallow cuts were used and the entire operation carefully controlled. The preparation of the specimens was completed by polishing in a longitudinal direction with 400 Aloxite paper in the automatic polishing device previously described [10].

For the tests with liquids in contact with the reduced section of the specimen, a short length of tight fitting polyethylene tubing was slipped over the cylindrical shanks. Prior to testing, the specimens were individually cleaned by agitation in three successive containers of high-purity benzene. The pieces of polyethylene tubing were cleaned in a similar manner; the specimens and tubing were kept in benzene until required for testing.

A test was run with the specimen under one of the following conditions: (1) Cleaned and dry, (2) coated with or immersed in an organic substance, or (3) immersed in water in either the clean condition or after coating with an oleophobic film. Whenever a liquid medium was used, an air bubble large enough to contact the specimen was deliberately left in the tube. The organic substances listed below were included in this study:

Name	*Formula*	*Type*
n-Hexadecane	$CH_3(CH_2)14\ CH_3$	Nonpolar
Xylene	$C_6H_4(CH_3)_2$	Do.
Benzene	C_6H_6	Do.
Octyl alcohol	$CH_3(CH_2)_6\ CH_2OH$	Oleophobic
Dodecyl alcohol	$CH_3(CH_2)_{11}\ OH$	Do.
Dodecylamine	$CH_3(CH_2)_{11}\ NH_2$	Do.
Octadecylamine	$CH_3(CH_2)_{17}\ NH_2$	Do.

As this investigation was primarily concerned with surface reactions caused by fluctuating stress, no studies were made of environments more corrosive than air and water, nor of the effects of time or speed of testing.

All of the results obtained in tests at constant stress amplitude are presented in table 1. The water and nonpolar liquids either had no significant effect or caused a decrease in fatigue life. The oleophobic films, however, caused a marked increase in fatigue life for three of the six materials investigated; namely, the steel, the magnesium alloy, and the copper-beryllium alloy. There was no significant difference in the results between specimens immersed in these substances or merely coated with them, and the results are not differentiated. The aluminum and titanium showed no effect of any of the environments, while the 17–7 PH stainless showed only slight effect.

Coating of the specimens with dodecyl alcohol and then testing them in a tapwater environment resulted in as much improvement as was found with specimens tested in air. It was also found that tapwater had very little, if any, influence on the fatigue properties of those materials not affected by the oleophobic films. Continuous application of xylene or benzene to specimens of the first three metals listed in table 1 resulted in the poorest fatigue behavior.

Figure 1 shows a comparison of the effect of reagents having different carbon chain lengths. Apparently a length of about 12 carbon atoms provides optimum conditions with little change in fatigue life beyond this number. It can also be seen that the type of polar group does not appear to be as important as the number of carbon atoms.

The data in table 1 and figure 1 indicated that the results for specimens coated with dodecyl alcohol, dodecylamine, and octadecylamine were sufficiently similar to permit grouping for better statistical analysis. This has been done in table 2 for four materials. There were not enough specimens of the other materials to justify such an analysis. In the materials that were affected by the oleophobic films, the dispersion of the data, as measured by the coefficient of variation, was much smaller for the coated specimens than for clean ones at the same stress amplitude.

TABLE 1. *Test results*

Material	Median life, 10^3 cycles									
	Stress amplitude	Clean	Coatings [a]							
			1	2	3	4	5	6	7	8	9
	1,000 psi										
4340 steel	95	181				86		417			432
	100	83	111	71	69	76	141	189	176	183	173
	115	28				25		40			37
Mg AZ–63	10	500		246		430		1,776	1,680	1,543	1,300
	12.5	51			20	31	187	410	315	293	367
	15	17						12			
Cu–1.75Be	45	258						1,195		1,450	1,320
	50	89	108	58	62	92	151	248	226	221	226
	60	21						21			
Ti–75A	55	989						896			
	75	13						14			
Al 6061–T6	30	326		310		317		350		307	
	37	49				59		63		58	
17–7 PH	100	114				114		169			
	115	52				55		67			

[a] 1. *n*-hexadecane
2. xylene
3. benzene
4. tapwater
5. octyl alcohol
6. dodecyl alcohol
7. dodecylamine
8. octadecylamine
9. dodecyl alcohol plus water

TABLE 2. *Evaluated results*

Material	Stress amplitude	Fatigue test					Coefficient of variation	
		Clean		Coated [b]				
		No. of specimens	Life,[a] No. of cycles	No. of specimens	Life,[a] No. of cycles	Percent improvement	Clean	Coated [b]
	1,000 psi							
4340	95	11	177×10^3	6	433×10^3	144	0.098	0.015
	100	7	87	6	180	107	.040	.014
	115	12	26.6	5	39	46.8	.079	.030
Mg AZ-63	10	7	477	7	1,524	242	.059	.022
	12.5	5	48	7	337	603	.110	.038
Cu-1.75Be	45	5	272	5	1,268	365	.063	.033
	50	5	89	7	231	159	.089	.019
Al 6061-T6	30	6	311	3	333	7	.032	.048
	37	10	50	6	54	8	.076	.072

[a] Antilog of the log mean.
[b] Coated with oleophobic substances having carbon chain lengths of 12 or greater.

The data for 4340 steel are presented graphically in figure 2, and it will be noted that the vertical difference between the S–N curves is nearly constant, as the improvement in fatigue life increases at low stresses. The approximate ranges of ± 1 standard deviation from the means are shown in this figure, emphasizing the small dispersion of results with coated specimens.

An attempt was made to determine the number of cycles at which cracking started in at least one test of each of the materials in the clean and coated conditions. This was done by measuring the vibration of the bearing boxes: there is a marked increase in vibration when cracking starts. These measurements showed that approximately 85 to 90 percent of the total life of the specimen had been expended prior to the initiation of cracks. Thus, it can be concluded that, with the specimens used in this investigation, the improvement obtained with oleophobic coatings was primarily a measure of their effect on the initiation of a fatigue crack.

Zisman and coworkers [11] characterize an oleophobic substance as a long chain, aliphatic molecule having a polar group at one end. A consequence of this structure is a strong tendency to form tightly packed monomolecular films on various substrates. It has been pointed out that these materials offer the same degree of protection to specimens immersed in water as to those in air. Those specimens, given no protection, had generally shorter fatigue lives when tested with their surfaces partially in water. Thus, it is reasonable to assume that at least some of the effect of the oleophobic materials is due to their ability to present a barrier to water and oxygen molecules.

Likewise, the reduction in dispersion of results from coated specimens may be due to the replacement of the variable laboratory atmosphere with a reproducible oleophobic film of the substance. Similar results were obtained by Liu and Corten [12] who reported a marked reduction in scatter when they coated their specimens with vaseline.

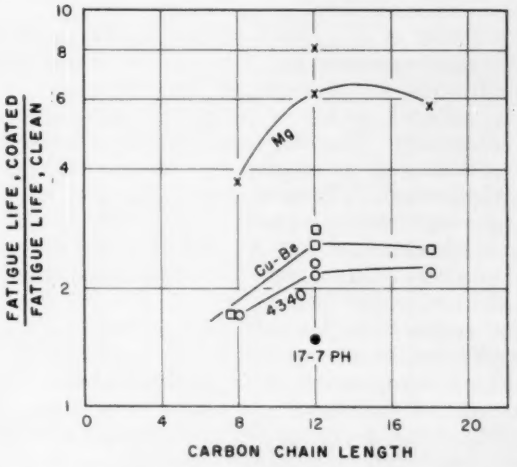

FIGURE 1. *Effect of oleophobic films on median fatigue life for four materials.*

The stress amplitudes in the tests were as follows: Mg (AZ-63)—12,500 psi, SAE 4340 steel—100,000 psi, Cu-1.75% Be—50,000 psi, and 17-7 PH stainless steel—100,000 psi. (For each material, the upper value at a chain length of 12 represents dodecyl alcohol, the lower one dodecylamine.)

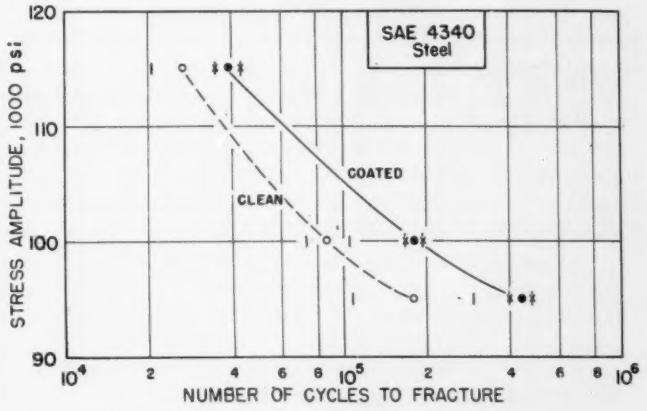

FIGURE 2. *Number of cycles to fracture as a function of the stress amplitude for SAE 4340 steel.*

Standard deviations at $\pm 1\,\sigma$ are also shown.

In contrast to the results with steel, Cu-Be alloy, and magnesium, the fatigue strengths of the 6061 aluminum and the titanium were not affected by coatings of the oleophobic substances used. The improvement with the 17–7 PH stainless, if any, was small. This suggests that the effects observed may be associated with the nature of the oxide film on the metals; the oxides on the unaffected alloys are known to be more adherent and less permeable than those of iron, copper, and magnesium.

On the basis of the limited data in table 1, it appears that the organic solvents xylene and benzene have a more deleterious effect on the fatigue strength than does water. This indicates that there are phenomena other than the reactions with water and oxygen that are important in the effect of environment on fatigue, but the exact nature of these phenomena cannot be determined without additional experiments.

3. Conclusions

This study of the effect of certain types of polar organic substances on the fatigue life characteristics of six different alloys revealed the following:

1. A general group of organic materials which form oleophobic films on metal surfaces were found to be effective in increasing the fatigue strengths of SAE 4340 steel, AZ–63 magnesium, and a copper 1.75 percent beryllium alloy. No effect was observed with titanium (75–A) and 6061-T6 aluminum alloy, and the effect on 17–7 PH stainless steel was questionable.

Conclusions 2 to 5 apply to results on the three alloys affected by the coatings.

2. Polar compounds with carbon chain lengths of 12 and 18 produced a greater improvement in fatigue life than a compound with a chain length of 8. As two different polar groups, amines and alcohols, showed the same improvement, it seems likely that the length of the carbon chain may be one of the controlling factors.

3. The dispersion of the data from the coated specimens was much smaller than that from the clean ones tested at the same stress amplitude.

4. The mean fatigue life of specimens with oleophobic films was the same whether they were tested in water or in air.

5. With the specimens used in this investigation, the fatigue life was governed primarily by the number of cycles to initiate a crack. Thus, the improvement obtained with oleophobic coatings was largely due to increase in the number of cycles to the initiation of a fatigue crack.

6. It is suggested that oleophobic films inhibit the impingement of extraneous molecules, such as water or oxygen, upon the surface. This reduces the rate of detrimental surface reactions that normally occur when specimens are stressed in air.

The authors thank Dr. J. Kruger, National Bureau of Standards and Dr. W. A. Zisman of the Naval Research Laboratory for their assistance and advice. The magnesium alloy was supplied by Mr. I. Feinberg of the Naval Ordnance Laboratory and the copper-beryllium metal through the courtesy of the Berylium Corporation, Reading, Pa.

4. References

[1] G. D. Lehmann, The variation in the fatigue strength of metals when tested in the presence of various liquids. Aeronautical Research Committee, R. and M. No. 1054 (1926).

[2] H. J. Gough and D. G. Sopwith, Atmospheric action as a factor in fatigue of metals, J. Inst. Metals **49,** 93 (1932).

[3] H. J. Gough and D. G. Sopwith, Some further experiments on atmospheric action in fatigue, J. Inst. Metals **56,** 55 (1935).

[4] L. Ferguson and G. M. Bouton, The effect of a coating of polybutene on the fatigue properties of lead alloys, symposium on stress corrosion cracking of metals, ASTM, STP No. 64, p. 473 (1944).

[5] H. E. Frankel and J. A. Bennett, Understressing as a means of eliminating the damaging effect of fatigue stressing, Proc. ASTM **55,** 891 (1955).

[6] G. Karpenko, Effect of the frequency of stress cycles upon the fatigue of steel in surface-active and in corrosive media, Doklady Akademii Nauk SSSR **87,** No. 5, 797 (1952).

[7] G. V. Karpenko and A. V. Karlashov, Effect of specimen dimensions upon adsorption fatigue and corrosion fatigue in steel, Doklady Akademii Nauk SSSR **92,** No. 3, 603 (1953).

[8] P. T. Gilbert, Corrosion fatigue, Met. Reviews **1,** 379 (1956.)

[9] E. G. Shafrin and W. A. Zisman, Hydrophobic monolayers adsorbed from aqueous solutions, J. Colloid Sci. **4,** 571 (1949).

[10] J. A. Bennett and J. G. Weinberg, Fatigue notch sensitivity of some aluminum alloys, J. Research NBS **52,** 235 (May 1954). RP2495.

[11] J. E. Brophy and W. A. Zisman, Surface chemical phenomena in lubrication, The fundamental aspects of lubrication, Ann. N.Y. Acad. Sci. **53,** Art. 4, 836. (June 1951).

[12] H. W. Liu and H. T. Corten, Fatigue damage during complex stress histories, Univ. of Illinois, T.A.M. Report No. 566, Submitted to National Aeronautics and Space Administration (Contract NAw–6524), (December 1958)

WASHINGTON, D.C. (Paper 64C2–34)

JOURNAL OF RESEARCH of the National Bureau of Standards—C. Engineering and Instrumentation
Vol. 64C, No. 2, April–June 1960

Ratio-Recording Spectroradiometer

Harry K. Hammond III, Warren L. Holford, and Milton L. Kuder

(January 26, 1960)

A ratio-recording spectroradiometer has been constructed primarily for determining the relative spectral irradiance from fluorescent lamps in the visible spectrum. Radiant flux from a test source and a comparison source is transmitted or reflected by separate diffusers. The irradiance from each diffuser is sampled alternately of the order of 100 times a second by a double prism monochromator with cam-linearized wavelength drive from 360 to 760 mμ. A 14-stage multiplier phototube with S–20 response is used with an electronic gate and integrator circuits to compare the spectral irradiances from the two sources. When the phototube outputs are unequal, a servo unit adjusts apertures in each beam to equalize them. The measured parameter is the amount of adjustment required for equalization at each wavelength. The apertures are adjusted by a cam coupled to a pen which records the ratio on a three-cycle logarithmic strip chart. The instrument requires about 8 minutes to record the spectrum at 10 mμ per inch. An expanded scale of 1 mμ per inch is used for evaluating the energy in the spectral lines. The speed of wavelength scan may be made inversely proportional to the unbalance signal, if desired, to provide ample time to record spectral lines accurately. Symmetry of beam treatment is demonstrated by interchanging test and comparison sources and recording the inverse ratio.

1. Introduction

In order to calibrate fluorescent lamp color standards on a sound physical basis, the relative spectral irradiance from the lamp should be determined. These data, when weighted by the response functions of the CIE standard observer, yield chromaticity coordinates directly. A spectroradiometer has been constructed at NBS for the measurement of relative spectral irradiance with particular regard to the problem of fluorescent-lamp measurement.

Spectrometers for dispersing light into its spectral components have been commercially available for a long time. However, a universal design has not been adopted for converting a spectrometer into a spectroradiometer because of the varied requirements of particular laboratories. A recording spectroradiometer was built by Zworykin in 1939 [1].[1] Ten years later, Studer and Jacobsen reported the design of a spectroradiometer which was available commercially for a time [2]. In 1957, however, no spectroradiometer was commercially available; so it became necessary to design one to meet our requirements.

2. Requirements

The general requirements of a spectroradiometer are simply stated. Radiant flux from a source must be dispersed into its spectral components and evaluated with a suitable detector and read-out device to provide relative spectral irradiance data. Accurate measurements require a high degree of spectral purity, but sufficient energy must be transmitted by the dispersing element for precise evaluation by the detector. A practical compromise between resolution and sensitivity is necessary, as very high resolution would permit only infinitesimal energy to be transmitted to the detector. The instrument response must be appropriate to record accurately the peaks of sharp spectral lines. It must be able also to average the light from a modulated source, such as a fluorescent lamp operated on alternating current.

For the purpose of evaluating fluorescent lamp chromaticity, a photometric accuracy of 1 percent is considered adequate. If the photometric errors are truly random, then the chromaticity coordinates computed from the spectral radiance data will be uncertain by much less than this amount.

3. Basic Components

Monochromator. Both prism and grating monochromators are available for dispersing light into a spectrum. Grating monochromators are attractive because the dispersion is almost constant over a practical range of wavelengths. This permits a direct connection to a linear wavelength scale and provides a pass band of constant spectral width for fixed mechanical slits. Gratings, however, have the disadvantages of overlapping orders, higher stray light, and possible ghosts. Stray radiant flux in any dispersion system is minimized by double dispersion. In a good double prism monochromator, the stray flux will be several orders of magnitude below the radiant flux in the pass band. After some investigation of monochromators available at a moderate price, a Carl Leiss double monochromator with dense flint glass prisms was selected. Dispersion data are

[1] Figures in brackets indicate the literature references at the end of this paper.

539889—60——5

shown in figure 1. The three bilateral slits have straight sides 10-mm long and are set independently. Data are taken with constant mechanical slits; hence the pass band is a function of wavelength. For measurement of fluorescent lamps, the entrance and exit slits are frequently set at 0.5 mm with the middle slit at 0.6 mm. For these conditions, the pass band at 546 mμ is just under 3 mμ when evaluated as the width of the mercury line at half height.

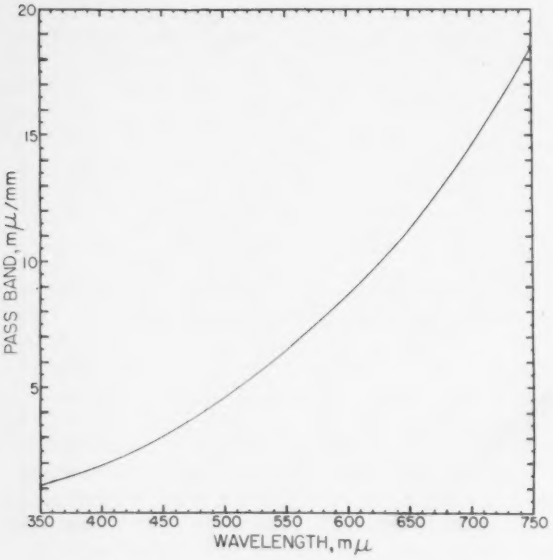

FIGURE 1. *Dispersion data for spectroradiometer.*
Carl Leiss double monochromator with dense flint glass prisms.

The original nonlinear prism drive, consisting of sector and worm, has been disengaged. The new drive consists of a system of levers including an 18-in. arm that follows a specially constructed cam with radii ranging from 3 to 7 in. The arm, cam, and associated gear train render the wavelength scale linear over the range 360 to 760 mμ.

Detector. The low level of radiant flux passing through the exit slit of the monochromator requires that a highly sensitive detector be employed. The detector should also provide good response over the entire range of spectrum to be measured. The equivalent noise input should be low to obtain a high signal-to-noise ratio for weak signals. The detector selected was a 14-stage multiplier phototube, RCA developmental type C7237, now designated as type 7265. This tube is an end-on type with S–20 response, peaking in sensitivity at approximately 420 mμ and maintaining 20 percent of the peak response at 700 mμ.

Recording System. Some spectroradiometers have been designed to use the output of the detector as the measured parameter. Instruments can be designed, however, that are essentially independent of the response characteristics of the phototube and the spectral transmittance of the monochromator. Considerations involved in this type of system have been published by Mitsuhashi in 1955 [3], and an instrument utilizing these principles was reported by MacAdam in 1953 [4] and described in detail in 1958 [5]. Our design was developed independently, but is similar in many respects to those cited above. Measurement is accomplished by rapidly comparing the flux from a standard source with that from a test source as the spectrum is scanned and optically attenuating the beams until the two have equal flux. For this system, the measured parameter is the setting of the beam attenuator. Attenuator settings are recorded on a strip chart, giving a plot of ratios of relative spectral irradiance from the two sources as a function of wavelength.

Attenuator System. There are two requirements that should be considered in the design of an attenuator system. The geometric distribution of flux incident on the entrance slit of the monochromator should not be appreciably affected by the attenuator, and the calibration of the system should not be a function of wavelength. The latter requirement cannot be met by optical wedges or polarizing filters. The former requirement cannot be met by a single adjustable aperture but for practical purposes is satisfied by an array of apertures. To compare precisely sources whose spectral irradiance ratios vary over a wide range, the aperture arrangement should be chosen so that the transmittance will be a rapidly changing function of displacement. Our basic attenuator design consists of an array of 25 square openings, 1/10 in. on a side, etched in metal foil, and arranged as shown in figure 2. Each attenuator consists of a pair of arrays, one fixed and one movable on an arc whose radius is about 4 in. The change in area of the openings, and therefore the transmittance, is proportional to the second power of the displacement of the movable array. When arranged so that the attenuator in one beam opens as the other closes, the transmittance ratio is a fourth-power function of the displacement drive, provided the flux through the attenuators is relatively uniform.

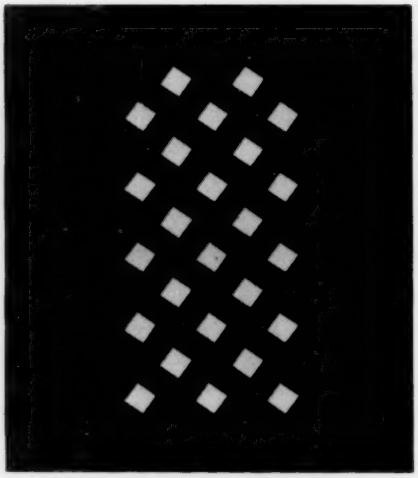

FIGURE 2. *Attenuator array.*

4. Entrant Beam Geometry

The entrant beam geometry is shown in figure 3. The rotating sector beam switch, consisting of a wheel with four sectors of alternate apertures and mirrors, alternately passes light from each source into the monochromator. The irradiance from each lamp may be sampled at a rate which is adjustable from 20 to 120 times a second. Compartments for filters are located in each beam for use when desired. The optical attenuators are located in each beam and operate in opposition, one opening while the other is closing. The two light sources are external to the instrument case and, therefore, can be easily changed.

The cone of rays at the entrance slit of the monochromator required to fill the collimating mirror was determined by rear projection of a source placed at the exit slit. To prevent the monochromator from giving a different weighting to rays from different sources, it is necessary that they both subtend the same solid angle at the entrance slit, or better, that they fill the maximum solid angle of the monochromator optics uniformly. To achieve this goal at some distance from the slit requires that the sources have either relatively large areas of uniform radiance or that they uniformly irradiate reflecting or transmitting diffusers of appropriate size.

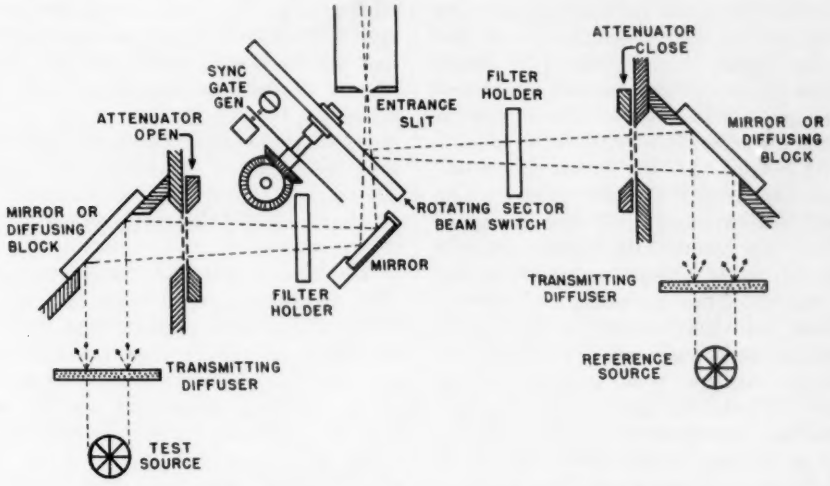

FIGURE 3. *Diagram of entrant beam geometry.*

5. Photometric Scale

In order to achieve the desired photometric scale on the strip chart, a precision linkage has been installed between the attenuators and the servo drive mechanism. The two movable elements of the attenuators are displaced simultaneously by two identical eccentric disks on a common shaft. The shaft extends to the strip chart recorder where it terminates in a cam-following lever. A relatively simple cam, driven by the recorder servomotor, converts the fourth power function to the desired logarithmic function. The location of cam and follower are shown in figure 4. The recorder plots the area ratio of the attenuators on a logarithmic scale. Cams may be interchanged by the removal of one thumb nut to provide different photometric scales. For fluorescent-lamp measurements, however, the cam consistently used provides a three-cycle log scale on the 10-in. width of the strip chart. The intense lines of the mercury spectrum are easily accommodated with this scale.

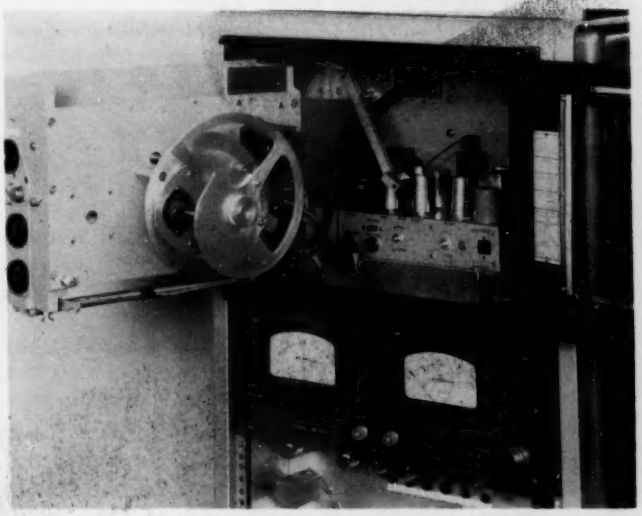

FIGURE 4. *Photometric cam provides 3-cycle log scale.*

6. Electronics

The dynode voltage supplied to the phototube is continuously adjusted automatically to maintain constant average anode current. This feature provides constant detector sensitivity as spectral irradiance from a source decreases, until a minimum photon level is reached and maximum gain is applied. This feature also prevents the phototube from giving erroneous balance indications due to anode current saturation caused by high gain at high flux levels. Phototube damage due to excessive gain at such levels is also prevented by this automatic voltage adjustment.

Signals from two sources are separately supplied to two integrating networks by electronic gates as shown in the block diagram of figure 5. The gating signals are generated by sets of auxiliary light sources and phototubes. One set is used for gating the test source signals, another for the signals from the reference source. An opaque disk on the beam switch motor shaft has precisely positioned apertures which produce the gating signals. The gate is opened after the test or reference flux falls on the detector and is closed before the flux is switched off. The gated signals are essentially square waves. The integrator circuit and subsequent filter are designed to provide a smooth direct-current signal to the conventional servoamplifier of the recorder. The integrating network has a time constant of about ½ sec. The integrator also serves to average signal variations due to modulated radiant flux from an a–c operated fluorescent lamp as well as noise pulses from the phototube. When the integrated signals from the two sources are unequal, the servo drives the attenuators until a balance is achieved.

The magnitude of the unbalance signal is also used to control the rate of wavelength scan. One motor drives the prisms and the recorder chart and thus wavelength correlation is maintained between the spectrum and the chart regardless of the scanning rate. The speed of the drive motor is modulated according to the magnitude of the unbalance signal. This modulation is roughly proportional to the reciprocal of the first derivative of the curve on the chart. When the curve is flat the rate of scan is maximum. As the slope of the curve begins to change the rate of scan is automatically reduced to prevent inaccurate recording imposed by phase lag in the servo response. This feature insures the faithful recording of the peaks of sharp spectral lines.

Tachometer generators are used in conjunction with both the wavelength drive and photometric balance motors. One generator provides motor speed information to the wavelength-scan speed-control unit. The other generator provides velocity damping for the balance motor.

The wavelength drive has been equipped with auxiliary gears and electric clutches to provide two chart scales, 1 mμ/in. or 10 mμ/in., merely by energizing the proper clutch. The expanded scale of 1 mμ/in. is most useful for evaluating the flux in spectral lines. When a modulated scanning rate is not desired, a manual switch provides for selection of one of two uniform scanning rates. With a chart scale of 10 mμ/in. the approximate times required to scan the visible spectrum at each speed are 8 min and 30 min.

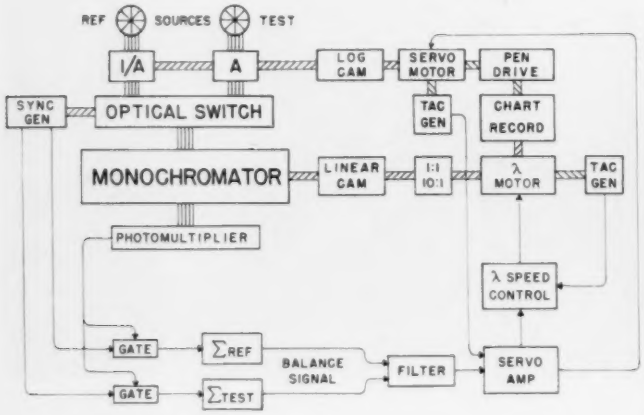

FIGURE 5. *Block diagram of instrument components.*

7. Meters and Controls

The front panel of the console is shown in figure 6. The wavelength motor shaft has been extended to the front of the instrument to permit convenient manual setting to any desired wavelength. Two dials are used, one reading hundreds and tens of millimicrons, the other reading units and tenths, so that wavelengths can be read easily to better than 0.1 mμ. Calibrations with spectral-line sources, however, show that the original cam has wavelength-scale errors of as much as 0.2 mμ below 580 mμ and somewhat larger errors at longer wavelengths.

FIGURE 6. *Mr. Holford records elecirical parameters while instrument records spectral irradiance of fluorescent lamp relative to an incandescent lamp.*

Photograph was made prior to use of external reflecting diffuser.

The channel balance meter in the lower left indicates the difference voltage between the test and reference signals. During operation, the difference voltage indications will be very small if the servo balance unit is operating properly.

The meter on the right indicates the dynode supply voltage to the phototube. Since the average anode current is held constant automatically, a lower flux level requires a higher dynode voltage. As the dynode voltage is raised to the maximum permissible value, the signal-to-noise ratio is lowered slightly. Further reduction in flux level results in a noisy signal and consequently produces an erratic recorder trace. Thus the dynode-voltage meter provides an indication of whether there is enough flux to permit a reliable ratio determination.

The meter at the upper left also provides indications proportional to the dynode voltage. This meter, however, is provided with zero suppression and sensitivity controls so as to provide an indication of the location of a spectral line when manually manipulating the wavelength knob during wavelength calibration.

Switches for controlling power, speed of scan, and wavelength scale are conveniently located on the front panel. Pushbuttons to provide fast travel of the wavelength drive in either the forward or backward direction are located near the wavelength dials. Potentiometers for setting electrical characteristics in the balance circuit and in the speed control unit to provide optimum instrument performance are located behind the panel below the two meters.

8. Calibration

During construction of the instrument, particular care was given to the design of the components whose calibration directly affected the instrumental accuracy. Mechanical linkages in the wavelength drive and photometric system were held to close tolerances and materials chosen were those least likely to wear or change with time. Several hundred hours of instrument operation have revealed no changes due to wear. Frequent wavelength calibrations using narrow slits of 0.15 mm reveal that wavelength scale calibration is reproducible to better than 0.1 mμ.

The photometric cam is calibrated by utilizing ratios of 2 to 1. Two lamps of equal intensity, as measured by the spectroradiometer, irradiate the diffuser at one entrance port. A reference lamp illuminating a diffuser at the second port is compared with each of these lamps in turn to assure their equality, and then compared with the sum of the two lamps. The resulting irradiance ratio is precisely 2. The wavelength drive is not operated during the photometric calibration. The three-cycle log chart is adequately covered by nine steps of ratios of 2 to 1. The intermediate calibration points are interpolated with data based on micrometric measurements of the cam radius. The reproducibility of photometric calibrations over the usable portion of the cam is about 0.3 percent.

9. Performance Tests

Tests have been made to evaluate the performance of the spectroradiometer. The investigation of possible systematic errors has been aided by the fact that the test lamp may be operated at either of the two entrance ports with the reference lamp at the other. Because photometric accuracy is determined by the geometric distribution of the radiant flux at the attenuators and the calibration of the photometric cam, the exchange of entrance ports produces reciprocal conditions which provide internal checks on instrument performance. A small discrepancy in fluorescent-lamp measurements was revealed when the reference and test sources were interchanged. This caused an investigation to be made of possible systematic errors or bias in the instrument. The electronic circuits for each channel were interchanged, but these circuits were not the cause of the biased results. The electronic system was further vindicated when practically identical spectral-irradiance data were recorded from a fluorescent lamp operating first on alternating current and then on direct current. A part of the small discrepancy was attributed to a bias in the servo unit. Equal, but opposite voltages to the servoamplifier did not produce equal torques at the servomotor because the voltages on the motor windings were not exactly 90° out of phase. The effect was noticeable only when the signals were relatively weak. A trimmer capacitor placed across one of the motor windings produced the required phase relationship for balanced operation of the servo motor.

Further investigation revealed that interchange of reference and test sources introduced no discrepancy when the test source geometry is similar to that of the calibration source. A fluorescent lamp, however, has a geometry quite different from that of the incandescent lamp standard. The discrepancy between results obtained by interchanging test and reference sources was traced to the nonuniform irradiation of the diffusing block placed at an angle of 45° to the axis of the fluorescent lamp. The nonuniform irradiance distribution from the incandescent standard was included in the calibration, but the entrance port acted as a field stop for the fluorescent lamp, thereby producing a different irradiance distribution.

In an attempt to eliminate this difficulty, the reflecting diffusers were replaced with mirrors, and ground-glass transmitting diffusers were mounted parallel to the axis of the fluorescent lamp. Ground glass, however, acts like a large number of tiny prisms and thus deviates shortwave energy more than longwave energy. This differential diffusion can be tolerated when comparing sources of the same size. When test and standard sources are different in size, as is the case with fluorescent and incandescent lamps, then different amounts of radiant flux are scattered out of the beam at each wavelength and erroneous values of relative spectral irradiance are obtained. Further consideration of the use of reflecting diffusers indicated that the problem of non-

uniform irradiance of the test diffuser could be solved by relocating it external to the instrument in such a position as to obtain uniform irradiance from the fluorescent lamp.

10. Modes of Operation and Applications

Accurate determination of the ratios of relative spectral irradiance from a test and a standard source by direct comparison requires similar treatment of each beam. Light from each source must traverse equivalent paths to prevent erroneous results caused by spectral selectivity of the system. No evidence of asymmetry has been discovered, but the majority of measurements have been made by using a substitution technique. In this technique a reference source is calibrated by operating the standard source on the test side. This procedure has the disadvantage of requiring periodic calibration of the reference source, but it has four advantages: (1) The standard and test beams travel the same paths; (2) the life of the standard lamp is conserved by operating it only to calibrate the reference source; (3) the reference source may be a low-wattage, short-life lamp which produces less heating of the air in the vicinity of the fluorescent lamp than does the usual 500-w projection lamp regularly supplied as a color-temperature standard; and (4) the spectral irradiance from the reference source can be modified by an uncalibrated filter. The use of a blue filter reduces the flux from the reference source at the red end of the spectrum, thereby keeping the flux ratio of fluorescent to reference lamp on scale. If a filter were not used, the ratio of flux of incandescent standard at 2854°K to reference source would plot as a horizontal line throughout the spectrum and the curve for fluorescent lamp "B" would be off the bottom of the scale beyond 700 mμ. See figure 7.

The spectroradiometer was built primarily for the measurement of fluorescent lamps. However, the instrument can measure the relative spectral irradiance from any source or source-filter combination that will provide a minimum illumination of about 1 fc on the diffuser. The transmittance of filters can be obtained by computing the ratio of relative spectral irradiance from the source-filter combination to that from the source alone. A "100 percent" curve is recorded as the irradiance ratio of two sources. If the sources are identical, the irradiance ratio will be constant throughout the spectrum, and the plot will be a line parallel to the wavelength axis. Transmittance data may be recorded by inserting the filter in either of the two beams. By measuring the filter in each beam and averaging the result, any inaccuracies in the photometric-cam calibration above and below the 100 percent curve will be averaged. Comparison of two filters may be made directly by inserting one in each beam.

Reflectance data for a specimen illuminated with any desired flux geometry may be obtained by computing the ratio of spectral radiance of the specimen

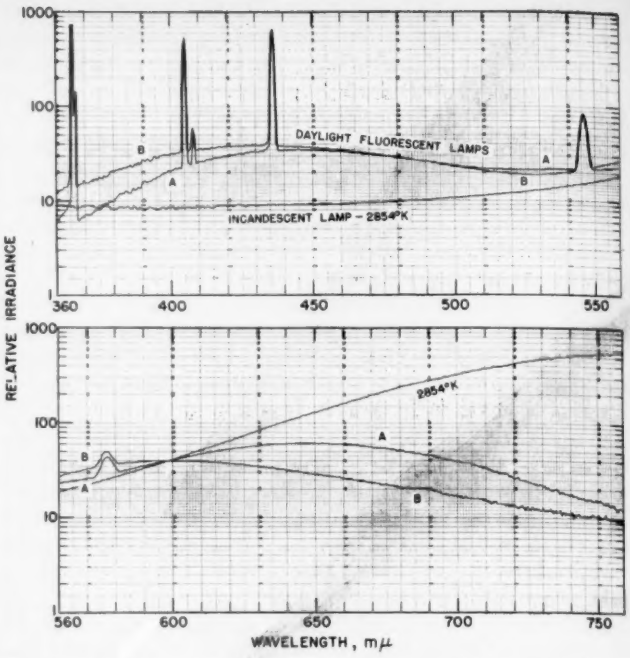

FIGURE 7. *Curves obtained for two daylight fluorescent lamps and an incandescent lamp at 2854° K.*

These curves are ratios of the irradiance from the test lamp to that from an incandescent reference lamp and Corning blue-green filter type 4308. Filter is used to limit irradiance-ratio range of lamps to two log-cycles. Daylight fluorescent lamps usually do not differ by as much as shown here. Curve A was obtained with an old lamp utilizing a discontinued beryllium phosphor. Curve B was obtained with a lamp from current production utilizing a phosphate phosphor. Low values of irradiance from both test and reference sources below 400 mμ and above 700 mμ cause the trace to be noisy.

to that of a standard diffuser. Luminescent or fluorescent materials can also be measured if they have several inches of uniform luminance and if the luminance is of the order of 1 fL.

The chart drive incorporates several flexible features. As previously mentioned, data may be recorded with wavelength scales of 10 mμ/in. or 1 mμ/in. The recorder chart can also be driven without advancing the wavelength so as to produce a record of the radiant flux of a spectrally homogeneous signal as a function of time.

Cams have been designed to provide 1 or 3 log cycles on the 10-in. strip chart. More precise data, however, may be obtained by reading directly two dial scales; one, a coarse scale, is on the pen-cable drum and the other, a fine scale, is on the servo motor shaft. The precision of photometric readings is approximately 0.1 percent on the dial scales.

11. Discussion

Spectral-irradiance data for a light source can be obtained relative to an incandescent lamp of known color temperature in relatively short time with good precision. Reduction of data from the chart record, however, is time consuming and in addition appears to be the weakest link in the chain of data precision. As indicated above, dial readings of servo motor balance positions have been used for calibration and on other occasions to provide readings of highest preci-

sion. Photometric calibrations can be made with a reproducibility of a few tenths of a percent, whereas chart readings are uncertain by about half a percent. Greater precision and increased speed of data reduction could be obtained by utilizing an electronic encoder to obtain decimal or binary digital readout on punched paper tape or other high precision recording means. Data in this form could then be supplied without transcription to a high-speed electronic computer to obtain chromaticity coordinates.

The authors express their thanks to Paul E. Allison for his contribution of skilled craftsmanship in the fabrication of mechanical parts for the instrument and to Jerome S. Laufer for his assistance in the selection of some of the components for the instrument.

12. References

[1] V. K. Zworykin, An automatic recording spectroradiometer for cathodoluminescent materials, J. Opt. Soc. Am. **29,** 84–91 (1939).
[2] F. J. Studer and W. R. Jacobsen, Spectroradiometry, Gen. Elec. Rev. **52,** No. 10, 34–9 (1949).
[3] H. Mitsuhashi, Some considerations of the balanced spectroradiometry, Sci. of Light **4,** 61–71 (1955).
[4] D. L. MacAdam, Automatic recording spectroradiometer, J. Opt. Soc. Am. **43,** 819A (1953).
[5] D. L. MacAdam, Continuously recording spectroradiometer, J. Opt. Soc. Am. **48,** 832–40 (1958).

Washington, D.C. (Paper 64C2–35)

JOURNAL OF RESEARCH of the National Bureau of Standards—C. Engineering and Instrumentation
Vol. 64C, No. 2, April–June 1960

An Intermittent-Action Camera With Absolute Time Calibration

G. Hefley, R. H. Doherty, and E. L. Berger

(January 12, 1960)

A detailed description is presented of a film-recording system in which a randomly occurring event and its absolute time are recorded simultaneously. The system consists of a 16-millimeter framing camera capable of intermittent operation at a maximum rate of 140 frames per second (fps) and a clock capable of reading out time with an absolute accuracy of plus or minus 1 millisecond (msec).

1. Introduction

The Central Radio Propagation Laboratory of the National Bureau of Standards, Boulder Laboratories, has developed a recording system which will simultaneously photograph randomly occurring events and the precise time of each event (fig. 1). The system employs a camera which has a minimum consumption of film but can complete a framing cycle in 7 msec. The timing system is capable of resolving time to within a few microseconds. When the standard time broadcasts of WWV are used to synchronize the system, the absolute accuracy is dependent upon the propagation variables of the WWV signal.

The high-framing rate of the camera results from the use of a unique clutch system between the film drive and a continuously revolving flywheel. The clutch actuation mechanism is similar to a large electrodynamic speaker. When a pulse is applied to a part corresponding to the voice coil, a cone is driven into engagement with the flywheel, thus rotating a small drum in contact with the film. The rotation of the drum pulls one frame of film past the lens opening. The peak power applied to the voice coil is approximately 35 kw. Power surges of this magnitude may be repeated at intervals of only a few milliseconds by utilizing 2 condenser reservoirs and 2 thyratrons in a series arrangement. An 88-microfarad (μf) condenser is discharged through the voice coil by one thyratron and after a short delay is recharged from a 1,600 μf reservoir by the other thyratron. Consequently, the power supply required to operate the system needs only to provide an average current sufficient to maintain the charge on the large condenser reservoir at the maximum duty cycle.

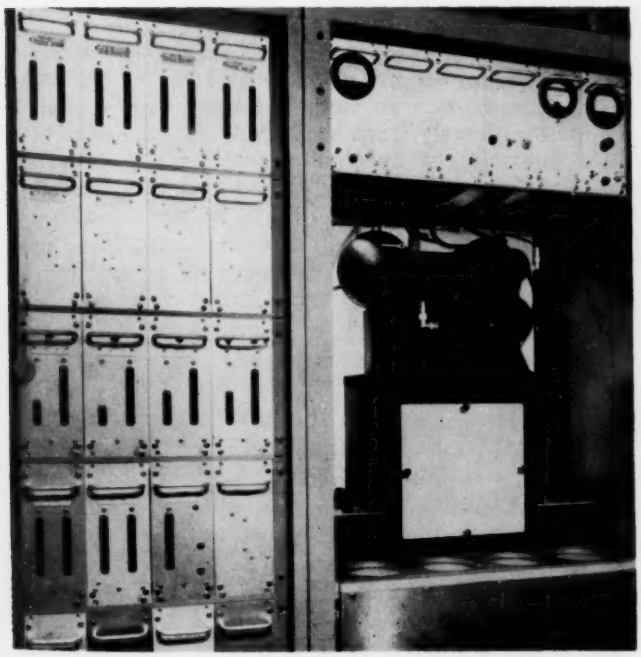

FIGURE 1. *Camera and timer.*

Studies of intermittent, randomly occurring events such as the electromagnetic radiation from lightning strokes require recording instruments of a special type. Because of the excessive film consumption it is impractical to take photographic records of oscilloscope waveforms for long periods of time with strip cameras. Commercially available framing cameras do not attain framing rates great enough for certain sferic observations. Frequently, it is necessary to combine the data with some form of accurate time presentation. For example, (1) sferics observed at widely separated stations can be identified on a world time basis, and (2) for precise measurement of the time interval between sferics.

A device which appears to satisfy these requirements has been developed at the National Bureau of Standards, Boulder Laboratories, Boulder, Colo. Although it was designed and built primarily for sferic studies, the basic concepts and certain features of this instrument may be useful in other research and practical applications (fig. 2).

The timer is composed of conventional decimal-counting units arranged to count from 10 μsec to 31 days with the count controlled by a precision 100 kc standard. Each of the decimal-counting units has a 1–2–2–4 binary output, all of which are read out in parallel by the same pulse used to trigger the camera.

539889—60——6

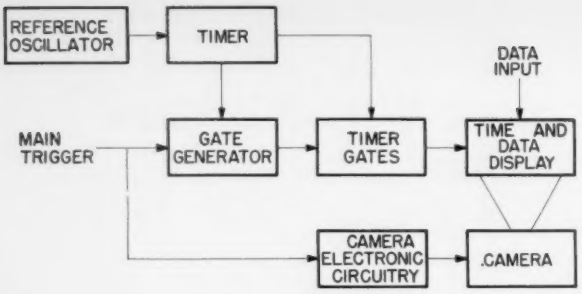

FIGURE 2. *Functional system diagram.*

To prevent any ambiguity in the read-out due to the binary output changing state, the time of the read-out is controlled by the timer. The read-out is made by the first 100-μsec-pulse following the event to be recorded.

Time is displayed for photographic purposes by use of small neon bulbs which are illuminated by a pulse of 100-μsec duration. Since this pulse is 100 μsec long, smaller increments of time must be resolved by another means such as time markers on an oscilloscope trace.

2. Design Approach

It is assumed that an electronic trigger can be derived from the data to be recorded. The time at which the trigger occurs for the purposes of this report is considered to be the time of the event. This trigger and other triggers derived from it in fixed time relationships initiate the oscilloscope sweeps for the data presentation and provide the commands for the time read-out and the mechanical functions of the camera proper.

Sixteen-millimeter film was chosen as a practical compromise between two mutually opposing considerations. Larger film would have been more desirable from the standpoint of picture quality or resolution but would have required greater torque to accelerate both it and the larger transport mechanism.

At the time the design was undertaken a film transport time of about 5 msec was considered adequate for the application at hand. In most cases, oscilloscope sweeps of 500 to 1,000 μsec were used for data presentation. The objective was, therefore, to build a camera that would complete an operational cycle in about 6 msec. It was further required that the camera be able to cycle at this rate for a number of frames.

In this application the average cycling rate was relatively low so there was no unusual requirement for a large driving motor. The essence of the mechanical problem was to supply the high instantaneous torques necessary to accelerate and decelerate the film and especially the film transport mechanism in the short period of time required.

The peak versus average power requirements were met by the simple expedient of an appropriate flywheel mounted directly on the motor shaft. The more difficult part of the problem was to transmit the available high-peak power to the film in a reliable and uniform manner.

The type of mechanism which would be ideal would combine some of the characteristics of both a friction and a positive action clutch. That is, a clutch which would engage and disengage smoothly and quickly with a minimum of external force and at the same time be capable of transmitting a very high torque.

The type of device selected was essentially a cone clutch with the engaging surface operating just outside the critical angle.

The command signal available to actuate the camera (which was supplied by other equipment) was 2 μsec in duration with a nominal amplitude of 100 v. A transducer was required to cause this signal to engage the clutch for the period of time necessary to advance the film one frame. The principle used to accomplish this was to cause a fixed quantity of electricity to flow in a coil similar to the voice coil in a dynamic speaker upon receipt of each command signal. The movement of the voice coil was used directly to engage the clutch.

The use of the usual sprocket wheel to advance the film was not considered because of excessive point pressures exerted on the film by the large accelerating forces. Instead, it was decided to apply the accelerating force across the entire width of the film by means of a precision neoprene-surfaced cylindrical roller.

It was evident from the outset that the inertia of the intermittently moving parts would be of major importance. The design of the driven parts to minimize inertia and yet provide the necessary mechanical strength was rather straightforward. Managing the film supply, however, in such a manner that excessive inertial loads would be prevented was a separate problem of at least equal importance. In the design requirements it was estimated that the camera should be able to take at least 20 frames in rapid succession. It seemed totally impractical to draw film directly from the supply magazine at such high intermittent speeds because of the generally complicated mechanism involved and the possibility of film breakage. Accordingly, it was decided to provide and maintain a free and unsupported loop of film between the drive roller and the supply magazine.

One simplifying aspect of the design requirements was that no shutter was required. In this case, the cathode-ray tubes were simply unblanked and the time was read out when the data occurred.

A crystal-controlled timer which could be synchronized with standard time signals was chosen to maintain a time reference. In order to record the time of an event on the film an instantaneous and unambiguous parallel read-out scheme was devised. For circuit simplicity each increment of time greater than 200 μsec was displayed on the film in a coded binary form. Increments of time smaller than 200 μsec were displayed on the oscilloscope traces.

The relative time accuracy of a crystal-controlled timer is dependent on the stability of the crystal; whereas, the absolute time accuracy or the time comparison between any two geographical points is dependent on the accuracy of the synchronizing signal. WWV (and certain other standard time broadcasts) transmit world time accurately, but due to the propagation path, instantaneous measurements at distant locations can only be resolved to about 1 msec. Through arduous investigation and interpretation of available ionospheric data WWV time can probably be established in retrospect to within two or three tenths of a millisecond.

A low-frequency navigation system known as Loran C transmits signals that may be received in excess of 1,000 miles with a stability of 1 to 2 μsec. If these signals were available at all locations and if they were properly synchronized with each other and with a world time standard, absolute time would be available with an accuracy of 1 to 2 μsec.

The timer described in this report could be synchronized with Loran C signals to provide microsecond absolute timing.

3. System Description

3.1. Camera Mechanics

The camera that was developed, based on the indicated design approach, utilizes methods for film storage and transfer that are rather unique and require detailed explanations. In addition to the film storage and transfer systems, the optical portion of the camera is a Dallmeyer, 15 mm wide-angle f1.5 lens, mounted in a vertical plane for direct exposure.

The main drive unit (fig. 3) consists of a 3,600-rpm induction drive motor, the flywheel, a conical clutch and brake, film drive rollers, and the triggering mechanism. Mounted directly on the motor is a flywheel with a nylon insert used as the driving element in the clutch brake system. The driven element, in normal position, is spring loaded against a stationary, identical nylon insert which acts as the braking element. The mechanical triggering mechanism consists of a large electromagnet and a freely suspended coil. In principle, it is entirely similar to a large electrodynamic speaker. When current is applied to the coil an axial thrust is exerted on the driven element, thus engaging it with the nylon insert (driving element) in the flywheel. The clutch and brake elements are tapered to form sections of a cone and the angle of this taper is close to the critical angle of the cone of friction. In this way, maximum frictional drive and braking are obtained without wedging of the components.

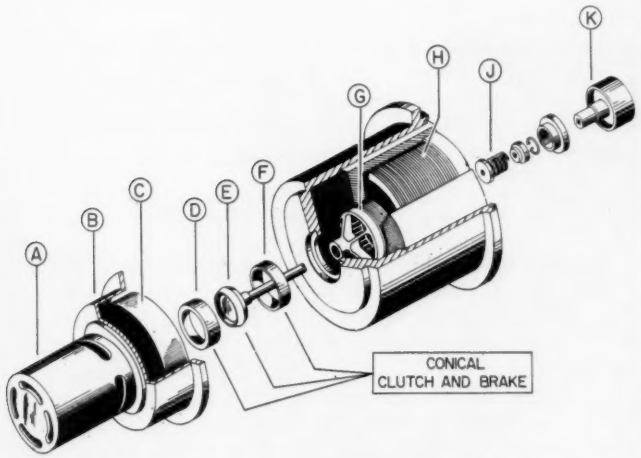

A. DRIVE MOTOR
B. FLYWHEEL HOUSING(cut-away)
C. FLYWHEEL
D. NYLON INSERT (drive element)
E. DRIVING ELEMENT
F. NYLON INSERT (braking element)
G. ACTUATING COIL
H. ELECTROMAGNET
J. TENSION SPRING
K. FILM DRIVING ROLLER

FIGURE 3. *Camera mechanical drive.*

The kinetic energy stored in the flywheel provides the high instantaneous torque necessary to accelerate the transport mechanism when the clutch is engaged. The maximum duty cycle of the film advance is affected by the size of this flywheel since it must store sufficient energy so that the motor speed will not be significantly reduced during the maximum operating rate.

The mechanism for engaging the clutch is a freely suspended coil of insulated copper wire wound on a 3-in. diameter aluminum shell and centered in the air gap of the electromagnet. This coil is connected to the shaft of the driven element of the clutch in such a way that the shaft may rotate inside the coil, but the axial movement of the coil is transmitted to the shaft. The force exerted by this coil is proportional to flux density, wire length, and the current. The time during which the force is applied depends on the length of time the current flows; thus, the film advance is controlled by varying the period of time during which the current flows through the coil.

The film transport mechanism consists of the film drive roller and a tension roller (fig. 4). The film-drive roller is neoprene-coated and has a spline which engages with the shaft of the driven element of the clutch. The shaft is free to move axially but rotational motion is transmitted to the roller. The tension roller is spring loaded against the drive roller with provisions for release to facilitate film loading.

The film storage mechanism contains a 200-ft supply and a 100-ft takeup magazine with a spring loaded light trap that operates when the magazines are removed from the camera. The takeup tension is applied by operating a small, heavy-duty motor (fig. 5) at low voltage in a stalled condition. This motor is located directly behind the takeup magazine and is connected to the film spool inside this magazine. A set of metering rollers (fig. 4) maintain a loop of film to keep the shock of acceleration from tearing the film and to reduce the mass that the main-drive roller must move. These metering rollers are geared together in such a manner that, as film is pulled into the takeup magazine, an equal amount of film is removed from the supply magazine to keep a constant loop of film ahead of the drive roller.

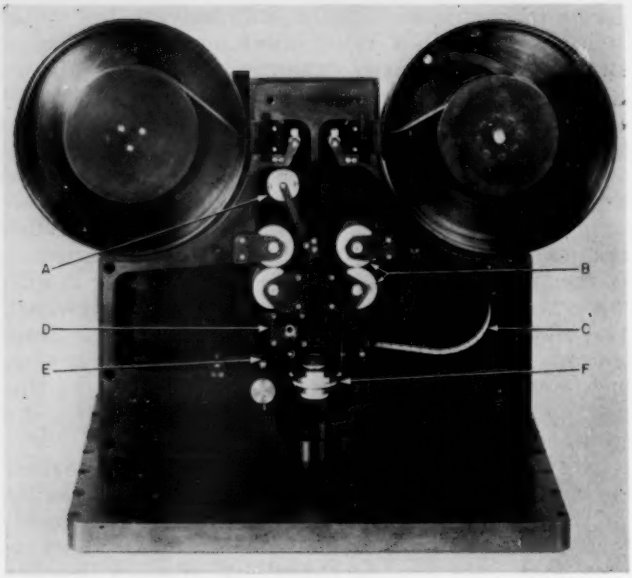

FIGURE 4. *Camera interior detail.*

a. Shock absorber arm, b. metering rollers, c. film loop, d. film drive roller, e. film tension roller, and f. optic system.

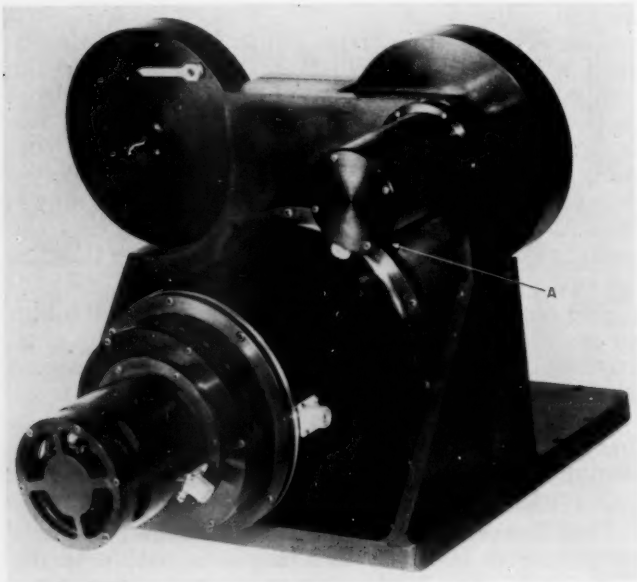

FIGURE 5. *Camera exterior detail.*

a. Takeup motor.

3.2. Camera Electronics

The electronic circuitry for the camera is designed to deliver high current for short durations and at rapid intervals (fig. 6a). A large condenser reservoir supplies this high current intermittently and thus reduces current which must be drawn from a power supply to an average value sufficient to sustain the average pulse rate. The reservoir presently used is a 1,600-μf condenser which will provide approximately ten advances at maximum speed. The power supply is capable of delivering 275 ma which will support an average rate of 60 fps. The average rate could be increased by using a larger power supply, and the number of adjacent advances could be increased by increasing the 1,600-μf reservoir. The camera drive is actuated by discharging an 88-μf condenser with a GL–5544 thyratron through the "voice" coil. The 88-μf condenser is recharged from the large reservoir by use of a second GL–5544.

The basic scheme is as follows: A main trigger pulse is applied to a thyratron trigger circuit. A 40-μsec pulse is generated and fed to the first thryatron through an isolation transformer. The main trigger is also delayed 2 msec and then used in the same way to fire the second thyratron. The second thyratron recharges the 88-μf condenser from the 1,600-μf reservoir (fig. 6b).

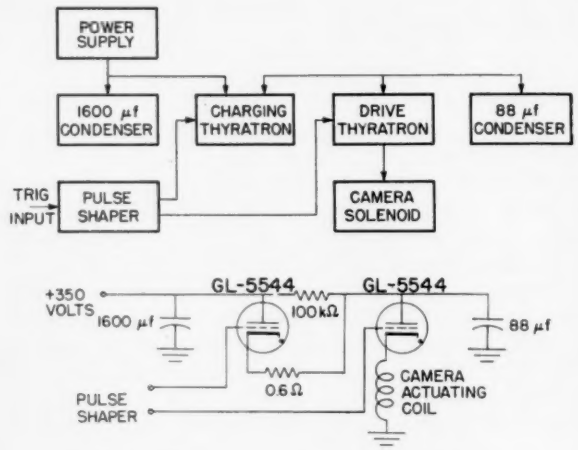

FIGURE 6. *Camera electronic circuitry.*

The complete electronic cycle requires less than 5 msec, and since the film is moving for 5 msec, triggers spaced closer than this would be useless. Therefore, a "killer" circuit was included to eliminate triggers spaced closer than 5 msec.

3.3. Timer Electronics

A reference oscillator operating at 100 kc and with a stability of 1 part in 10^8 is used to control the timer. The 100-kc signal is used to form 10 μsec pulses. These pulses are fed into a series of decimal-counting units so arranged that the count will correspond to time from microseconds to days. The resolution accuracy of this system is 2 or 3 μsec and the time between any 2 sferics can be determined within this accuracy. The timer is adjusted by utilizing the WWV standard time signals. Therefore, the absolute time accuracy to which the timer is calibrated is limited by the propagation variables. This system could be synchronized more accurately if more precise time signals were available.

The timer count from 10 μsec to 10 sec is accomplished by using standard decimal-counting units. Between each unit other stages were added to provide amplification, clipping, differentiation, and to isolate the output of one unit from the input to the next unit. The use of these stages in addition to cathode followers between the units permits longer leads for physical separation of the units. The limiting and isolation provide quite effective protection against spurious signal pickup.

The count of six necessary for the seconds and minutes counters is accomplished by taking advantage of the fact that the output of the third stage of a decimal counter provides a count of six. The hours counter is arranged so that it will reset with an output pulse at 24 (fig. 7). This is accomplished by actuating a relay when the tens-of-hours counter reaches the count of two. When this relay is energized the normal circuit in the units of hours counter is modified in that the output from the second binary digit at count of four is not fed to the third binary digit, therefore, this counter returns to zero rather than counting to five. The output of this second binary digit is applied to the second binary digit in the tens-of-hours counter, thus resetting it to zero and providing an output pulse to the days counters.

3.4. Timer Calibration

Dual inputs to the minutes, hours, and days counters facilitate resetting the counters after nonoperating periods. One-second pulses can be supplied to all of these counters through the other input for setting purposes. A push-button switch on the front of each unit allows the minutes, hours, or days counters to be reset within 60, 24, or 40 sec, respectively. The input to the seconds counter can be interrupted by a switch, holding that counter and hence all subsequent counters. Stopping the seconds counter at 00 and starting it again with the 5-min tone from WWV completes the calibration to within 1 sec.

The procedure necessary to calibrate the timer more precisely is to trigger an oscilloscope with the 1-sec pulses from the timer and to display the WWV signal on this oscilloscope (fig. 8). If the 1-sec pulses are systematically slowed down, the WWV seconds pulses will appear to move from right to left across an oscilloscope with a normal sweep. To slow down the timer, two gate generators are also triggered with the 1-sec pulses, and these gates are used to remove pulses at the input to the 1-msec counter. In the fast position 10 pulses are removed, slowing the timer 10 msec per second; in the slow position 1 pulse is removed, slowing it 1 msec per second. This allows the timer to be set within 1 msec of WWV. If a more accurate setting were desired, the pulses could be removed at the input to the 100-μsec counter, and a third gate with a duration between 100 μsec and 1 msec could be used.

3.5. Timer Read-Out

The decimal-counting units have a modified binary read-out code. This code is the 1-2-2-4 code consistent with the binary states associated with the

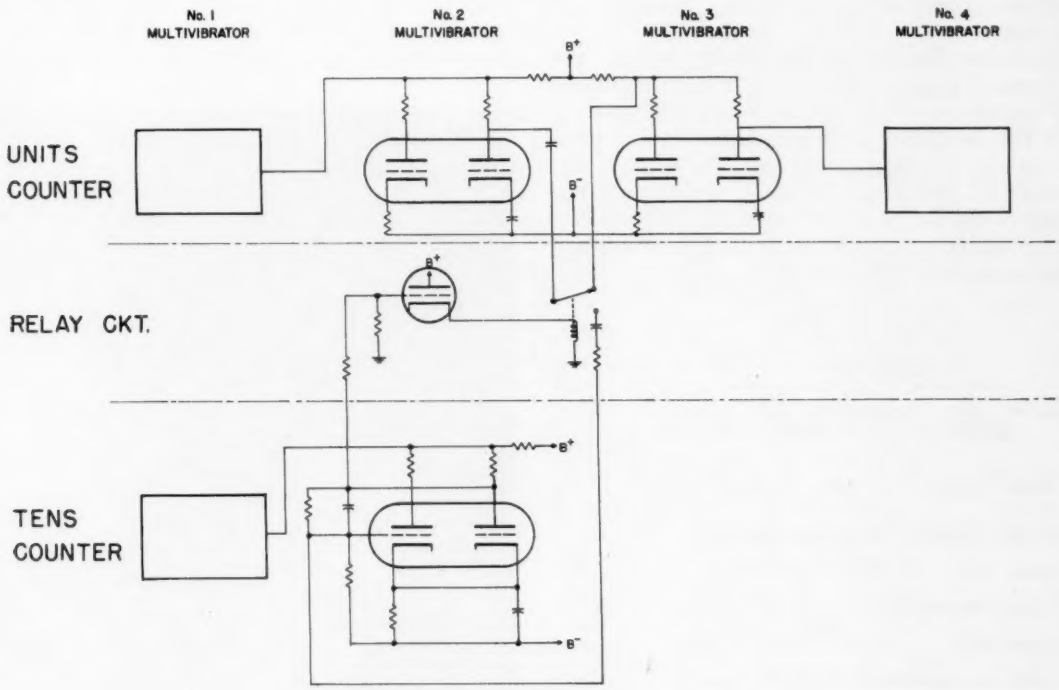

FIGURE 7. *Modification on hours counter.*

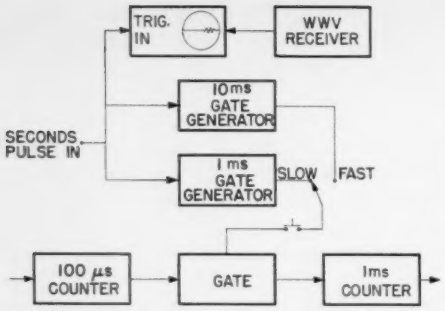

FIGURE 8. *Timer synchronizing circuit.*

feedback loops required to obtain a count of 10 rather than a count of 16.

The output of each binary digit is fed to a logical "and" circuit which operates a neon bulb in the camera field when an additional gate input is applied. This gate input is initiated by the main trigger but controlled by the timer in such a way that all binary digits are read out in a stable state thus precluding ambiguity. Figure 9 shows the block diagram and the waveforms associated with the gate generator used to produce the gate for all of the "and" circuits. The read command (fig. 9a) is applied to a gate generator. The generated gate (fig. 9b) passes the first 200-μsec pulse (fig. 9c). This pulse generates a second gate (fig. 9d) which is stopped simultaneously by the first gate (fig. 9b). Both gates terminate with the next 100-μsec pulse (fig. 9e). The 100-μsec gate (fig. 9d) thus formed is the gate generator output which is one of the inputs to the "and" circuit. This gate occurs only when all of the binary counters above 200-μsec are in a stable state.

The neon bulbs displaying the binary counts are arranged in sets of four for convenience in transposing to decimal numbers. The time below 200-μsec is resolved on the oscilloscope trace, since 10-and 200-μsec markers are superimposed on the traces (fig. 10). If traces of less than 200-μsec duration were desired, time could be read out on neon bulbs down to 10-μsec by utilizing circuitry to hold the binary digits between 10 and 200 μsec.

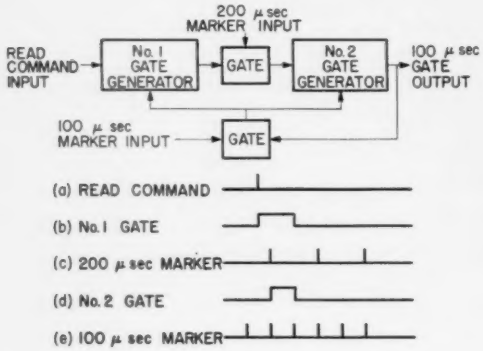

FIGURE 9. *One-hundred microsecond gate generator.*

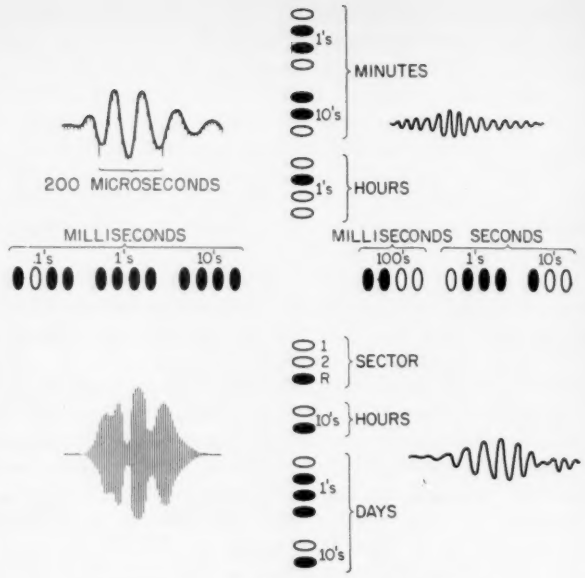

FIGURE 10. *Camera field presentation.*

4. System Performance and Results

Extensive operation of the camera and timer during a 4-month period demonstrated the system's usefulness and also indicated where modifications would be warranted.

The direction that the film moved was parallel to the oscilloscope sweep direction (fig. 11). Sferics which occurred at time intervals less than 5 msec would overlap, and the traces would be lengthened. Rotation of the camera or the scope traces by 90° would resolve this problem. Movement of the film transversely to the direction of the trace should allow sferics separated by only 1 msec to be resolved.

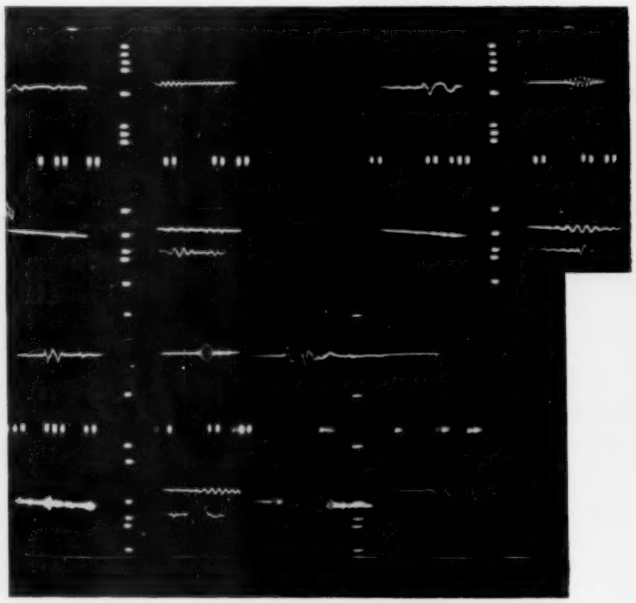

FIGURE 11. *Photographs of adjacent frames.*

The time measured from the main trigger until the camera advance is complete is 7 msec. The film motion is about 24 mm or one and one-half 16 mm frames. The calculated time necessary to move the film 24 mm with the 1-in. drive roller operating at 3,600 rpm is 5.2 msec. The interval measured between the main trigger and the start of the film advance is 1.5 msec, so evidently when the film is moving it is moving at nearly maximum velocity. Figure 11 shows two frames 9 msec apart and 2 others with closer spacing (4.5 msec) where the film was moving when the second sferic occurred. It can be seen that if sferics occur with spacings greater than 7 msec the camera is an intermittent-action frame camera, whereas, if the sferics are more closely spaced the camera becomes a strip camera at a speed of 178 ips for short durations. It is obvious that camera triggers occurring more often than 5 msec would be meaningless, and therefore a 5-msec blocking circuit is operated following each main trigger before the camera is triggered.

Present limitations on the maximum film velocity are the motor speed and the drive-roller diameter. Increasing the motor speed creates bearing problems due to the heavy flywheel and shock loading. On the other hand, increasing the drive-roller diameter from 1 in. to 3 or 4 in. appears entirely feasible. This change would reduce the film transport time from 5.2 msec to 1.7 or 1.3 msec.

Experiments have been conducted using an aluminum disk and a coil wound with strip copper to determine the applicability of the induction disk to engage the clutch. The coil and the disk are coaxial with the film drive. A pulse of current through the coil pushes the disk over by repulsion. Initial results indicate that this method may be faster, thus reducing the 1.5-msec start time, but the disk will not keep the clutch engaged for an extended period of time as can be done with the voice coil. The mechanism associated with the induction disk has fewer moving parts and is inherently simpler. This method should be excellent for higher film transport speeds.

BOULDER, COLO. (Paper 64C2–36)

Publications of the National Bureau of Standards*

Selected Abstracts

A carbon-14 beta-ray standard, benzoic acid-7-C^{14} in toluene, for liquid scintillation counters, W. F. Marlow and R. W. Medlock, *J. Research NBS* **64A,** *No. 2, 143 (1960).*

A carbon-14 beta-ray standard for use in liquid scintillation counting has been prepared and standardized. The sample consists of benzoic acid-7-C^{14} dissolved in toluene. Samples of the solution were oxidized quantitatively in a Paar oxygen bomb, and the radioactivity of the carbon dioxide was compared with the radioactivity of carbon dioxide prepared quantitatively from the Bureau's sodium carbonate-C^{14} standard.

Some effects of aging on the surface area of portland cement paste, C. M. Hunt, L. A. Tomes, and R. L. Blaine, *J. Research NBS* **64A,** *No. 2, 163 (1960).*

A hardened cement paste cured at room temperature, from which part of the evaporable water has been removed by vacuum drying, is shown to decrease in surface area with time. This change is the opposite of that usually observed during hydration and probably represents some colloidal growth phenomenon analogous to aging observed in other colloidal gels. Both water vapor and nitrogen absorption measurements show the effects of aging in cement paste.

Wet or dry paste is shown to undergo less change than paste of intermediate evaporable water content, so that if surface area after storage is plotted as a function of evaporable water content, a curve with a minimum is obtained. With increasing storage temperature there is some indication that this minimum might shift towards lower water content.

Aging is shown to occur during the initial drying of a cement paste, so that even the initial surface area of a cement paste depends upon the manner in which the paste has been dried.

Some solutions for electromagnetic problems involving spheroidal, spherical, and cylindrical bodies, J. R. Wait, *J. Research NBS* **64B,** *No. 1, 15 (1960).*

Solutions are presented for the low-frequency electromagnetic response of an oscillating magnetic dipole by conducting bodies of simple shape. The quasi-stationary approximation is employed throughout which is valid when the relevant dimensions of the problem are all small compared to the free-space wavelength. This amounts to matching solutions of the wave equation within the bodies to solutions of Laplace's equation outside.

Screw-thread standards for federal services 1957. Amends in part H28 (1944) (and in part its 1950 Supplement). *NBS Handb. H28 (1957)—Part II (1959) 75 cents.*

Information is presented on the limits of size, basic dimensions, thread form, and gaging of tapered and straight pipe threads (including Dryseal pipe threads), gas-cylinder-valve outlet and inlet threads, hose coupling threads (including fire-hose coupling threads), and welding and cutting torch hose connections.

Communication theory aspects of television bandwidth conservation, W. C. Coombs, *NBS Tech. Note 25 (PB151384) (1959) 50 cents.*

New concepts of communication bandwidth utilization and conservation are in prospect through difference signal modulation systems in which only relative changes information is transmitted in lieu of absolute amplitudes. By these systems, the changes data function is made one of time as well as of amplitude, so that better advantage can be taken of redundancies in the video signal.

Advantageous conversions of information rate are made feasible by reason of a tremendous disparity existing between the extremely high information capacity of conventional television systems and the relatively very low perception capability of a human observer channel. Information conversions more consistent with perception capabilities of the human channel are achieved in difference signal modulation without usual great expansion of bandwidth that would be required to reproduce every possible absolute amplitude of each datum in the whole video picture mosaic directly.

Conversion to binary digital form accrues the further advantages of binary systems, including greater immunity to noise, greater adaptability to discrete data storage media, greater ease of scrambling for security, and greater amenability of encoding to optimum parametric controls for most advantageous transmission.

Distribution of mail by destination at the San Francisco, Los Angeles, and Baltimore Post Offices, N. C. Severo and A. E. Newman, *NBS Tech. Note 27 (PB151386) (1959) $1.50.*

This report presents the results of the application of the sampling method presented in a paper by Norman C. Severo and Arthur E. Newman entitled "A statistical chain-ratio method for estimating relative volumes of mail to given destinations," to appear in *NBS Journal of Research 64C,* No. 1 (Jan.–Mar. 1960). These studies were made at the San Francisco, Los Angeles, and Baltimore Post Offices.

Photographic dosimetry at total exposure levels below 20 mr, M. Ehrlich and W. L. McLaughlin, *NBS Tech. Note 29 (PB151388) (1959) 50 cents.*

Photographic dosimetry at exposure levels below 20 mr is difficult because of insufficient sensitivity of commercial photographic emulsions, instabilities in the latent photographic image, and inaccuracies in sensitometric procedure. Some of the endeavors to cover the range below 20 mr more adequately, both with film-scintillator combinations and with conventional photographic dosimeters, will be briefly discussed.

Resistance diode bridge circuit for temperature control, L. H. Bennett and V. M. Johnson, *NBS Tech. Note 34 (PB151393) (1959) 50 cents.*

The conventional a-c bridge gives irregular performance including loss of temperature control when the temperature error exceeds a certain critical value. The present note describes a simple method of achieving stable temperature control over a large range of temperatures.

Service area of an airborne television station, M. T. Decker, *NBS Tech. Note 35 (PB151394) 75 cents.*

As a step in the evaluation of a proposed airborne television network, the service to be expected from an airborne station has been calculated for a wide variety of operating conditions. The use of basic transmission loss to describe the radio propagation effects enables the results to be used when equipment parameters are changed as system requirements and economic considerations dictate.

Strain gauge calibration device for extreme temperatures, R. M. McClintock, *Rev. Sci. Instr.* **30,** *No. 8, 715 (1959).*

A device is described for applying known static strains to strain gages under extreme temperature environments. The essential part is a constant strength cantilever beam used in

such a way that the mechanical properties of the component parts need not be accurately known. The location of the strain gages on the beam is not critical since strain is constant along its length. Conditions are given for which errors caused by thermal expansion can be eliminated. Measurements of the strain sensitivity of constantan wire gages are given at temperatures between 4° and 300° Kelvin.

Rapid insertion device for coaxial attenuators, A. Y. Rumfelt and R. J. Como, *Rev. Sci. Instr.* **30,** *No. 8, 687 (1959).*

A rapid insertion device for coaxial attenuators is described. This device is used as an alignment aid when making insertion loss measurements of fixed coaxial attenuators at frequencies up to 6 kMc. It provides a quick connect and disconnect feature, maintains axial alignment of the connectors during joining and separation, and reduces cable flexure. The improved repeatability and accuracy of insertion loss measurements is shown by comparative data with different alignment techniques.

PILOT, the NBS multicomputer system, A. L, Leiner, W. A. Notz, J. L. Smith, and A. Weinberger. *Proc. Eastern Joint Computer Conf. (Philadelphia, Pa.), p. 164 (1958).*

At NBS a new large-scale digital system has been designed for use on a wide variety of experimental applications ranging from automatic search and interpretation of Patent Office records to real-time control of commercial aircraft traffic. Because of this wide range of intended use, the system had to combine in a single installation a variety of characteristics not ordinarily associated with one facility, namely (1) a high computation rate, (2) highly flexible control capabilities for communicating with the outside world, and (3) a wide repertoire of internal processing formats. The over-all system is organized around three independently programmed computers which intercommunicate in such a way as to permit all three to work together concurrently on a common problem, each computer working on the piece of the problem for which it is individually best suited. The over-all system thus provides a working model of an integrated multi-computer network.

Investigation of creep behavior of structural joints under cyclic loads and temperatures, L. Mordfin, N. Halsey, and G. E. Greene, *NASA Tech. Note D–181, p. 37 (1959).*

Eighty-two structural joint specimens were tested to evaluate the effects of cyclic loads and cyclic temperatures on creep and rupture. The specimens included riveted joints of 2024–T3 clad aluminum alloy, and riveted and spot-welded joints of 17–7 PH (TH 1050) stainless steel. The results of these tests show a wide variance but indicate certain trends which permit the estimation of the cyclic creep behavior of joints.
An analysis of the effects of stress concentration on the tensile rupture strength of riveted joints is presented in appendix A. This, together with data from several other laboratories, shows that the effects are small for joints fabricated from notch ductile materials and conventional rivets.

Microwave reflectometer techniques, G. F. Engen and R. W. Beatty, *IRE Trans. on Microw. Theory and Tech.,* **MTT–7,** *No. 3, 346 (1959).*

A rigorous analysis of the microwave reflectometer is presented for what is believed to be the first time. By means of this analysis, the correct adjustment of auxiliary tuners is described and the errors resulting from incorrect adjustments are treated in a quantitative manner.
It is shown how the reflectometer technique may be further simplified while preserving the accuracy of measurement. A convenient method of adjusting the auxiliary tuners is described, sources of error are discussed, and an example is given of the calculation of error limits.

Cryogenic engineering of hydrogen bubble chambers, B. W. Birmingham, D. B. Chelton, D. B. Mann, and H. P. Hernandez, *ASTM Bull. No. 240, 34 (TP164) (1959).*

Low-temperature material problems encountered during the development of a liquid-hydrogen bubble chamber are discussed. Properties affecting the selection of the bubble chamber material, the glass window, and the thermal radiation shield are examined. Methods of sealing the glass window to the chamber with various gaskets suitable for use at liquid hydrogen temperature (−423 F) are presented. In addition, a method of continuously maintaining the bubble chamber and contents at liquid hydrogen temperature by means of an external refrigerator is described.

On prediction of system behavior, J. R. Rosenblatt, *Proc. of the New Yrok Univ.-Ind. Conf. on Reliability Theory (New York, N.Y.), p. 39 (1958).*

It is customary in theoretical discussions of prediction of system performance to assume that the relation between variables by which performance is assessed and variables describing the parts of the system can be specified by a function. The purpose of this paper is to consider some of the problems which arise in choosing the form of such a function and in specifying the relevant variables and the nature of appropriate experiments, measurements, and data.
In the context of each of a number of familiar types of mathematical model, the possible consequences of alternative choices of time units, subsystem definitions, and independence assumptions are discussed.

Ceramic wafer tubes for modular units, C. P. Marsden, *sec. on Components and Materials, Electronics* **32,** *No. 39, 94 (1959).*

Mechanized assembly and processing means have been designed and constructed to show that ceramic wafer tubes can be produced with a yield of better than 75 percent and with a high degree of reliability and ruggedness in military environments. This article discloses the design, methods of fabrication and the processing of these tubes.

Magnified and squared VSWR responses for microwave reflection coefficient measurements, R. W. Beatty, *IRE Trans. on Microw. Theory and Tech.* **MTT–7,** *No. 3, 346 (1959).*

In conventional microwave impedance measuring instruments, the measured ratio of maximum to minimum detector signal level is ideally equal to the voltage standing-wave ratio (VSWR) of the termination. In this paper, it is shown how radically different types of response are obtainable in which the observed ratio may approximately equal the square of the VSWR or may be magnified any desired amount. Theory is given enabling accurate measurements by interesting techniques. Accuracies of 0.1 percent in VSWR to 2.0 have been achieved using magnified response techniques.

Method of cooling head-on photomultipliers, G. C. Harman, *Rev. Sci. Instr.* **30,** *No. 8, 742 (1959).*

A simple method of cooling the photoemissive surface of head-on photomultipliers is described. It consists of a small, specially constructed Dewar with a window in its top. The Dewar is charged with dry ice powder and slipped over the head of the multiplier so that it cools only the sensitive surface. The rest of the tube remains at room temperature. The dark current is reduced by a factor of at least 500.

Optical measurements on thin films of condensed gases at low temperatures, J. Kruger and W. J. Ambs, *J. Opt. Soc. Am.* **44,** *1195 (1959).*

A determination of the refractive indices of thin films of oxygen, nitrogen, carbon dioxide, water, argon, neon, and krypton condensed at 4.2° K was made. These were ob-

tained for the 5461 A line of Hg with an ellipsometer. Similar measurements were also made on films of these gases condensed after passage through a microwave discharge. With the exception of N_2, and Kr measurable differences in refractive indices were observed between films condensed from discharged and undischarged gases.

Wavelength definition of the meter, I. C. Gardner, *Systems of Units, Natl. and Intern. Aspects, Publ. Am. Assoc. Advance. Sci., No. 57, p. 53 (1959).*

The different applications of the national prototype meter to the calibration of line standards, of end standards, and of wavelengths are presented. The advantages of a wavelength standard are considered and the progress of international conferences for redefining the meter in terms of a wavelength standard is set forth. One may expect final and conclusive action at the Conference (General) of Weights and Measures in 1960. The advantages to be anticipated from the development of an atomic beam source are discussed.

Digital recording of electrocardiographic data for analysis by a digital computer, L. Taback, E. Marden, H. L. Mason, and H. V. Pipberger, *IRE Trans. Med. Electronics* **ME–6,** *167 (1959).*

A corrected orthogonal 3-lead system has been used to record electrocardiograms directly from patients at Veterans Hospitals, using three FM channels of magnetic tape. A pilot facility has been designed and assembled by NBS to permit a medical technician to inspect these on an oscilloscope and select a significant cardiac cycle. This is automatically sampled at millisecond intervals and the numerical values are stored in digital form on magnetic tape acceptable to an electronic computer. Upon writing various programs for the digital computer, the cardiac researcher will have a flexible tool for objective analysis of large quantities of biological data by a variety of possible criteria.

Young's modulus of various refractory materials as a function of temperature, J. B. Wachtman, Jr., and D. G. Lam, Jr., *J. Am. Ceram. Soc.* **42,** *No. 5, 254 (1959).*

Young's modulus as a function of temperature was determined by a dynamic method for single-crystal sapphire and ruby and for polycrystalline aluminum oxide, magnesium oxide, thorium oxide, mullite, spinel, stabilized zirconium oxide, silicon carbide, and nickel-bonded titanium carbide. For the single crystals, Young's modulus was found to decrease linearly with increasing temperature from 100° C to the highest temperature of measurement. For all the polycrystalline materials, except silicon carbide, stabilized zirconium oxide, and spinel, Young's modulus was found to decrease approximately linearly with increasing temperature until some temperature range characteristic of the material was reached in which Young's modulus decreased very rapidly and in a nonlinear manner with increasing temperature. This rapid decrease at high temperature is attributed to grain-boundary slip. Stabilized zirconium oxide and spinel were found to have the same rapid decrease in Young's modulus at high temperature, but they also had a decidely nonlinear temperature dependence at low temperature.

Thermodynamic properties of helium at low temperatures and high pressures, D. B. Mann and R. B. Stewart, *J. Heat Transfer* **81,** *323 (1959).*

The thermodynamic properties of helium have been compiled and correlated for a temperature range from 3.0 to 20° K for pressures to 100 atmospheres and for specific volumes from 5 to 800 liters per kilogram. The properties are presented on both the Temperature-Entropy and the Enthalpy-Entropy coordinate systems and include pressure, temperature, volume, entropy and enthalpy.

Fire research at the National Bureau of Standards, A. F. Robertson, *Fire Research Abstr. and Rev.* **I,** *No. 4, 159 (1959).*

A review is presented of work performed at the National Bureau of Standards and primarily directed towards the unwanted or accidental fire problem. It is emphasized that the general field of fire research is so broad that many other research activities at the NBS may be considered as pertinent to this subject. Some few of these studies are mentioned; however, emphasis is placed on problems relating to ignition, growth, confinement, and extinguishment of fires. Pertinent references to NBS work are included.

Preliminary assessment of the IGY, A. H. Shapley, *Proc. Natl. Electron. Conf., p. 1 (1958).*

The activities of the International Geophysical Year are reviewed, with particular emphasis on studies of the ionosphere.

Factorial experiments in life testing, M. Zelen, *Technometrics* **1,** *No. 3, 269 (1959).*

This paper discusses procedures for analyzing factorial experiments, where the experiment deals with the life testing of components or equipment. These procedures assume an underlying general distribution of "times-to-failure," of which the exponential, Weibull, and extreme value distributions are special cases. Statistical tests and confidence procedures are outlined, and an example illustrating the procedure for life-test results of glass capacitors is included. Small sample approximations, which are adequate for practical applications, are given for the proposed procedures. This is shown empirically by generating thousands of life-test experiments on an electronic computer. An empirical sampling investigation is given of the robustness of the proposed procedures. From the sampling results, it is concluded that these techniques are sensitive (non-robust) to departures from the original assumptions on the probability distribution of failure-times. An investigation is also given of a transformation which appears to give robust results. These same techniques carry over exactly to the situation where one is analyzing an array of variance estimates from an underlying normal population.

Other NBS Publications

Journal of Research, Section A. Physics and Chemistry, Volume 64A, No. 2, March–April 1960. 70 cents.

A carbon-14 beta-ray standard, benzoic acid-7-C^{14} in toluene, for liquid scintillation counters. W. F. Marlow and R. W. Medlock. (See above abstracts.)

A comparison of experimental and theoretical relations between Young's modulus and the flexural and longitudinal resonance frequencies of uniform bars. S. Spinner, T. W. Reichard, and W. E. Tefft.

Determination of copolymer composition by combustion analysis for carbon and hydrogen. Lawrence A. Wood, Irving Madorsky, and Rolf A. Paulson.

Some effects of aging on the surface area of Portland cement paste. C. M. Hunt, L. A. Tomes, and R. L. Blaine. (See above abstracts.)

Conformations of the pyranoid sugars. I. Classification of conformers. H. S. Isbell and R. S. Tipson.

Tritium-labeled compounds III. Aldoses-*1-t*. H. S. Isbell, H. L. Frush, N. B. Holt, and J. D. Moyer.

Determination of aluminum in precipitation hardening stainless steel and high temperature alloys. Lawrence A. Machlan, John L. Hague, and Edward J. Meros.

Journal of Research, Section B. Mathematics and Mathematical Physics, Vol. 64B, No. 1, January–March 1960. 75 cents.

Theory of diffraction in microwave interferometry. D. M. Kerns and E. S. Dayhoff.
Some solutions for electromagnetic problems involving spheroidal, spherical, and cylindrical bodies. James R. Wait. (See above abstracts.)
Kantorovich's inequality. Morris Newman.
A symmetric continuous poker model. A. J. Goldman and J. J. Stone.
Moebius function on the lattice of dense subgraphs. R. E. Nettleton and M. S. Green.
The minimum of a certain linear form. Karl Goldberg.
Space of k-commutative matrices. Marvin Marcus and N. A. Khan.
Selected bibliography of statistical literature, 1930 to 1957: I. Correlation and regression theory. Lola S. Deming.
Selected bibliography of statistical literature, 1930 to 1957: II. Time series. Lola S. Deming.

Journal of Research, Section D. Radio Propagation, Volume 64D, No. 3, May–June 1960. 70 cents.

A theory of radar scattering by the moon. T. B. A. Senior and K. M. Siegel.
A theory of wavelength dependence in ultrahigh frequency transhorizon propagation based on meteorological considerations. Ralph Bolgiano, Jr.
A preliminary study of radiometeorological effects on beyond-horizon propagation. F. Ikegami.
Trade-wind inversion as a transoceanic duct. M. Katzin, H. Pezzner, B. Y.-C. Koo, J. V. Larson, and J. C. Katzin.
An analysis of propagation measurements made at 418 megacycles per second well beyond the radio horizon (a digest). H. B. Janes, J. C. Stroud, and M. T. Decker.
On the calculation of the departures of radio wave bending from normal. B. R. Bean and E. J. Dutton.
On the mode theory of very-low-frequency propagation in the presence of a transverse magnetic field. D. D. Crombie.
On the theory of reflection of low- and very-low-radiofrequency waves from the ionosphere. J. Ralph Johler and Lillie C. Walters.
Focusing, defocusing, and refraction in a circularly stratified atmosphere. K. Toman.
Response of a loaded electric dipole in an imperfectly conducting cylinder of finite length. Charles W. Harrison, Jr., and Ronold W. P. King.
Impedance characteristics of a uniform current loop having a spherical core. Saburo Adachi.

Hydraulic Research in the United States—1959, H. K. Middleton, Misc. Pub. 227 (1959) $1.25.
Frequency dependence of VHF ionospheric scattering, J. C. Blair, NBS Tech. Note 9 (PB151368) (1959) 75 cents.
Some applications of statistical sampling methods to outgoing letter mail characteristics, N. C. Severo, A. E. Newman, S. M. Young, and M. Zelen, NBS Tech. Note 16 (PB151375) (1959) $2.75.
Radio noise data for the International Geophysical Year July 1, 1957—December 31, 1958, W. Q. Crichlow, C. A. Samson, R. T. Disney, and M. A. Jenkins, NBS Tech. Note 18 (PB151377) (1959) $2.50.
Variations of gamma cassiopeiae, S. R. Pottasch, NBS Tech. Note 21 (PB151380) (1959) 75 cents.
A history of vertical-incidence ionosphere sounding at the National Bureau of Standards, S. C. Gladdern, NBS Tech. Note 28 (PB151387) (1959) $2.00.
Aerodynamic phenomena in stellar atmospheres—A bibliography, NBS Tech. Note 30 (PB151389) (1959) $1.25.

The following papers appear in Treatise on Anal. Chem., pt. 1. Theory and practice, vol. 1 (The Interscience Encyclopedia, Inc., New York, N.Y., 1959):
Accuracy and precision: Evaluation and interpretation of analytical data, W. J. Youden, ch. 3. Sec. A. Analytical chemistry: its objectives, functions and limitations, p. 47.
Principles and methods of sampling, W. W. Walton and J. I. Hoffman, ch. 4. Sec. A. Analytical chemistry: its objectives, functions and limitations, p. 67.
Atomic weights, E. Wichers, ch. 6. Sec. B. Application of chemical principles, p. 161.
Concept and determination of pH, R. G. Bates, ch. 10. Sec. B. Application of chemical principles, p. 361.
Electrode potentials, R. G. Bates, ch. 9. Sec. B. Application of chemical principles, p. 319.

System loss in radio-wave propagation, K. A. Norton, Letter to Editor, Proc. IRE **47,** No. 9, 1661 (1959).
The oxide films formed on copper single crystal surfaces in pure water. 1. Nature of the films formed at room temperature, J. Kruger, J. Electrochem. Soc. **106,** No. 10, 847 (1959).
Variation of the thermodynamic ideal temperature in the polystyrene-cyclohexane system, D. McIntyre, J. H. O'Mara, and B. C. Konouck, J. Am. Chem. Soc. **81,** 3498 (1959).
Energy dissipation in standing waves in rectangular basins, G. H. Keulegan, J. Fluid Mech. **6,** Pt. 1, 35 (1959).
Trapped energetic radicals, J. L. Franklin and H. P. Broida, Ann. Rev. Phys. Chem. **10,** 145 (1959).
Total photoelectric cross sections of copper, molybdenum, silver, tantalum, and gold at 662 kev, W. F. Titus, Phys. Rev. **115,** No. 2, 351 (1959).
Diode in feedback loop makes stable transistor bias circuit, G. F. Montgomery, Electronic Design **7,** 54 (1959).
Strength of synthetic single crystal sapphire and ruby as a function of temperature and orientation, J. B. Wachtman and L. H. Maxwell, J. Am. Ceram. Soc. **42,** No. 9, 432 (1959).
Dimensional stability of impregnated sole leather, B. H. Fouquet, J. Am. Leather Chemists' Assoc. **LIV,** No. 10, 544 (1959).
Theoretical problems of reliability measurement and prediction, J. R. Rosenblatt, Proc. of the Third Exploratory Conf. on Missile Model Design for Reliability Prediction at White Sands Missile Range (New Mexico) p. 29 (1959).
Dimensional changes in systems of fibrous macromolecules: polyethylene, L. Mandelkern, D. E. Roberts, A. F. Diorio, and A. S. Posner, J. Am. Chem. Soc. **81,** 4148 (1959).
Attenuation of scattered cesium-137 gamma rays, F. S. Frantz, Jr., and H. O. Wyckoff, Radiology **73,** No. 2, 263 (1959).
Observations of the ionosphere over the south geographic pole, R. W. Knecht, J. Geophys. Research **64,** No. 9, 1243 (1959).
Dependence of mechanical strength of brittle polycrystalline specimens on porosity and grain size, F. P. Knudsen, J. Am. Ceram. Soc. **42,** No. 8, 376 (1959).
Theory of dielectric relaxation in molecular crystals, J. D. Hoffman, Arch. sci. (Geneva), Soc. Phys. et Hist. Nat. Geneve **12,** 36 (1959).
Denture reliners—direct, hard, self-curing resin, G. M. Brauer, E. E. White, Jr., C. L. Burns, and J. B. Woelfel, J. Am. Dental Assoc. **59,** 270 (1959).
Photoproton cross sections of carbon, S. Penner and J. E. Leiss, Phys. Rev. **114,** No. 4, 1101 (1959).
A porcelain reference electrode conductive to sodium ions for use in molten salt systems, R. J. Labrie and V. A. Lamb, J. Electrochem. Soc. **106,** No. 10, 895 (1959).
Memorandum on a procedure for obtaining spectral radiant intensities of tungsten-filament lamps, 400–700 mμ, L. E. Barbrow, Letter to Editor, J. Opt. Soc. Am. **49,** No. 11, 1122 (1959).
Paramagnetic resonance spectra of active species. Blue material from hydrazoic acid, W. B. Gager and F. O. Rice, J. Chem. Phys. **31,** No. 2, 564 (1959).
Argon deposition on a 4.2° K surface, S. N. Foner, F. A. Mauer, and L. H. Bolz, J. Chem. Phys. **31,** No. 2, 546 (1959).

Low-temperature tensile properties of copper and four bronzes, R. M. McClintock, D. A. Van Gundy, and R. H. Kropschot, ASTM Bull. No. 240, 34 (TP177) (1959).

Kinetic equation for a plasma with unsteady correlations, C. M. Tchen, Phys. Rev. **114,** 394 (1959).

A nomenclature for conformations of pyranoid sugars and derivatives, H. S. Isbell and R. S. Tipson, Science **130,** No. 3378, 793 (1959).

On the convergence of the Rayleigh quotient iteration for the computation of the characteristic roots and vectors. III (General Rayleigh quotient and characteristic roots with linear elementary divisors) A. M. Ostrowski, Arch. Rat. Mech, Anal. **3,** 325 (1959).

On the convergence of the Rayleigh quotient iteration for the computation of the charactristic roots and vectors. IV (Generalized Rayleigh quotient for nonlinear elementary divisors), A. M. Ostrowski, Arch. Rat. Mech. Anal. **3,** 341 (1959).

Spectral study of a visible, short-duration afterglow in nitrogen, B. E. Beale, Jr., and H. P. Broida, J. Chem. Phys. **31,** No. 4, 1030 (1959).

Atomic electron affinities, F. Rohrlich, Nature **183,** 244 (1959).

Cavity resonators for dielectric spectroscopy of compressed gases, H. E. Bussey and G. Birnbaum, Rev. Sci. Instr. **30,** 800 (1959).

A discussion of federal specifications GS–X–620 and L–F–310 for dental X-ray apparatus and dental X-ray film, G. C. Paffenbarger, A. F. Forziati, and M. P. Kumpula, J. Am. Dental Assoc. **59,** 472 (1959).

Dynamic stability of frozen radicals. II. The formal theory of the model, J. L. Jackson, J. Chem. Phys. **31,** No. 3. 722 (1959).

An additional lunar influence on equatorial *Es* at Huancayo, R. W. Knecht, Research Note J. Atmospheric and Terrest. Phys. **14,** 348 (1959).

On artificial geomagnetic and ionospheric storms associated with high-altitude explosions, S. Matsusbita, J. Geophys. Research **6,** 1149 (1959).

An intermittent-action camera with absolute time calibration, R. G. Hefley, R. H. Doherty, and E. L. Berger, IRE Wescon Conv. Record **3,** Pt. 6, 129 (1959).

Nonresonant microwave absorption and electric dipole moment of NO in the gaseous state, A. A. Maryott and S. J. Kryder, J. Chem. Phys. **31,** No. 3, 617 (1959).

The earth and its environment, S. Chapman, Proc. IRE **47,** No. 2, 137 (1959).

Bremsstrahlung cross-section formulas and related data, H. W. Koch and J. W. Motz, Rev. Modern Phys. **31,** No. 4, 920 (1959).

Note on quiet-day vertical cross sections of the ionosphere along 75° W geographic meridian, J. W. Wright, Letter J. Geophys. Research **64,** 1631 (1959).

Effect of atomic tests on radio noise, C. A. Samson, Letter Nature **184,** 538 (1959).

Short-time stability of a quartz-crystal oscillator as measured with an ammonia maser, A. H. Morgan and J. A. Barnes, Letter Proc. IRE **47,** 1782 (1959).

Electromagnetic radiation from cylindrical structures, J. R. Wait (Pergamon Press, New York, N.Y., 1959).

Interplanetary gas. I: Hydrogen radiation in the night sky, J. C. Brandt and J. W. Chamberlain, Astrophys. J. **130,** 670 (1959).

The nova outburst. III. The ionization of hydrogen gas by an exciting star, J. Jefferies and S. Pottasch, Ann. Astrophys. J. **22,** 318 (1959).

Exploratory study, by low temperature X-ray diffraction techniques, of diborane and the products of a microwave discharge in diborane, L. H. Bolz, F. A. Mauer, and H. S. Peiser, J. Chem. Phys. **31,** No. 4, 1005 (1959).

Some clinical applications of research findings in dental materials, G. C. Paffenbarger, Ohio Dental J. **33,** No. 3, 218 (1959).

Liquid helium cryostat with an integral super-conducting resonator, E. Maxwell and F. A. Schmidt, Suppl. Bull. Inst. Intern. du Froid, Comm. **1,** Delft, Holland, Annexe 1958–1, p. 95 (1958).

Sporadic *E* observed on VHF oblique incidence circuits, E. K. Smith, In North Atlantic Treaty Organization. Sporadic *E* ionization; Ionospheric Research Meeting, AGARD Avionics Panel, Cambridge, England, Sept. 1958 AGARDograph 34), p. 129 (1958).

Low-temperature transport properties of copper and its dilute alloys: Pure copper, annealed and cold-drawn, R. L. Powell, H. M. Roder, and W. J. Hall, Phys. Rev. **115,** 314 (1959).

The double bond isomerization of olefins by hydrogen atoms at −195°, M. D. Scheer and R. Klein, J. Phys. Chem. **63,** 1517 (1959).

Paramagnetic resonance in the free hydroxyl radical, H. E. Radford, Nuovo Cimento, Serie X **14,** 245 (1959).

Relaxation processes in multistate systems, K. E. Shuler, Phys. of Fluids **2,** No. 4, 442 (1959).

The following appear in Proc. Intern. Rubber Conf., Nov. 8 to 13, 1959 (Washington, D.C.):

Power loss and operating temperature of tires, R. D. Stiehler, M. N. Steel, G. G. Richey, J. Mandel, and R. H. Hobbs, p. 73.

An indoor tester for measuring tire tread wear, G. G. Richey, J. Mandel, and R. D. Stiehler, p. 104.

Measurement of the aging of rubber vulcanizates, J. Mandel, F. L. Roth, M. N. Steel, and R. D. Stiehler, p. 221.

Standard materials for rubber compounding, F. L. Roth and R. D. Stiehler, Proc. p. 232.

Invariant and complete stress functions for general continua, C. Truesdell, Arch. for Rational Mech. and Anal. **1,** No. 4, 1 (1959).

On the convergence of Gauss' alternating procedure in the method of least squares, A. M. Ostrowski, Ann. Mat. Pura Appl. (Bologna, Italy) (IV), **48,** 229 (1959).

Ethane carbon-carbon distance obtained from infrared spectra, H. C. Allen and E. K. Plyler, J. Chem. Phys. **31,** No. 4, 1062 (1959).

The anomalous inversion in cristobalite, R. F. Walker, The kinetics of high temperature processes, 228 pages (J. Wiley & Sons, New York, N.Y., 1959).

Determination of starch in paper. A comparison of the TAPPI, enzymatic, and spectrophotometric methods, J. L. Harvey, B. W. Forshee, and D. G. Fletcher, Tappi **42,** No. 11, 878 (1959).

Branched-chain higher sugars. III. A 4-*C*-(hydroxymethyl)-pentose, R. Schaffer, J. Am. Chem. Soc. **81,** 5452 (1959).

Vibrational spectrum of cyanate ion in various alkali halide lattices, A. Maki and J. C. Decius, J. Chem. Phys. **31,** No. 3, 772 (1959).

Glass research at the National Bureau of Standards, C. H. Hahner, The Glass Industry, p. 588 (1959).

Applications of the molecular refractivity in radio metrology, B. R. Bean and R. M. Gallet, J. Geophys. Research **64,** No. 10, 1439 (1959).

Use of crystal to display high energy X-ray images, J. S. Pruitt, Non-Destructive Testing **XVII**, No. 6, 359 (1959).

The measuring process, J. Mandel, Technometrics **1,** No. 3, 251 (1959).

Refractive indices and transmittances of several optical glasses in the infrared, G. W. Cleek, J. J. Villa, and C. H. Hahner, J. Opt. Soc. Am. **49,** No. 11, 1090 (1959).

Absolute photometry of the aurora—II. Molecular nitrogen emission in the sunlit atmosphere, M. H. Rees, J. Atmospheric and Terrest. Phys. **14,** 338 (1959).

Absolute photometry of the aurora—I. The ionized molecular nitrogen emission and the oxygen green line in the dark atmosphere, M. H. Rees, J. Atmospheric and Terrest. Phys. **14,** 325 (1959).

**Publications for which a price is indicated (except for NBS Technical Notes) are avaliable only from the Superintendent of Documents, U.S. Government Printing Office, Washington 25, D.C. (foreign postage, one-fourth additional). Technical Notes are available only from the Office of Technical Services, U.S. Department of Commerce, Washington 25, D.C. (Order by PB number.) Reprints from outside journals and the NBS Journal of Research may often be obtained directly from the author.*

UNITED STATES
GOVERNMENT PRINTING OFFICE
DIVISION OF PUBLIC DOCUMENTS
WASHINGTON 25, D.C.

OFFICIAL BUSINESS

PENALTY FOR PRIVATE USE TO AVOID
PAYMENT OF POSTAGE, $300
(GPO)

JOURNAL OF RESEARCH of the National Bureau of Standards Vol. 64C, No. 2 April–June 1960
C. Engineering and Instrumentation

Contents

Page

Measurement of cobalt-60 and cesium-137 gamma rays with a free-air chamber. H. O. Wyckoff. 87

Apparatus for the measurement of the normal spectral emissivity in the infrared. Arthur G. Maki, Ralph Stair, and Russell G. Johnston. 99

Electrostatic deflection plates for cathode-ray tubes. I. Design of single-bend deflection plates with parallel entrance sections. II. Deflection defocusing distortion of single-bend deflection plates with parallel entrance sections. Lothar Frenkel. 103

The functional synthesis of linear plots. J. P. Vinti and R. F. Dressler. 115

Radiation field from a rectangular source. J. H. Hubbell, R. L. Bach, and J. C. Lamkin. 121

Microwave attenuation measurements with accuracies from 0.0001 to 0.06 decibel over a range of 0.01 to 50 decibels. G. F. Engen and R. W. Beatty. 139

Effect of oleophobic films on metal fatigue. H. E. Frankel, J. A. Bennett, and W. L. Holshouser. 147

Ratio-recording spectroradiometer. Harry K. Hammond III, Warren L. Holford, and Milton L. Kuder. 151

An intermittent-action camera with absolute time calibration. G. Hefley, R. H. Doherty, and E. L. Berger. 159

Publications of the National Bureau of Standards. 167

For sale by the Superintendent of Documents, U.S. Government Printing Office, Washington 25, D.C. Price 75 cents (single copy)
Subscription price: $2.25 a year; 50 cents additional for foreign mailing.

UNITED STATES GOVERNMENT PRINTING OFFICE, WASHINGTON : 1960